UNIVERSITY of CALIFORNIA
Santa Barbara

Modeling Variability in Black Hole Images

A dissertation submitted in partial satisfaction of the
requirements for the degree of

Doctor of Philosophy

in

Physics

by

Lia Medeiros

Committee in charge:

Professor Omer Blaes, Chair

Professor Feryal Özel

Professor Joe Hennawi

Professor Peng Oh

March 2019

The dissertation of Lia Medeiros is approved:

Professor Feryal Özel

Professor Joe Hennawi

Professor Peng Oh

Professor Omer Blaes, Chair

March 2019

This dissertation is dedicated to my loving and patient companion for the past 16 years. You were with me through every late night, every moment of doubt and triumph, and every move that led to this dissertation, I just wish you could have been here to see it finished.

Acknowledgements

First and foremost I must acknowledge the critical role of my advisors, Professors Feryal Özel and Dimitrios Psaltis for being willing to take on a student from another university and for all of their patience and guidance throughout this process. Second I must thank Tod Lauer who first thought of applying principal components to these simulations, was indispensable to the work presented in Chapter 5, and has become a wonderful mentor. I must also thank C.K. Chan, Aleksander Sadowski, and Ramesh Narayan who ran the GRMHD and ray-tracing simulations used in the majority of this work. I also want to acknowledge C.K. Chan's patience in answering my many coding questions and for being a valuable collaborator. Additionally, I must acknowledge my other collaborators Junhan Kim, and Dan Marrone who contributed significantly to the work presented here. Finally, I would like to thank Professor Omer Blaes for going along with my crazy plans and ideas despite his better judgement.

I gratefully acknowledge support from NSF GRFP grant DGE 1144085 and NSF PIRE grant 1743747. All ray tracing and principal components analysis calculations were performed with the `El Gato` GPU cluster at the University of Arizona that is funded by NSF award 1228509.

Curriculum Vitæ

Lia Medeiros

Education

2019	Ph.D. in Physics, University of California, Santa Barbara
2016	M.S. in Physics, University of California, Santa Barbara
2013	B.S. in Physics and Astrophysics, University of California, Berkeley

Publications

1. "A Model for Anisotropic Interstellar Scattering and its Application to Sgr A*"
   Psaltis, Dimitrios, Johnson, Michael, Narayan, Ramesh, **Medeiros, Lia**, Blackburn, Lindy, Bower, Geoff
   2018 submitted to The Astrophysical Journal
2. "GRay2: A General Purpose Geodesic Integrator for Kerr Spacetime"
   Chan, Chi-kwan, **Medeiros, Lia**, Özel, Feryal, Psaltis, Dimitrios
   2018 The Astrophysical Journal, 867:59 (11pp)
3. "Principal Component Analysis as a Tool for Characterizing Black Hole Images and Variability"
   Medeiros, Lia, Lauer, Tod R., Psaltis, Dimitrios, Özel, Feryal
   2018 The Astrophysical Journal, 864:7 (16pp)
4. "GRMHD Simulations of Visibility Amplitude and Phase Variability for Event Horizon
   Telescope Images of Sgr A*"
   Medeiros, L., Chan, C.K., Özel, F., Psaltis, D., Kim, J.H., Marrone, D.P., Saḍowski, A.
   2018 The Astrophysical Journal, 856:163 (13pp)
5. "Variability in GRMHD Simulations of Sgr A*: Implications for EHT Closure Phase Observations"
   Medeiros, L., Chan, C.K., Özel, F., Psaltis, D., Kim, J.H., Marrone, D.P., Saḍowski, A.
   2017 The Astrophysical Journal, 844:35 (13pp)
6. "Bayesian Techniques for Comparing Time-dependent GRMHD Simulations to Variable Event Horizon Telescope Observations"
   Kim, Junhan, Marrone, Daniel P., Chan, Chi-Kwan, **Medeiros, Lia**, Özel, Feryal, Psaltis, Dimitrios
   2016 The Astrophysical Journal, 832:156 (11pp)

7. "Fast Variability and mm/IR flares in GRMHD Models of Sgr A* from Strong-Field Gravitational Lensing"
   Chan, C.K., Psaltis, D., Özel, F., **Medeiros, L.**, Marrone, D.P., Saḑowski, A., & Narayan, R.
   2015 The Astrophysical Journal, 812:103 (13pp)

8. "Abundant cyanopolyynes as a probe of infall in the Serpens South cluster-forming region"
   Friesen, R. K., **Medeiros, L.**, Schnee, S., Bourke, T. L., Francesco, J. Di, Gutermuth, R., Myers, P. C.
   2013 Monthly Notices of the Royal Astronomical Society, 436, 1513–1529

Note for the reader

While it may seem weird for a single author to refer to oneself in the plural, I will do so from now on as a way to signify that I did not do this alone.

Abstract

Modeling Variability in Black Hole Images

by

Lia Medeiros

The Event Horizon Telescope (EHT), a mm-wavelength very long baseline interferometer (VLBI), aims to take the first ever resolved images of black holes at event horizon scales. Interferometers detect the complex Fourier components (visibilities) of a source and use image synthesis algorithms to reconstruct the image. A fundamental assumption of most image reconstruction algorithms is that the source remains stationary throughout the length of the observation. A primary target for the EHT is the Galactic center black hole Sagittarius A* (Sgr A*), which is known to be variable on timescales significantly shorter than the observational timescale for the EHT. We use magnetohydrodynamic simulations and radiative transfer calculations in general relativity to characterize the effect of intrinsic source variability on interferometric observables. We show that intrinsic source variability will significantly affect conventional image reconstruction techniques and that variability must be taken into account for both image synthesis and model fitting. Furthermore, we explore the utility of Principal Component Analysis (PCA) to characterize the structural variability in GRMHD simulations of Sgr A* and find that simulations can be compactly represented with a PCA-derived basis of eigenimages.

This allows for detailed comparisons between variable observations and time-dependent models.

Contents

Chapter 1

Introduction

Our current understanding of black holes assumes they are described by the Kerr solution to Einstein's equations. As of yet, this assumption remains largely untested. A promising avenue for testing the Kerr solution is by detecting the shadow a black hole casts on the surrounding emission. The shadow of a Kerr black hole will have a diameter of $(5 \pm 0.2)GM/c^2$ (where M is the black hole mass, G is the gravitational constant, and c is the speed of light) independent of its spin (see Figure 1.1 for the full range of Kerr shadows, see also Johannsen & Psaltis 2011). Therefore, measuring the size and shape of the shadow of a black hole of known mass and distance constitutes a null hypothesis test of the Kerr metric (Psaltis et al., 2015b). The 1.3 mm-wavelength Very Long Baseline Interferometry (VLBI) experiment known as the Event Horizon Telescope (EHT) aims to take the first image of a black hole to both test general relativity (GR) in the strong-field regime and probe the turbulent accretion flow around supermassive black holes.

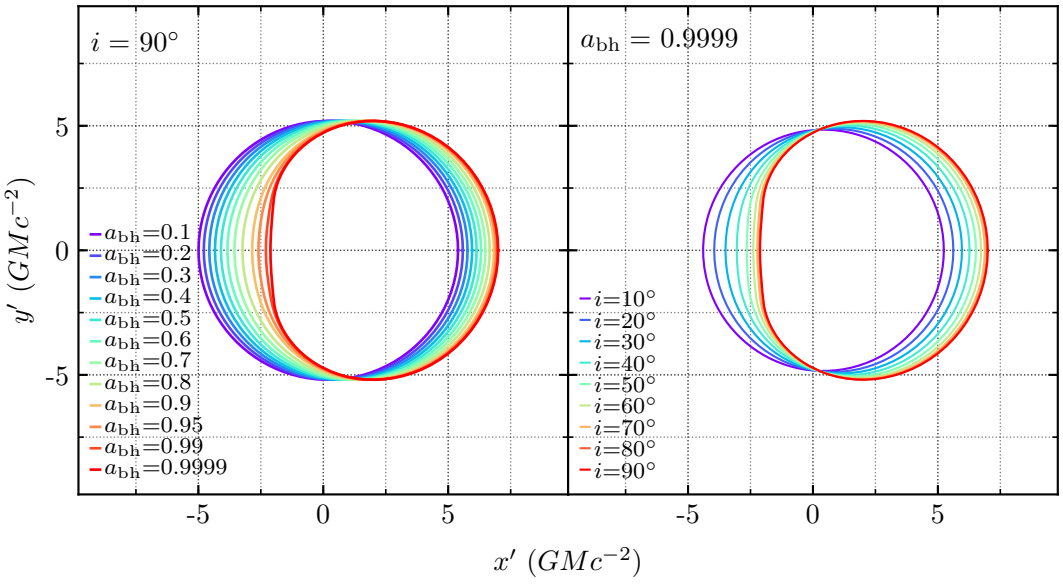

Figure 1.1 Several black hole shadows that result from the Kerr metric as a function of the black hole spin, $a_{\rm bh}$ (right), and the inclination of the observer, i (left). Here we assume that the spin vector points up. For all but the most rapidly spinning black holes viewed by equatorial observers, the shadow has a nearly circular shape and the radius of all of these shadows is between $4.8GM/c^2$ and $5.2GM/c^2$.

The EHT array consists of a large number of telescopes spread all over the world, with baselines ranging from Arizona to Hawaii and from the South Pole to Europe. It measures interferometric visibilities and uses them to generate the first-ever black hole images with horizon scale resolution (Doeleman et al. 2009a). The EHT performed the first observations with this globe-spanning array in April 2017; data are currently being correlated, calibrated, and analyzed. The telescopes that participated in the April 2017 observations are shown in Figure 1.2.

One of the primary observing targets for the EHT is Sagittarius A* (Sgr A*), the supermassive black hole at the center of our Galaxy. Sgr A* is an ideal candidate for the EHT since it has the largest angular size on the sky among the known nearby black

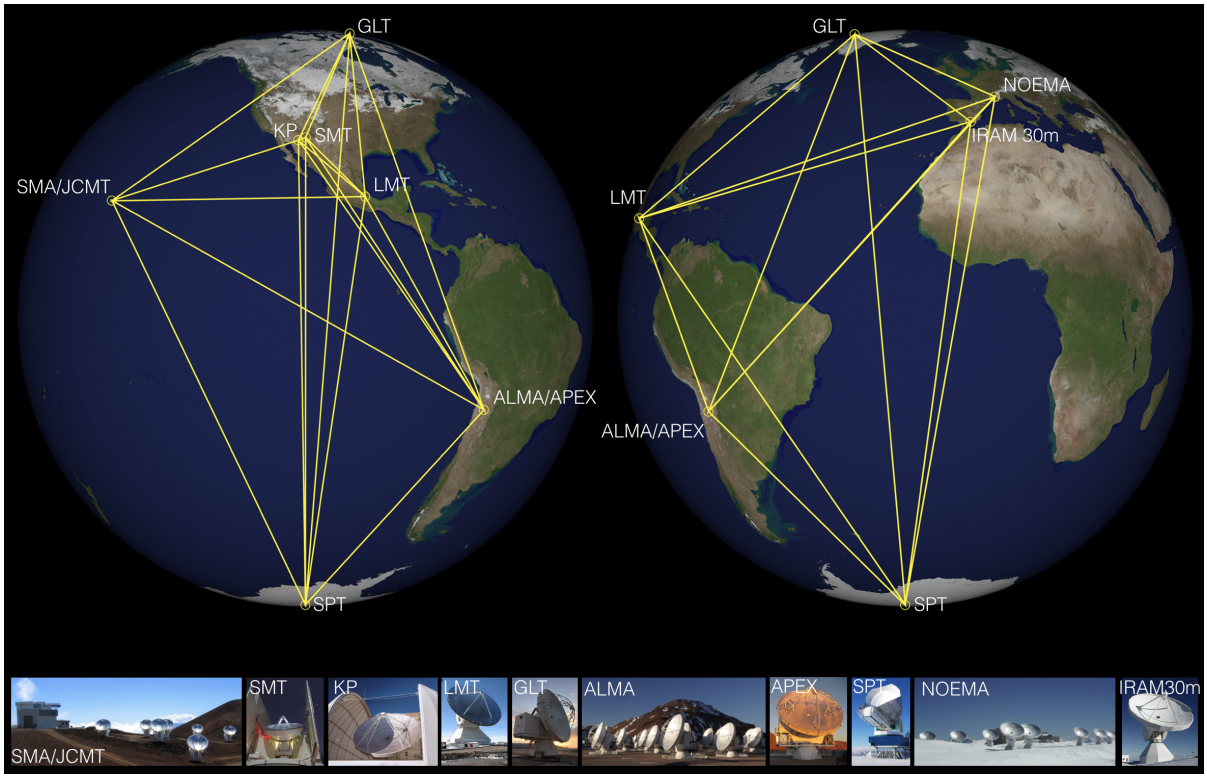

Figure 1.2 The telescopes that comprise the EHT array and their locations on Earth. The telescopes involved in the April 2017 observations were the Large Millimeter Telescope (LMT) on Volcan Sierra Negra, Mexico, the Submillimeter Telescope (SMT) on Mt. Graham, Arizona, the Submillimeter Array (SMA) on Maunakea, Hawaii, the James Clerk Maxwell Telescope (JCMT) also on Maunakea, Hawaii, the Atacama Large Millimeter/submillimeter Array (ALMA) in Atacama, Chile, the Atacama Pathfinder EXperiment (APEX) also in Atacama, Chile, the South Pole Telescope (SPT) at the South Pole, and the Institut de Radioastronomie Millimetrique (IRAM) 30 meter telescope on Pico Veleta in the Spanish Sierra Nevada. The Greenland Telescope (GLT), in Greenland, joined the array for the 2018 observations and Kitt Peak (KP), in Arizona, and the NOrthern Extended Millimeter Array (NOEMA), in the French Alps, are expected to join the array soon. (Image Credit: D. Marrone/University of Arizona)

holes (Johannsen et al., 2012), a well measured mass and distance (Ghez et al., 2008; Gillessen et al., 2009), and has been extensively studied at a variety of wavelengths for over a decade (see Baganoff et al. 2001 and Genzel et al. 2003 for early studies). The EHT also observed the black hole at the center of M87 since that black hole is $\sim 1,000$

times more massive and $\sim 1,000$ times farther away, such that it subtends approximately the same size on the sky. In this dissertation we focus primarily on Sgr A*, since the well constrained mass measurement makes it the ideal source to test general relativity.

Numerous observations and studies in the past few decades have established the fact that black hole accretion flows are highly variable. X-ray observations of galactic black hole binaries reveal a variability spectrum characterized by red noise as well as distinct high-frequency quasi-periodic components (see, e.g., van der Klis 2000; Remillard & McClintock 2006). Similarly, multi wavelength observations of nearby AGN, including Sgr A*, show variability on timescales ranging from hours to months (see, e.g., Genzel et al. 2003; Marrone et al. 2008; Porquet et al. 2008; Do et al. 2009, and Neilsen et al. 2015). The EHT itself has also observed variability at 1.3 mm (Fish et al., 2011), indicating that Sgr A*is structurally variable on scales of a few Schwarzschild radii. This variability is not surprising. It is understood to be the result of the turbulent accretion flows as well as a potential manifestation of the unique black hole spacetime near its horizon (see, e.g., Rauch & Blandford 1994; Chan et al. 2015a). Because of this, it is expected that the images for Sgr A*and M87 at mm wavelengths will also be variable at dynamical timescales near their event horizons.

Black hole variability is an important consideration for the EHT. At event horizon scales, the dynamical timescale for Sgr A* is between 5 and 30 minutes depending on the spin of the black hole[1]. However, since the EHT is a VLBI instrument, it relies

[1]Here we approximate the dynamical timescale as the period of a Keplerian orbit with radius equal to the innermost stable circular orbit (ISCO) radius. Specifically we use: $t_{\rm dynamical} = 2\pi(R^3_{\rm ISCO}/GM)^{1/2}$, where $R_{\rm ISCO} = 6GMc^{-2}$ for a massive particle orbiting a Schwarzschild black hole and approaches

on the rotation of the Earth to trace baseline tracks in $u - v$ space. A single night of observation can take over ten hours, over an order of magnitude longer than the dynamical timescale for Sgr A*. Consequently, different data points along baseline tracks correspond to different realizations of the turbulent structure of Sgr A*. Traditional image reconstruction algorithms rely on the assumption that the black hole image structure remains stationary on typical observation timescales, which range from about one hour for the shortest tracks to over ten hours for the longest.

It is critical to understand how the sources may vary over timescales comparable to those observations in order to design and implement proper image reconstruction algorithms (see, e.g., Lu et al. 2016; Johnson et al. 2017; Bouman et al. 2017 for early attempts). It is also important to study and characterize the variability predicted by different accretion flow models, in order to investigate whether the mode and amplitude of predicted variability agrees with observations (see Kim et al. 2016). Both these issues acutely affect the analysis and interpretation of the data of Sgr A*.

Improvements in our theoretical understanding of black hole accretion have led to a convergence in the properties of GRMHD simulations (see, e.g., Mościbrodzka et al. 2009a; Shcherbakov & Baganoff 2010; Dexter et al. 2010, 2012; Shcherbakov et al. 2012; Mościbrodzka & Falcke 2013; Chan et al. 2009, 2015a,b) and semi-analytic models inspired by them (e.g., Broderick & Loeb 2006) that can account for most observed characteristics of Sgr A*. A variety of these models has been directly compared to early EHT data in order to perform parameter estimation and model comparison.

$2GMc^{-2}$ in the limit of a maximally spinning black hole.

Chan et al. (2015a,b) reported a series of GRMHD simulations with high spatial and time resolution (these simulations will be discussed in depth in Chapter 2). Chan et al. (2015a) used these simulations to study the variability as a function of wavelength for the source-integrated flux of Sgr A* and found two kinds of variability: long timescale flaring events and shorter timescale, persistent variability originating from the turbulent flow. Some of these models are able to reproduce the flaring events observed from Sgr A* at longer wavelengths but additional physics (such as non-thermal electrons) is required to reproduce X-ray flares (Ball et al. 2016; see also Chan et al. 2009; Dodds-Eden et al. 2010).

In this dissertation we will employ the set of models discussed above to explore how the turbulent accretion flow will affect the structure of the emission region at 1.3 mm and how this variability will be manifest in EHT observables. Interferometers measure the complex Fourier components of the image. The amplitude and phase of the Fourier components are commonly referred to as the visibility amplitude and the visibility phase respectively. In mm VLBI the water vapor in the atmosphere interferes with our visibility phase measurements so the EHT must rely on closure phases, the clever addition of phase at three baselines such that the effect of the atmosphere at each telescope cancels. Because the EHT will not observe absolute visibility phases we cannot combine the visibility amplitude and phase into complex numbers, but rather must treat visibility amplitude and closure phase separately. Likewise, we will treat these two observables separately in this dissertation.

This dissertation is organized as follows. In Chapter 2 we introduce accretion disks and discuss the simulations that are used in this dissertation. In Chapter 3 we explore how the variability in the GRMHD simulations is manifest in visibility amplitudes. The effect of variability on absolute phases and closure phases is discussed in Chapter 4. In Chapter 5 we explore the use of principal components analysis to both understand and characterize the variability seen in the GRMHD simulations, but also as a means to fruitfully compare GRMHD simulations to EHT data. We conclude and discuss future work in Chapter 6.

1.1 Previously Published Work

1. The content in Chapter 2 is mostly taken from Medeiros et al. (2018a) and Medeiros et al. (2017).

2. The content of Chapter 3 first appeared in Medeiros et al. (2018a).

3. The content of Chapter 4 first appeared in Medeiros et al. (2017).

4. The content of Chapter 5 first appeared in Medeiros et al. (2018b).

Chapter 2

Simulations of Accreting Black Holes

Accretion flows around black holes can be divided into two general categories based on their radiative efficiency and the resulting temperature of the gas. Cold accretion flows have temperatures significantly lower than the virial temperature (defined as $T_{\rm vir} \sim GMm_p/kR$, where m_p is the proton mass, k is Boltzmann's constant) of the flow, and have relatively high accretion rates. If the accretion rate is close to but smaller than the Eddington accretion rate ($\dot{M} \lesssim \dot{M}_{Edd.}$)[1], the flow can settle into a geometrically thin and optically thick disk and can radiate away its energy efficiently through thermal emission. The thin disk model of Shakura & Sunyaev (1973) describes these kinds of flows (see also Novikov & Thorne 1973; Lynden-Bell & Pringle 1974 and reviews by Pringle 1981; Frank et al. 2002; Kato et al. 2008; Abramowicz & Fragile 2013, and Blaes 2014). If the accretion rate gets too high ($\dot{M} \gtrsim \dot{M}_{Edd.}$), the flow becomes optically thick and

[1]Here we define the Eddington accretion rate as $\dot{M}_{Edd.} \equiv 10L_{Edd.}/c^2 = 10(4\pi GMm_p c/(\sigma_{\rm T}))/c^2 = 1.39 \times 10^{18}(M/M_\odot){\rm gs}^{-1}$, where M is the mass of the black hole, m_p is the proton mass, and $\sigma_{\rm T}$ is the Thompson scattering cross section for the electron.

the timescale for photons to diffuse out is long compared to accretion timescales. The trapped photons get advected inward leading to a thicker disk. This is referred to as the slim disk model, or optically thick advection-dominated accretion flow (see e.g., Katz 1977; Begelman 1979; Begelman & Meier 1982; Abramowicz et al. 1988; Chen & Taam 1993, and Ohsuga et al. 2005).

Hot accretion flows that are relevant for nearby, supermassive black holes and are, thus, of interest to us here are geometrically thick and optically thin. They have accretion rates significantly below $\dot{M}_{Edd.}$ and have temperatures close to the virial temperature of the flow (see e.g., Yuan & Narayan 2014 and Blaes 2014 for reviews). The first model for a hot accretion flow was developed by Shapiro et al. (1976). This model predicted a two-temperature plasma, an important component of hot accretion flows since the energy transfer between the electrons and ions is inefficient due to the collisionless nature of these flows. However, this early model was thermally unstable. Ichimaru (1977) showed that advection played an important role in hot flows, since the viscously dissipated accretion energy can go into heating the flow. The inclusion of advection created a thermally stable hot accretion flow which was then further developed by Rees et al. (1982); Narayan & Yi (1994, 1995a,b); Abramowicz et al. (1995), and Chen et al. (1995). These flows are frequently referred to as Advection Dominated Accretion Flows (ADAFs), or Radiatively Inefficient Accretion Flows (RIAFs) since hot accretion flows are usually radiatively inefficient. The Galactic center black hole (Sgr A*) is expected to be an ADAF since its accretion rate ($\dot{M} \approx 10^{-9} - 10^{-7} M_{\odot} \mathrm{yr}^{-1}$, e.g., Marrone et al.

2007) is much lower than $\dot{M}_{Edd.}$. This is also true for the black hole in M87 and other supermassive black holes in the Virgo cluster (see e.g., Di Matteo et al. 2003). Because of this, we will focus primarily on hot accretion flows in the remainder of this dissertation.

2.1 GRMHD Simulations

Modeling accretion flows around black holes has been a decades-long effort. First attempts at simulating black hole accretion flows used hydrodynamic codes and an α-like prescription for the viscous stress (Igumenshchev et al. 1996; Stone et al. 1999; Igumenshchev & Abramowicz 1999, 2000; Igumenshchev et al. 2000; De Villiers & Hawley 2002, and Fragile & Anninos 2005). Angular momentum transport in hot accretion flows primarily happens through magnetohydrodynamic (MHD) turbulence driven by the magnetorotational instability (MRI; Balbus & Hawley 1991, 1998). Eventually, numerical algorithms were developed for simulating the interaction between the ionized gas in the flow and the expected magnetic fields. These algorithms solved the MHD equations instead of the hydrodynamic equations. In later studies, the equations were reformulated in general relativity to include the effects of the black hole spacetime, leading to general relativistic magnetohydrodynamic (GRMHD) equations. A few examples of MHD and GRMHD codes include ZEUS (Stone & Norman 1992a,b), HARM Gammie et al. (2003), the spectral code described in Chan et al. (2005), the GRMHD code of De Villiers & Hawley (2003), COSMOS++ (Anninos et al., 2005), and ATHENA (Stone et al., 2008).

The simulations of Sgr A* discussed in this dissertation are the result of 3 dimensional

GRMHD simulations run using the HARM code (see Narayan et al. 2012; Sądowski et al. 2013, and Chan et al. 2015b for more details on these simulations). These simulations were initialized with a thick torus of gas a few hundred gravitational radii[2] away from the central Kerr black hole and a seed magnetic field. The simulations discussed in this work do not take into account the effect of radiation pressure on the dynamics of the flow but significant advances have been made recently in simulating this effect (see e.g., Davis et al. 2012; Jiang et al. 2014; Sądowski et al. 2017; Chael et al. 2018; Ryan et al. 2018; Morales Teixeira et al. 2018; Curd & Narayan 2019).

The GRMHD simulations discussed in this dissertation span a range of black hole spin (a=0 to 0.9) and magnetic field configurations. Specifically, we explored two different initial magnetic field configurations. The first consists of multiple small loops and leads to weak, turbulent fields near the horizon and an emitting region at 1.3 mm that is dominated by the disk region (SANE, Standard and Normal Evolution; see also McKinney & Gammie (2004); Hawley & Krolik (2006); Shiokawa et al. (2012); Mościbrodzka & Falcke (2013); Mościbrodzka et al. (2014) for other SANE-like GRMHD simulations). The second consists of a single initial magnetic field loop and leads to coherent magnetic field structures near the horizon and an emitting region at 1.3 mm that is dominated by the jets (MAD, Magnetically Arrested Disk, see, e.g., Tchekhovskoy et al. 2012; McKinney et al. 2012).

[2]We define one gravitational radius as GM/c^2, where M is the mass of the central black hole, G is the gravitational constant, and c is the speed of light.

2.2 Radiative Transfer and Ray Tracing Simulations

The GRMHD simulations are run for many dynamical timescales, ensuring that steady-state is reached and simulation outputs sample the range of variability encountered in these flows. Radiative transfer and ray tracing simulations are then run as a post-processing step on the outputs from the GRMHD simulations. These simulations solve the geodesic equations in the Kerr metric to evolve the trajectories of photons backwards from the plane of the observer and compute the interactions of the photons with the flow. We include thermal bremsstrahlung and synchrotron emission but neglect non-thermal emission and Compton scattering (see Ball et al. 2016 for the effects of non-thermal emission on these simulations). These calculations were performed using the fast GPU-based ray tracing code `GRay` (Chan et al., 2013), which allowed us to calculate wavelength-dependent images for each snapshot in the simulations. Our simulations have a time resolution of $10\,GMc^{-3}$, equivalent to 212 s, for the mass of Sgr A*, which is $M = 4.3 \times 10^6\,M_\odot$. Each simulation has 1024 time steps resulting in a total time span of approximately 60 hours for each simulation. `GRay` employs the fast light approximation in which the speed of light is assumed to be infinite (see Chan et al. 2018 for the new version of this code, `GRay2`, that does not make this assumption and see, e.g., Dolence et al. (2009); Mościbrodzka et al. (2011); Shiokawa et al. (2012) for models allowing for a finite speed of light). At horizon scales, the light crossing time is ~ 20 s, which is an order of magnitude smaller than our time resolution.

The simulations do not evolve the thermodynamics of the electrons because electron

heating occurs at scales that are much smaller than the spatial resolution of the simulations. Instead, we use physically motivated but simplistic models to assign a temperature to the electrons based on the ion temperature and other parameters in the flow. As with most other such prescriptions, we base the electron-to-ion heating ratio on the plasma β, defined as $\beta = P_{\rm gas}/P_{\rm mag}$, the ratio of gas to magnetic pressure. Specifically, we use a threshold in plasma β to define two regions: the disk ($\beta > 0.2$) and the funnel, which is a low density region dominated by magnetic pressure ($\beta < 0.2$). We use a constant electron-to-ion temperature ratio for the disk region and consider two possible, physically-motivated models for the funnel region. In the first model, we assume a constant electron-to-ion temperature ratio (which is different than the ratio for the disk region) and in the second, a constant electron temperature to allow for the case where electron conduction is very efficient. These models reproduce a disk/funnel structure that is similar to the results discussed in Ressler et al. (2017), who use a more detailed treatment developed to model particle heating in the solar wind (Howes, 2010, 2011). For each or the GRMHD simulations, we varied the thermodynamic prescription for the electrons described above, the accretion rate, and the inclination of the observer to investigate the effects of these parameters.

2.3 The Best Fit Models

Out of a large number of simulations, we identified five models which best fit the previous multi-wavelength observations of Sgr A* (Chan et al., 2015b). The specific criteria used

to constrain these models are *(a)* the flux and the spectral slope at 10^{11}–10^{12} Hz, *(b)* the flux at $\simeq 10^{14}$ Hz that falls within the observed range of the highly variable infrared flux, *(c)* an X-ray flux that is consistent with 10% of the observed quiescent flux, which is the percentage which has been attributed to emission from the inner accretion flow (Neilsen et al., 2013), and *(d)* a size of the emission region that is consistent with the size determined by the early EHT observations Doeleman et al. (2008). Figure 2.1 shows the mean broadband spectra of the five best fit models and the observational constraints used to select the models. All of the best-fit models have an observer inclination of $i = 60°$ with respect to the spin axis of the black hole. Table 2.1 summarizes the parameters of the models we consider.

Figure 2.2 shows the light curves for the five models we consider. These light curves were calculated by computing the source integrated flux at $\lambda = 1.3$ mm from each model for each late-time snapshot during the ≈ 60 hrs of simulation time. Models A and B represent SANE flows and the same plasma model but differ on the choice of black hole spin: Model A has $a = 0.7$, while Model B has $a = 0.9$. Both models A and B show large amplitude, short timescale variability that was shown to be consistent with broadband observations in Chan et al. (2015a). Models D and E have the same black hole spin of $a = 0.9$ and the same MAD configuration, but differ on the choice of the plasma model used. Both models D and E show only long timescale, low amplitude variability. Model C consists of a MAD flow and a black hole spin of $a = 0$. Model C shows very fast, quasi-periodic, low amplitude variability.

Table 2.1. Summary of our Five Models

Name	a	B_0	$n_{\rm e}$	$\theta_{\rm disk}$	$T_{\rm e,funnel}$	$\theta_{\rm funnel}$
A	0.7	SANE	6.885×10^7	0.02371	56.23	. . .
B	0.9	SANE	5.465×10^7	0.01000	31.62	. . .
C	0.0	MAD	5.932×10^8	0.00056	. . .	0.01000
D	0.9	MAD	1.599×10^8	0.00075	1.78	. . .
E	0.9	MAD	1.599×10^8	0.00075	. . .	0.00316

Note. — Summary of the five best fit models from Chan et al. (2015b). The first column lists the model names used throughout this dissertation. The second and third columns list the black hole spin (a) and the accretion flow state that depends on the initial magnetic field geometry (B_0). The fourth column refers to the density normalization (n_e) while the fifth column refers to the electron-ion temperature ratio in the disk ($\theta_{\rm disk}$). The last two columns refer to the treatment of the funnel region, we consider two plasma models one with a constant electron temperature for the funnel ($T_{\rm e,funnel}$), the other with a constant electron-ion temperature ratio for the funnel ($\theta_{\rm funnel}$).

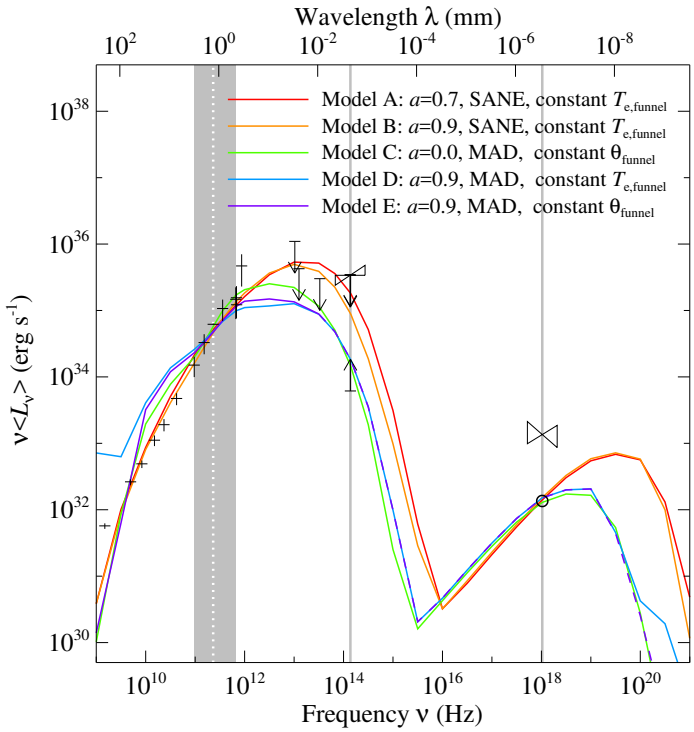

Figure 2.1 The colored curves show the mean broadband spectra for the five models discussed throughout this dissertation, note that Model E is plotted as a dashed purple curve for clarity when it overlaps other models. The bowties, arrows, and crosses are the data points that were used in Chan et al. (2015b) to constrain the models. Chan et al. (2015b) performed a least-squares fit to the radio spectrum between $\nu \approx 1011$ Hz and $\nu \approx 1012$ Hz (denoted by the gray band). The gray line at $\nu \approx 1018$ Hz marks the frequency where the models were fit to 10% of the observed quiescent X-ray flux (the open circle below the bowtie) to fix the density normalization of the flow. The models were also constrained to fit a range of fluxes at $\nu \approx 1014$ Hz, also denoted by a gray line. The dotted white line denotes $\lambda = 1.3$ mm where the models were constrained to fit the size of the emission region measured by the EHT.

Figure 2.3 shows the average 1.3 mm wavelength images for the five simulations we consider. Models A and B, the SANE models, have 1.3 mm wavelength emission regions that are dominated by the thick accretion disk. The emission from these models is asymmetric due to the effects of relativistic Doppler beaming, because the part of the orbiting accretion flow that is coming towards the observer is beamed and appears

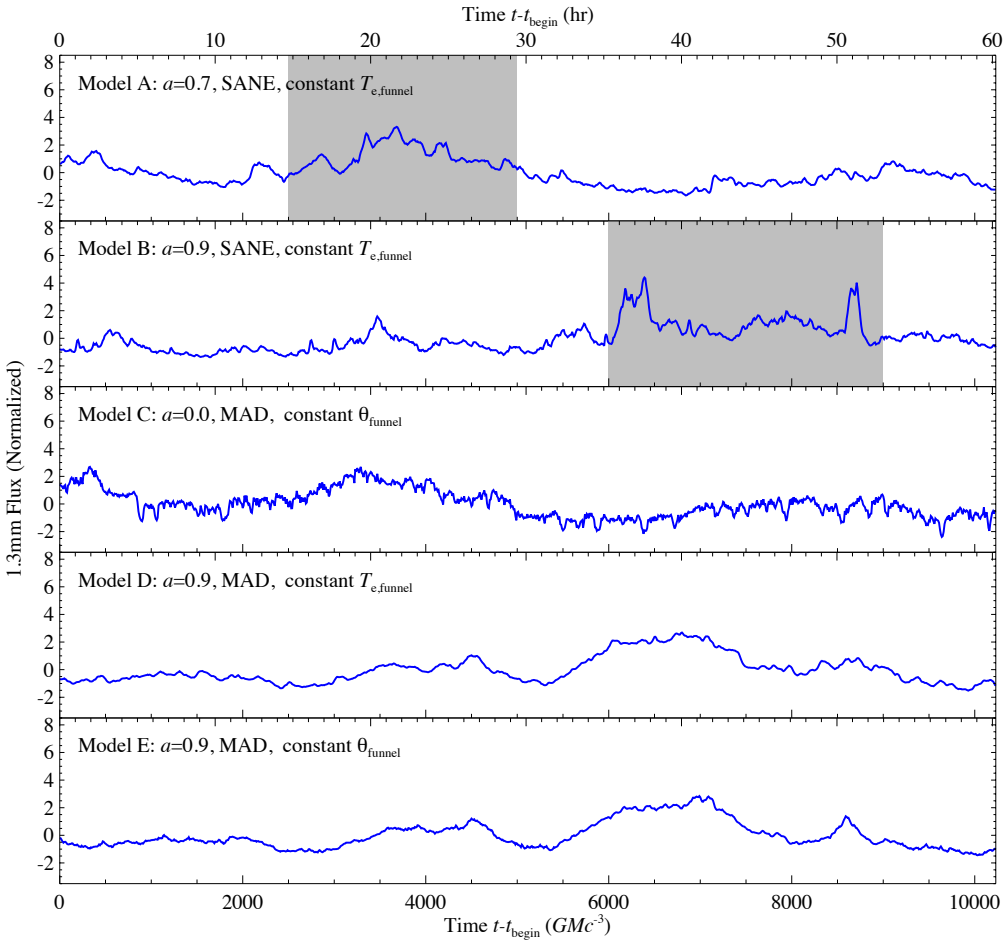

Figure 2.2 The 1.3 mm flux, centered (subtracted by the mean) and normalized by the variance, as a function of time for the five simulations we explore (see also Chan et al. 2015a,b). Models A and B, the SANE models, have significant flaring events, shown in grey, which we have excluded from all calculations of averages in Chapter 3. The models have a time resolution of $10\,M$, which is approximately equal to 212 s for the mass of Sgr A* and a total duration of ≈ 60 hours.

brighter than the part that is moving away from the observer. The MAD models (C, D, and E), however, have 1.3 mm wavelength emission regions that are dominated by the funnel regions. Model C is unique in that its emission is dominated by the footpoints of the funnel region with negligible emission coming from the disk. Models D and E have emission coming from both the Doppler-beamed disk and the funnels.

The red circles superimposed on the images correspond to the size of the black hole

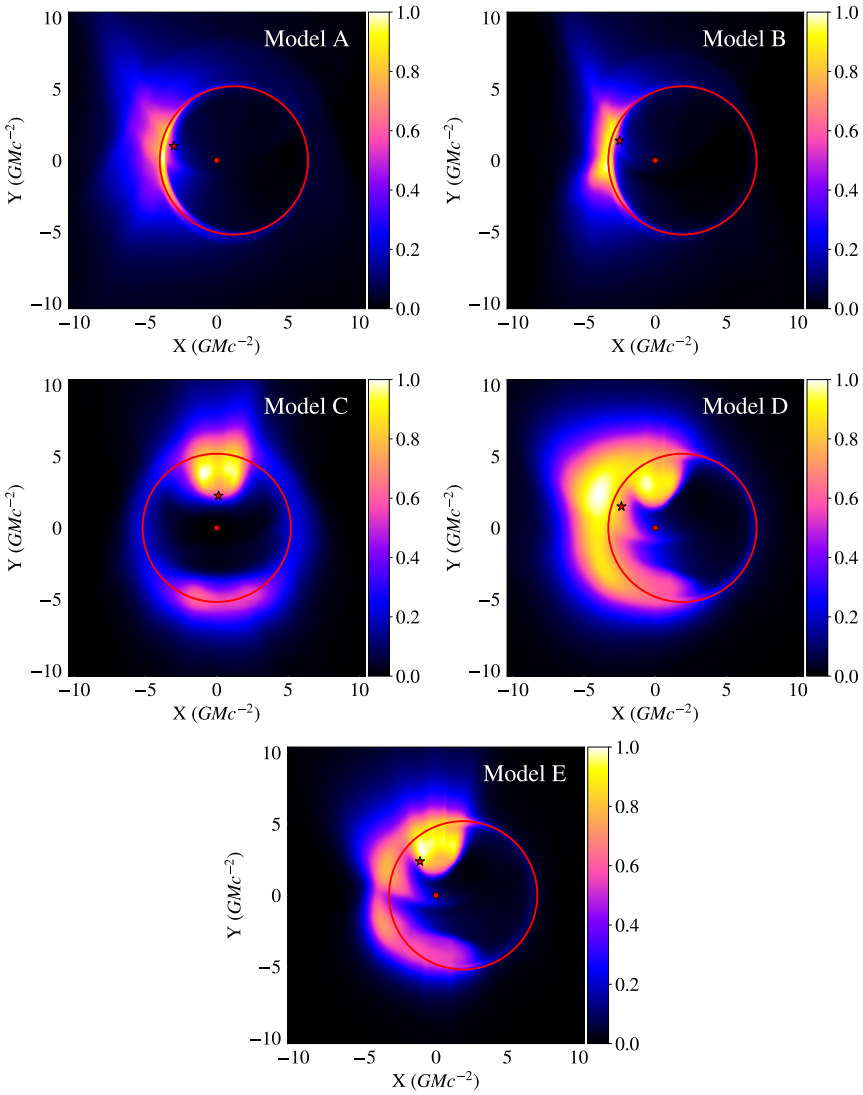

Figure 2.3 The average 1.3 mm images of the five models we consider. The SANE models (A and B) have most of their emission originating from the disk region, while the MAD models (C, D, and E) have significant emission originating from the footpoints of the funnels. Model C is unique, with negligible emission from the disk and a black hole spin of zero. The red circles indicate the expected size of the black hole shadow according to general relativity. The red stars correspond to the location of the center of light for each model (see Chapter 4) while the red dots denote the location of the center of the black hole. Since the orientation of Sgr A* on the sky is not known, these images show an arbitrary orientation where the spin axis of the black hole points North. The maximum intensity in each panel has been normalized to unity.

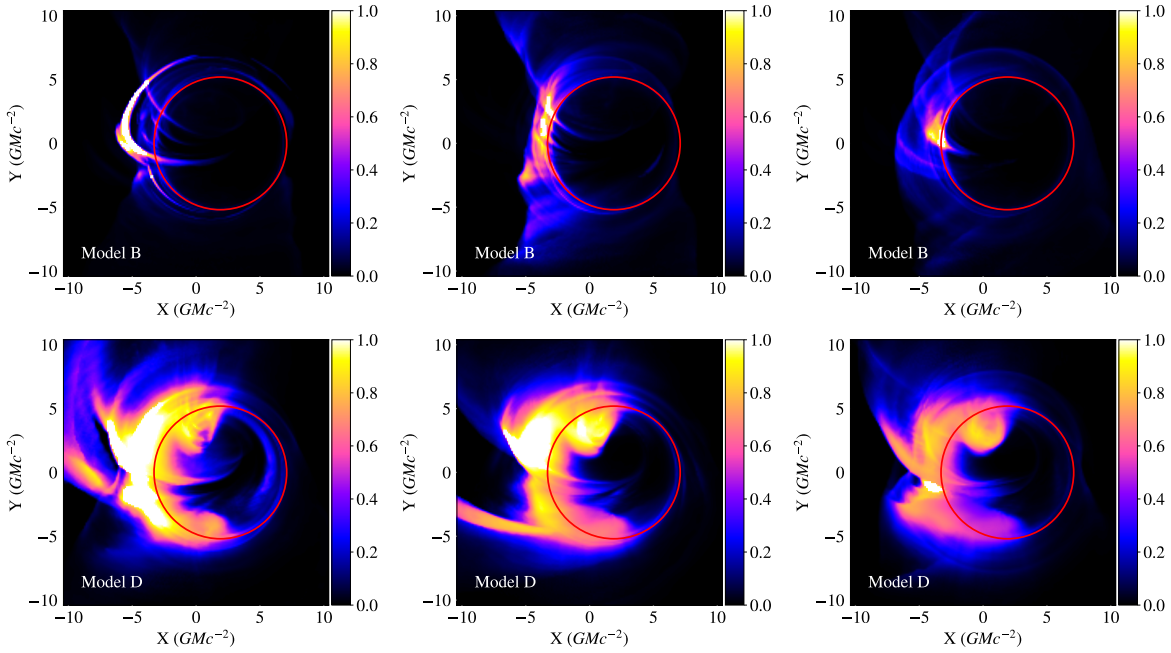

Figure 2.4 A few example snapshots from Model B (top row) and Model D (bottom row) showing significant structural variation of the image with time. All snapshots have the same brightness normalization such that differences in brightness between snapshots are real. Although SANE models are more variable, MAD models still show significant variability.

shadow predicted by general relativity. For comparison, the red dots show the location of the center of the black hole. Frame dragging effects cause the emission to be offset (red circles are not centered on the black hole) for models which have a non-zero spin. The red stars in the figures indicate the calculated center of light for each image. The center of light was used in the calculation of the Fourier transform of the image, as we will discuss in Chapter 4.

Figure 2.4 shows a few example snapshots from models B and D. We can see that the disk-dominated model (Model B) shows significant structural changes in the images with

time as opposed to a constant structure with varying flux. In large part, these variations are caused by short lived flux tubes that come in and out of the line of sight. Additionally, there is also significant variability in the thickness and structure of the crescent shape. The hybrid model (Model D) has a funnel component and a disk component in its emission region. In general, models like this show less overall variability than the disk-dominated models but still show significant structural changes with time.

Chapter 3

GRMHD Simulations of Visibility Amplitude Variability for Event Horizon Telescope Images of Sgr A*

In this chapter we explore how the variability seen in GRMHD simulations of accretion flows will be manifest in visibility amplitudes. Specifically, we aim to characterize and understand the variability in the location of salient features of black hole images in $u-v$ space, using these simulations. Our study allows us to explore the degree to which these salient features in the $u-v$ plane, which primarily determine the structures in the reconstructed images, evolve during the duration of an EHT imaging observation. It also helps us assess whether the location of such features can be used to measure fundamental properties of the black hole that are fixed, such as the size of the black hole shadow or

the black hole spin.

Because we want to quantify the time evolution of these features in the $u - v$ plane as predicted by GRMHD simulations, we do not simulate particular EHT observations, consider the effects of the Earth's rotation, or consider interstellar scattering. Of course, the variability in the visibility amplitudes that the EHT will measure will ultimately be a combination of the intrinsic source variability, the effect of the Earth's rotation, and of the scattering screen. However, our goal is not to simulate a mock observation or perform a parameter estimation. We rather aim to test the degree to which one of the key assumptions in VLBI image reconstruction, i.e., that the images can be treated as stationary, will affect the interpretation of Sgr A* observations.

To perform this analysis, we calculate and study the time-dependent visibilities at 1.3 mm for the five best-fit models discussed in Chapter 2. We employ analytic models to understand the behavior and significance of various features in the visibility amplitudes and use our simulations to investigate the ability of analytic models to capture the gross features of the black-hole images.

3.1 Time Dependence of Visibilities

Although Figure 2.3 shows resolved images of Sgr A* at 1.3 mm, the EHT is an interferometer and will measure the complex Fourier components of Figure 2.3. To explore the properties of the actual observables, we show in Figure 3.1 the average 1.3 mm visibility amplitudes for the five models. We calculated these visibility amplitudes by performing,

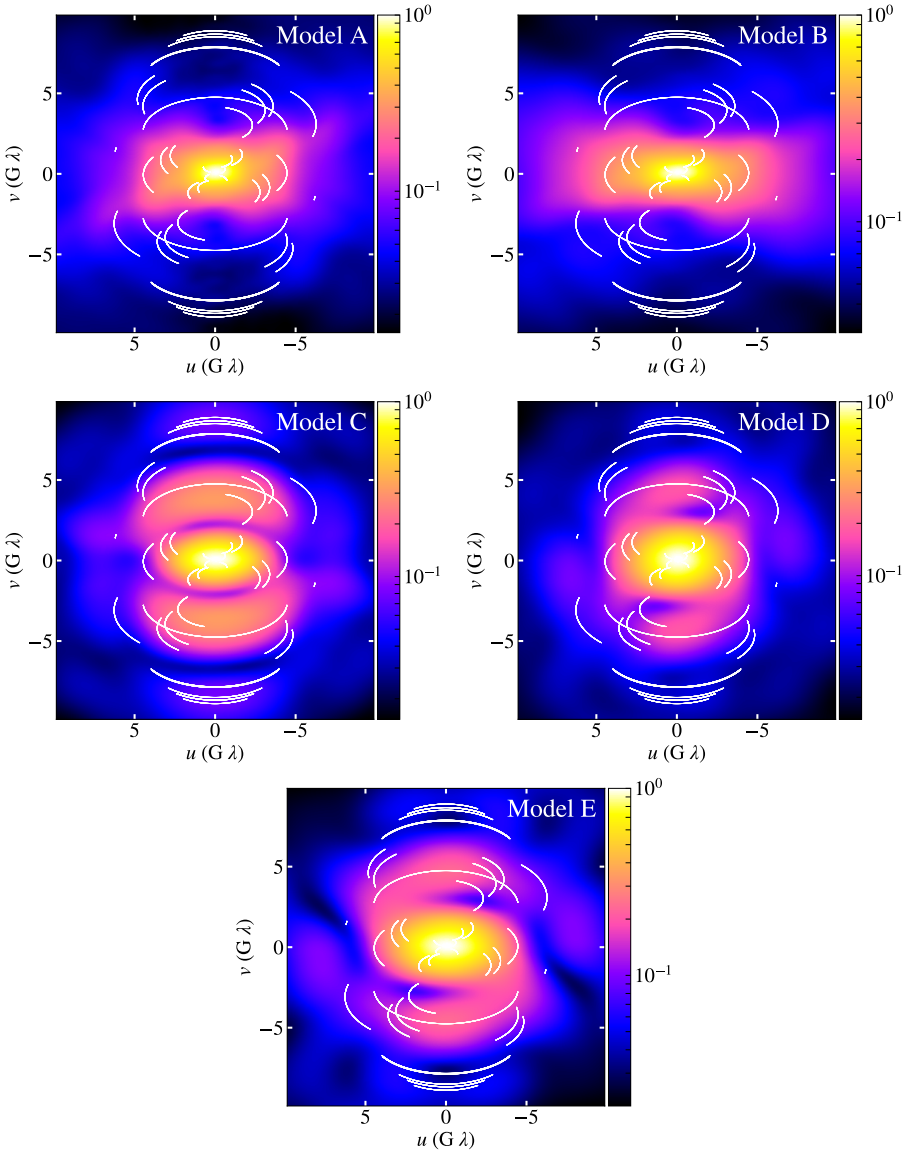

Figure 3.1 The average 1.3 mm visibility amplitudes, calculated by taking the magnitudes of the complex Fourier components of the two dimensional Fourier transforms, of each snapshot of the five simulations we consider and then averaging over the snapshots. The white lines denote the current and future tracks of the EHT baselines as the Earth rotates. Baselines are shown for an arbitrary N-S black hole orientation for illustrative purposes only. The maximum visibility amplitude in each panel has been normalized to unity.

on each snapshot, the two dimensional Fourier transform

$$V(u,v) = \iint I(\alpha,\beta) e^{-2\pi i(u\alpha+v\beta)} d\alpha d\beta, \tag{3.1}$$

where $\alpha \equiv X/D$, $\beta \equiv Y/D$, and D is the distance to Sgr A*, and then taking the mean magnitude of the complex Fourier components. The white lines are the current and planned tracks of the various baselines of the EHT shown for a particular N-S orientation of the black hole (see, e.g., Doeleman et al. 2009a). The visibility amplitude maps of models A and B appear elongated in the horizontal direction. This is because the Fourier transform is the conjugate of the original image and the original image is a crescent elongated in the vertical direction. Models C, D, and E show multiple emission peaks in the original image along the vertical direction. This results in multiple peaks in the visibility amplitude maps, along the same axis. Model C appears to be more symmetric in both the original image and its transform.

Even though the visibility maps shown in Figure 3.1 allow us to identify the gross features of the images, they do not faithfully represent the observations that the EHT will obtain. As discussed in the introduction, the EHT relies on the rotation of the Earth to increase its coverage of the $u - v$ plane and, therefore, make a better image. However, Sgr A* is variable on timescales that are much shorter than a day. Since the EHT will observe Sgr A* for multiple days each year for multiple years, it will measure a distribution of data points at each $u - v$ point along the baseline tracks. We now aim to quantify the effect of variability on the structure of the visibility amplitude.

3.1.1 SANE Models

The SANE models A and B have their 1.3 mm emission structure dominated by the disk and have crescent-like shapes. In Figures 3.2 and 3.3, we show the mean simulated images, the means of the visibility amplitudes of each snapshot, and the visibility amplitudes of the mean simulated images, for these SANE models. Note that the visibility amplitude is the magnitude of the Fourier transform of the image. Because calculating the amplitude is a non-linear operation, the order of operations for taking the mean and calculating the amplitude matters. Comparing the mean visibility amplitudes to the visibilities of the mean images reveals an expected but important consequence of variability. The visibilities of any snapshot (including of the average image) have significantly more structure than the average visibilities.

To explore the behavior of the structure of visibility amplitudes further, we turn our focus to the images from the individual snapshots. In the various panels of Figure 3.4, we show (a) the simulated images, (b) the projections of these images along directions parallel and perpendicular to the black hole spin axis, (c) the visibility amplitudes, and (d) the cross sections of the visibility amplitudes taken along directions parallel and perpendicular to the black hole spin axis for 5 snapshots from model B. The projection-slice theorem states that the Fourier transform of the projection of a two-dimensional image onto some axis is equal to a slice of the Fourier transform of the image as long as the slice is parallel to the projection axis and intersects the center of the visibility amplitude map. As a result, the cross sections of the visibility amplitudes shown in the rightmost

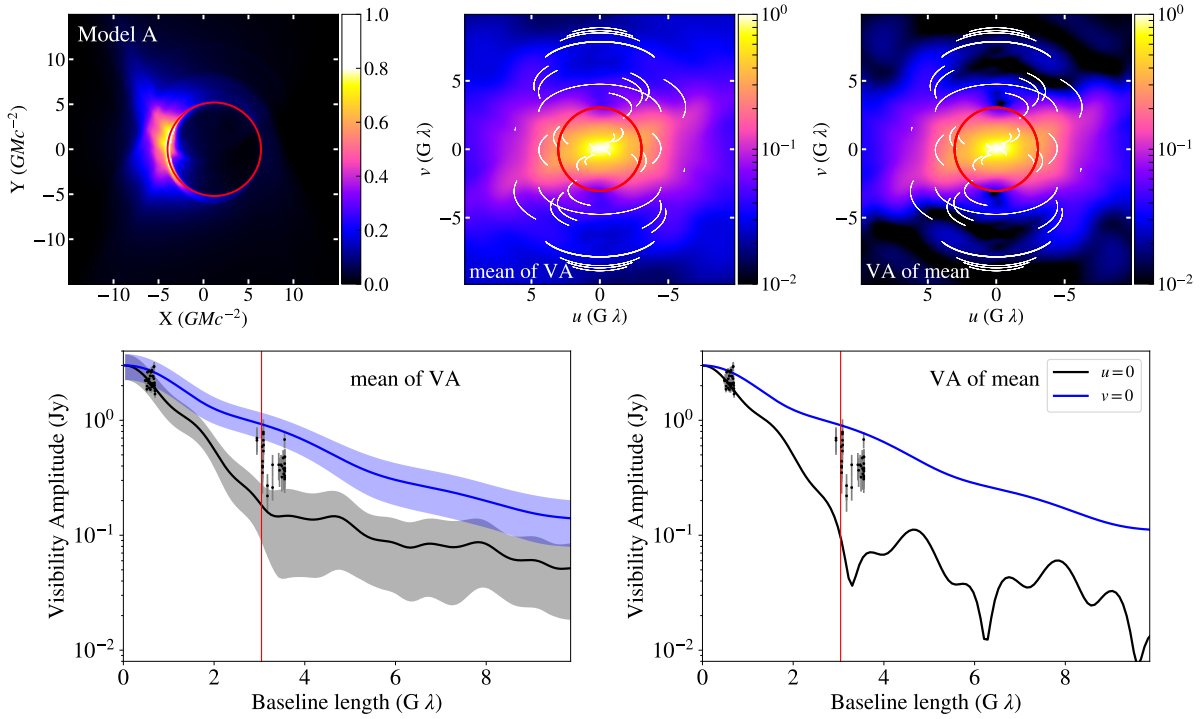

Figure 3.2 (Top Left) Mean simulated image of Model A. Red circle indicates the location of the black hole shadow. (Top Middle) Mean of the visibility amplitude of each snapshot. Red circle indicates the first null in the visibility amplitude of a thin photon ring located at the radius of the black hole shadow. (Top Right) Visibility amplitude of the mean simulated image. Red circle is the same as the top middle panel. (Bottom Left) Cross sections, taken parallel (black line and region) and perpendicular (blue line and region) to the black hole spin axis, of the top middle panel. These cross sections were not chosen to correspond to any particular EHT baselines. The colored regions are the 68% ranges of the mean visibilities at each baseline. Red line is the location of first null in the visibility amplitude of a thin photon ring located at the radius of the black hole shadow. (Bottom Right) Cross sections, taken parallel (black line) and perpendicular (blue line) to the black hole spin axis, of the top right panel. The red line is the same as the bottom left panel. The black points and error bars in the bottom panels are EHT data taken in 2007 and 2009 shown here for illustrative purposes only (Doeleman et al. 2008, Fish et al. 2011).

panels are just the one-dimensional Fourier transforms of the projections shown in the second column of panels. These cross sections are representative of the range of behavior of the two dimensional visibilities since the parallel cross section probes the closest deep

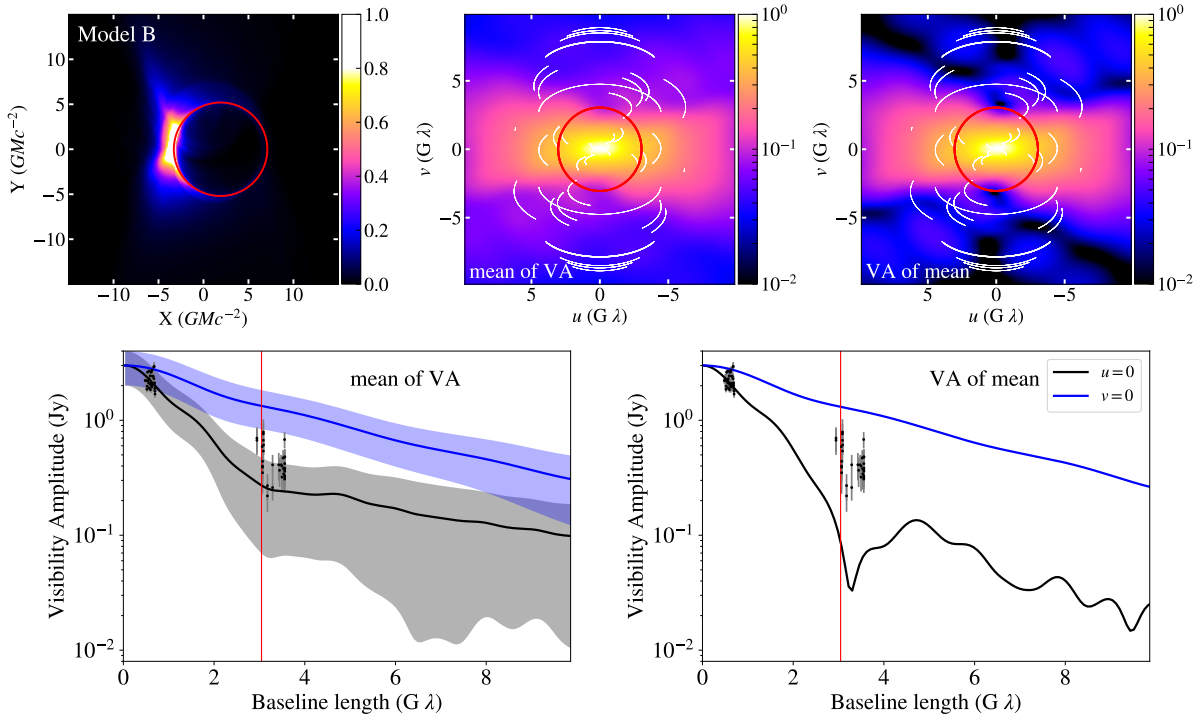

Figure 3.3 Same as Figure 3.2, but for Model B.

minimum to the zero baseline while the visibility amplitudes are smoothly decreasing in the perpendicular cross section. The cross sections are good representations for the range of behavior that could be observed for different orientations.

In the rightmost column, we see that the visibility amplitude cross sections perpendicular to the spin axis decrease slowly and smoothly while those parallel to the spin axis have a lot more structure. Particularly, the cross sections parallel to the spin axis often have minima, but the location and depth of these minima are variable. By taking the average of the visibility amplitudes, we lose all information about the minima and are left with a smoothly decreasing visibility amplitude, as was seen in the mean of the visibilities in Figures 3.2 and 3.3.

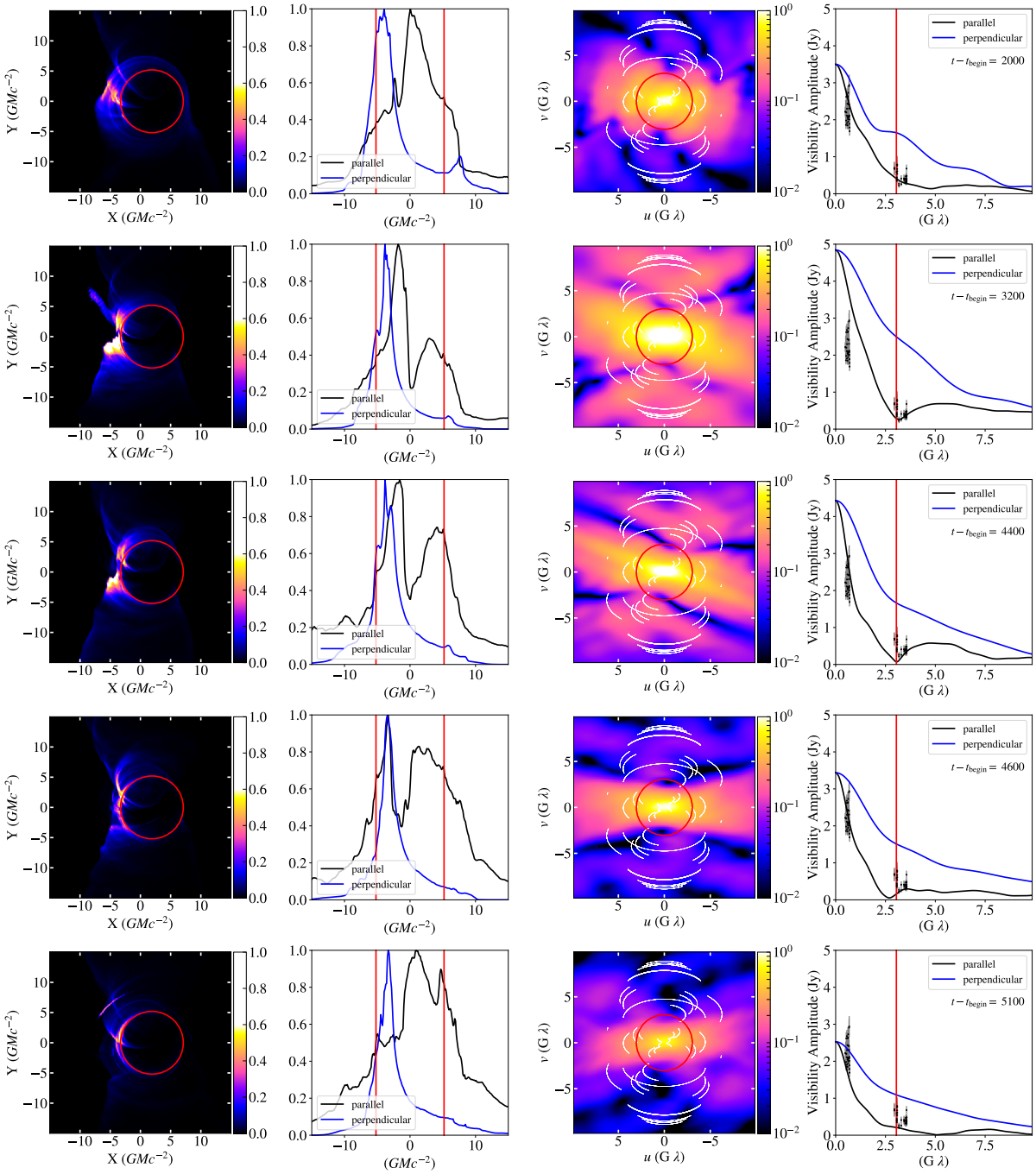

Figure 3.4 Example snapshots from Model B. From left to right: the simulated image for each snapshot, the projections of the simulated image in directions parallel and perpendicular to the black hole spins axis, the visibility amplitude for this snapshot, and the cross sections for the visibility amplitude of this snapshot.

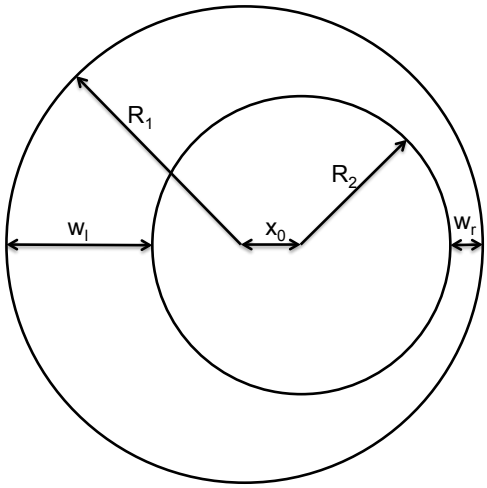

Figure 3.5 An analytic representation of an asymmetric ring model (following Kamruddin & Dexter 2013) as a difference between two offset disks with different radii.

To understand the behavior described above, we employ a simple analytic model to represent the properties of the emission regions. Since the SANE models (A and B) have their emission dominated by the Doppler boosted disk, it roughly resembles a crescent shape. Following Kamruddin & Dexter (2013), we use a model of an asymmetric ring, defined as the difference between two offset disks with different radii, which becomes a crescent as its asymmetry grows. The diagram in Figure 3.5 shows the parameters used to describe our asymmetric ring model. The Fourier transform of the asymmetric ring is given by

$$V_{\rm cres}(k) = \frac{2\pi I_0 R_1}{k}\left[J_1\left(R_1 k\right) - e^{-2\pi i(\alpha_0 u)} R J_1\left(k R_2\right)\right], \tag{3.2}$$

where $k \equiv 2\pi\sqrt{u^2+v^2}$, J_1 are Bessel functions of the first kind, I_0 is the constant surface brightness of the disks, α_0 is the displacement of the smaller disk from the center of the larger disk in the α direction, and $R = R_2/R_1$. Hereafter, we set $R_1 = 1$ without loss of generality. We also define the widths of the asymmetric ring on the left and right sides

of the image as $w_l \equiv R_1 - R_2 + \alpha_0$ and $w_r \equiv R_1 - R_2 - \alpha_0$.

A cross section of the visibilities parallel to the black hole spin axis is then given by

$$V_{\mathrm{cres},u=0}(v) = \frac{I_0}{v}\left[J_1\left(2\pi v\right) - RJ_1\left(2\pi Rv\right)\right], \tag{3.3}$$

which only depends on R, the ratio of the two radii, and not on α_0, the displacement of the smaller disk. In other words, the visibility amplitude along the directions parallel to the spin axis will be the same regardless of the asymmetry of the ring. For an infinitesimally thin ring, i.e., when $w_l \ll R_1$ and $w_r \ll R_1$, the visibility amplitude along a direction parallel to the spin axis has a minimum at $u \simeq 0.4/R_1$. However, Figure 3.6 shows that changing the width of the ring, $w_l = w_r = R_1 - R_2$, changes the location of the minima. In the SANE simulations (A and B) the width of the approximately crescent shape is highly variable because of different turbulent structures appearing and disappearing from the Doppler boosted side of the crescent. This is why the locations of the minima are also highly variable.

The cross section of the visibility function perpendicular to the spin axis of the black hole ($v = 0$) is equal to

$$V_{\mathrm{cres},v=0}(u) = \frac{I_0}{u}\left[J_1\left(2\pi u\right) - e^{-2\pi i\alpha_0 u}RJ_1\left(2\pi Ru\right)\right]. \tag{3.4}$$

Although the visibility amplitude of a cross section parallel to the spin axis did not depend on the displacement α_0, which measures the asymmetry of the ring, the perpendicular cross section does. Figure 3.7 shows the dependence of the visibility amplitude on the degree of asymmetry of the ring w_r/w_l. As the ring becomes more asymmetric, i.e., as $w_r/w_l \to 0$, the visibility amplitude of the cross section perpendicular to the spin

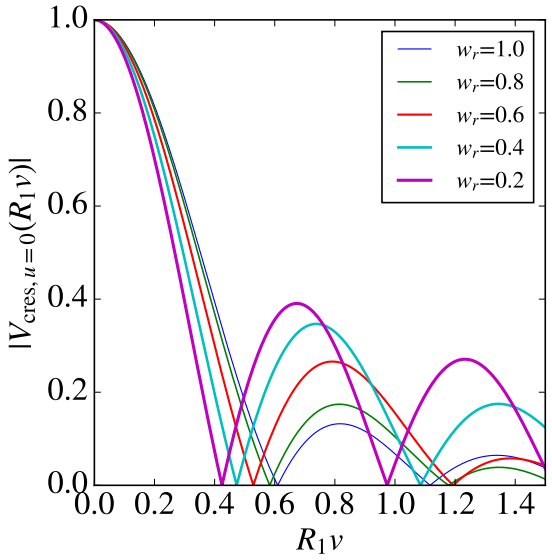

Figure 3.6 The cross section of the visibility amplitude which is parallel to the spin axis for the analytic asymmetric ring model for different widths of the ring. Since the parallel cross section does not depend on the asymmetry of the ring, we have set $w_l = w_r$. A characteristic null appears in the visibility amplitude at $v \approx 0.5/R_1$, with its precise location depending on the width of the ring.

axis becomes smoother and all traces of minima are lost. Due to the effects of Doppler beaming, our simulations are completely dominated by one side of the ring. This is why the cross sections of the visibilities perpendicular to the spin axis (e.g., the blue curves in Figures 3.2 and 3.3) are broad and monotonically decreasing, while the parallel cross sections have strong local minima.

The model described above cannot fully encompass all of the variable structure that we see in Figure 3.4. In the GRMHD simulations, the emission is not always a simple crescent. In some snapshots, the emission along the equatorial plane gets blocked by the colder disk which causes the emission to have two disjointed regions. When this occurs, the visibility amplitudes have short-lived features similar to those of the MAD models,

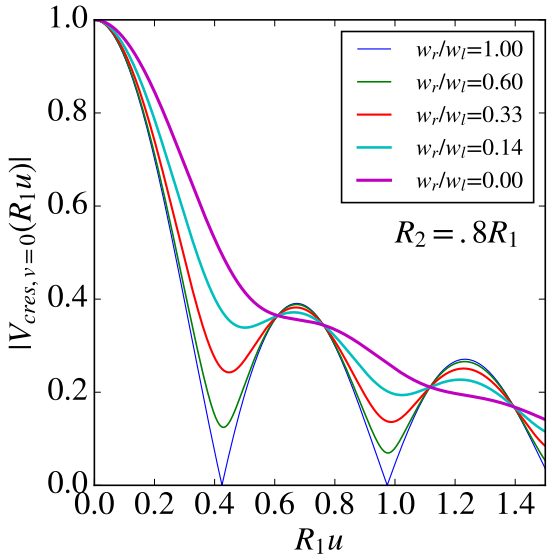

Figure 3.7 The cross section of the visibility amplitude in the direction perpendicular to the spin axis for the asymmetric ring model, for different degrees of asymmetry in the ring brightness. As the ring becomes more asymmetric, the local minimum at $u \approx 0.5/R_1$ becomes less pronounced.

which have two disjointed peaks of emission and will be discussed below.

In summary, for most instances, the behavior of the SANE models (A and B) can be roughly modeled by an asymmetric ring of variable width. The behavior of the cross section of the visibility amplitude that is parallel to the spin axis does not depend on the asymmetry of the ring and exhibits minima. The location of these minima depends on the width of the asymmetric ring, which is variable. Because of this variability, taking the average of the visibility amplitude over time will result in a visibility amplitude with reduced or no minima. The direction perpendicular to the spin axis, however, does depend on α_0. An extremely offset ring, where the thinnest part has a thickness of zero, has a monotonically decreasing visibility amplitude.

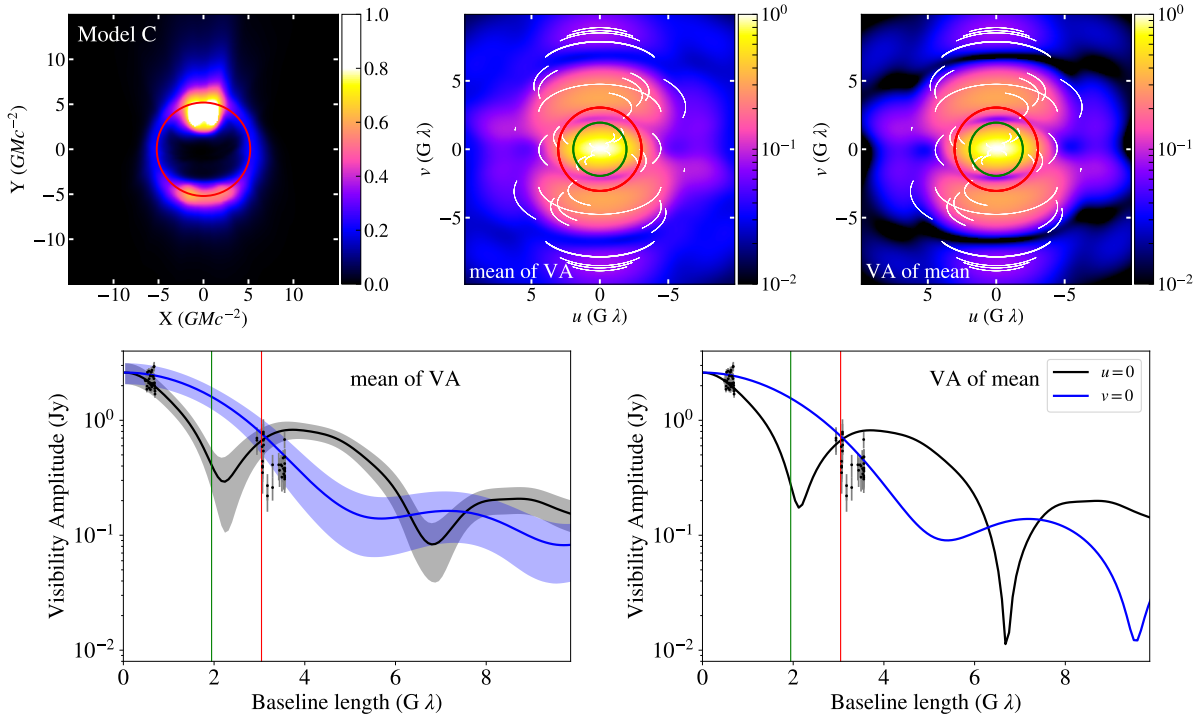

Figure 3.8 Same as Figure 3.2, but for the images from Model C and with the addition of green circles in the top middle and right panels and green lines in the bottom panels. The location of these corresponds to the location of the first minimum in the visibility amplitude of two Gaussians separated by a distance equal to the size of the black hole shadow. These minima occur at small baseline lengths compared to the minima of the asymmetric ring shown in red.

3.1.2 MAD Models

The 1.3 mm emission of the MAD models (C, D, and E) is dominated by the funnels and jet footprints; because of this, it is characterized broadly by two peaks. Throughout the simulations, the relative widths and amplitudes of the peaks change but the distance between them remains approximately constant since it is set by the size of the black hole shadow.

Figures 3.8 and 3.9 are the equivalent of Figure 3.2 but for Models C and D, respectively. Focusing on the one-dimensional cross sections of the visibility amplitude of the

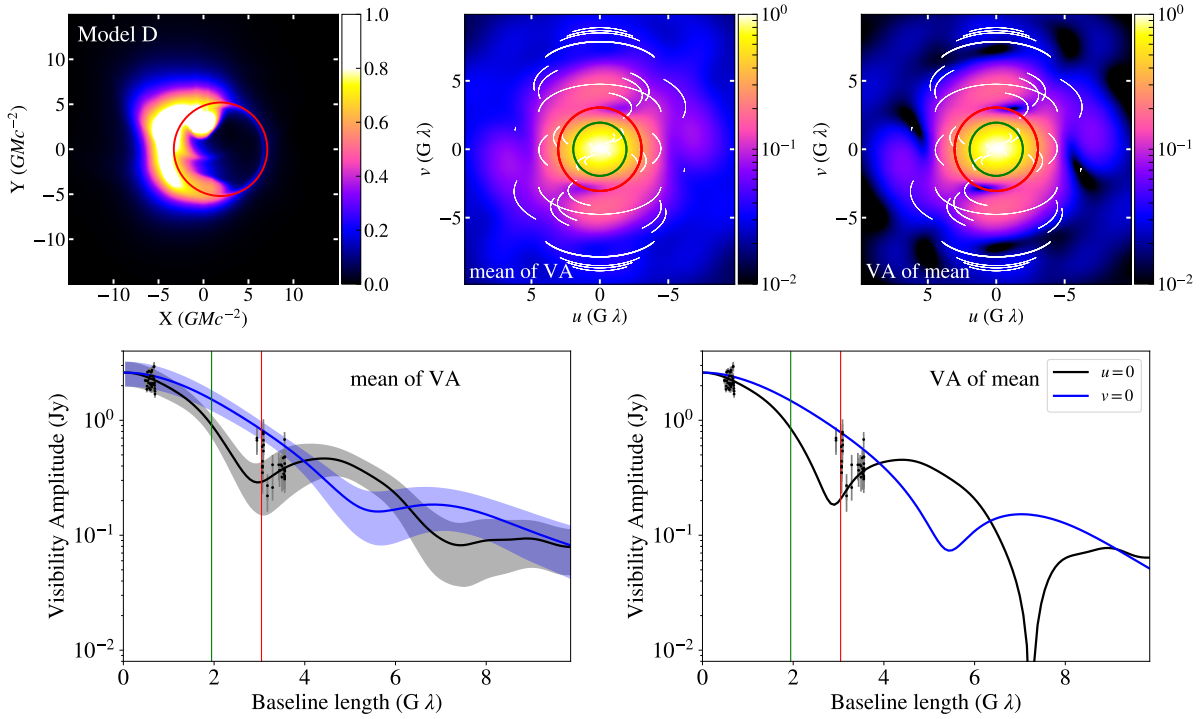

Figure 3.9 Same as Figure 3.8, but for Model D.

mean and the mean of the visibility amplitudes, the cross sections perpendicular to the spin axis have less pronounced minima, which are located at baselines much larger than expected for the size of Sgr A*. The cross sections parallel to the spin axis show much more pronounced minima, close to the expected location for the size of Sgr A*, much like the SANE models. Unlike the SANE models, however, the means of the visibility amplitudes and the visibility amplitudes of the means have very similar structures and both have a minimum in the vertical direction. Furthermore, the minima appear to be in the same locations and the ranges of amplitudes at a given baseline are much smaller than those of the SANE models. This indicates that the existence and location of a visibility minimum is more persistent in MAD models than in SANE models.

To understand the behavior of the MAD models, we employ an approximate model of their emission using two Gaussians separated by a distance d in the direction parallel to the spin axis but with no separation in the direction perpendicular to the spin axis. We define this model as (see Figure 3.10)

$$\begin{aligned} I(\alpha) = \quad & A_1 e^{-\left[(\alpha-\alpha_{01})^2/2\sigma_{\alpha 1}^2 + (\beta-\beta_{01})^2/2\sigma_{\beta 1}^2\right]} \\ & + A_2 e^{-\left[(\alpha-\alpha_{02})^2/2\sigma_{\alpha 2}^2 + (\beta-\beta_{02})^2/2\sigma_{\beta 2}^2\right]}. \end{aligned} \tag{3.5}$$

To simplify our notation, we set $\alpha_{01} = \beta_{01} = 0$ such that one Gaussian is peaked at the origin; set $\alpha_{02} = 0$ so that the Gaussians are separated by a distance $d = \beta_{02}$ along the β axis, and define the ratio of amplitudes $A \equiv A_2/A_1$. This reduces to an overall normalization of A_1, which we ignore to get

$$I(\alpha) = e^{-\left[\alpha^2/2\sigma_{\alpha 1}^2 + \beta^2/2\sigma_{\beta 1}^2\right]} + A e^{-\left[\alpha^2/2\sigma_{\alpha 2}^2 + (\beta-d)^2/2\sigma_{\beta 2}^2\right]}. \tag{3.6}$$

We further define the quantities

$$\begin{aligned} \alpha' \quad & \equiv \frac{\alpha}{\sigma_{\alpha 1}}, \quad \sigma'_\alpha \equiv \frac{\sigma_{\alpha 2}}{\sigma_{\alpha 1}}, \quad \beta' \equiv \frac{\beta}{\sigma_{\beta 1}}, \\ \sigma'_\beta \quad & \equiv \frac{\sigma_{\beta 2}}{\sigma_{\beta 1}}, \quad d' \equiv \frac{d}{\sigma_{\beta 1}}, \end{aligned} \tag{3.7}$$

which in turn gives

$$\begin{aligned} I(\alpha) \quad & = e^{-\left(\alpha'^2+\beta'^2\right)/2} + A e^{-\left(\alpha'^2/\sigma'_\alpha + (\beta'-d')^2/\sigma'^2_\beta\right)/2} \\ & = e^{-\left(\alpha^2+\beta^2\right)/2} + A e^{-\left(\alpha^2/\sigma_\alpha + (\beta-d)^2/\sigma_\beta^2\right)/2}. \end{aligned} \tag{3.8}$$

In this last expression, we omitted the primes for clarity. We now take the Fourier transform of the intensity to obtain

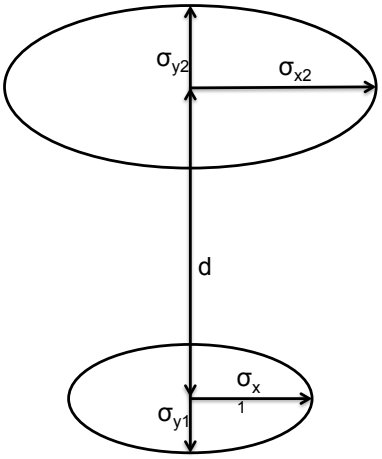

Figure 3.10 An analytic representation of a two spot model in terms of two Gaussian components separated by a distance d along the vertical direction.

$$V_{2g}(k) = \quad 2\pi e^{-\left(u^2+v^2\right)2\pi^2} + 2\pi A\sigma_\alpha\sigma_\beta e^{-\left(u^2\sigma_\alpha^2+v^2\sigma_\beta^2\right)2\pi^2} e^{-2\pi idv}. \tag{3.9}$$

The visibility along a direction parallel to the spin axis takes the form

$$V_{2g,u=0}(v) = 2\pi e^{-2(\pi v)^2} + 2\pi A\sigma_\alpha\sigma_\beta e^{-2(\pi\sigma_\beta v)^2} e^{-2\pi idv}. \tag{3.10}$$

Its magnitude, $|V_{2g}(v)|$, has a minimum when $V_{2g}(v)$ is minimum, i.e., when the second term is real and negative. This occurs when

$$vd = (2n+1)/2, \tag{3.11}$$

i.e., the location of the minimum depends only on the separation between the two Gaussians and not on any of their other properties. Note that, in this configuration, the location of the minimum occurs at a baseline length that is different compared to the case of an asymmetric ring model (see Figures 3.8 and 3.9). This minimum will reach

zero when the amplitudes of the two terms in the sum are equal, or when

$$A = \frac{1}{\sigma_\alpha \sigma_\beta} e^{-\pi^2(1-\sigma_\beta^2)(2n+1)^2/2d^2}. \tag{3.12}$$

The simplified analytic model shows that two Gaussians do not always produce a null in the visibility amplitude. For a given separation d and width ratios σ_α and σ_β, there is only one value of the ratio of the brightness of the two Gaussians, A, that gives rise to a null. When a local minimum does not reach zero, the properties of the two components of the image affect the depth of the minimum. This is shown in Figure 3.11 for the dependence of the depth of the minimum on the ratio A of the brightness of the two components of the image and, in Figure 3.12, for the dependence of the ratio of widths of the two components along the spin axis of the black hole. In our MAD simulations, the relative amplitudes and widths of the two peaks is highly variable; however, the distance between the two peaks remains approximately constant and is set by the size of the black hole shadow and the observer inclination. Because of this, the depth of the minimum varies but the location is approximately constant. When we average minima of various depths but constant location, we get a minimum in the same location of an average depth.

The cross sections of the visibility amplitude maps perpendicular to the spin axis do not exhibit nulls. Analytically, the perpendicular cross sections of the visibility amplitudes of two Gaussians separated in the vertical direction is given by

$$V_{2\mathrm{g},v=0}(u) = 2\pi e^{-2(\pi u)^2} + 2\pi A \sigma_\alpha \sigma_\beta e^{-2(\pi \sigma_\alpha u)^2}, \tag{3.13}$$

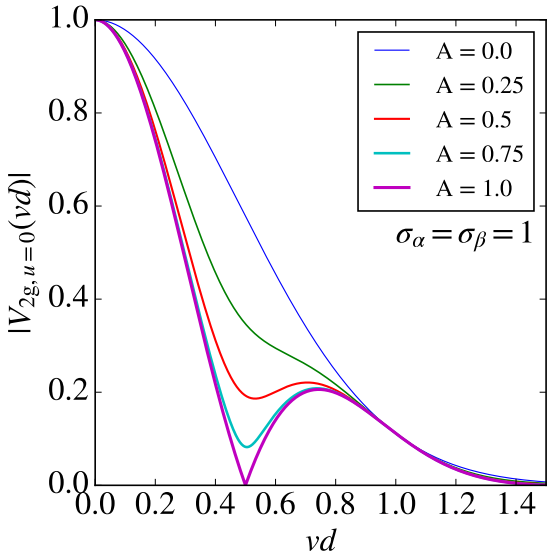

Figure 3.11 The cross section of the visibility amplitude in the direction parallel to the spin axis, for the analytic two-component model for different relative brightnesses of the components, A. We have also set the displacement to $d = 3$ and the relative widths to $\sigma_\alpha = \sigma_\beta = 1$. The baseline dependence of the visibility amplitude shows a characteristic minimum at a location that depends only on the distance between the two components of the image. The minimum becomes deeper as the relative brightness of the two components becomes equal to unity.

which is just the addition of two Gaussians both peaked at the origin, and therefore has no nulls.

In our simulations, the visibility amplitudes of the MAD models have a consistent minimum in the direction parallel to the spin axis of the black hole. The location of the minimum is approximately constant and is determined primarily by the size of the black hole shadow. Averaging over time does not appear to erase the minimum as it did in the SANE models.

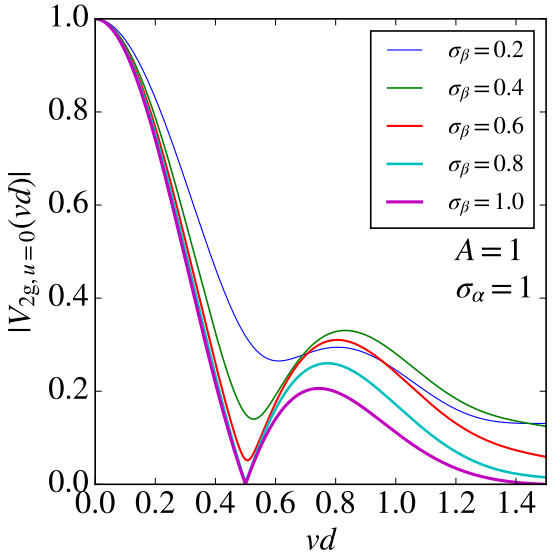

Figure 3.12 The cross section of the visibility amplitude in the direction parallel to the spin axis, for the analytic two-component model for different widths of the components, σ_β. We have also set the displacement to $d = 3$, the relative widths in the α direction to $\sigma_\alpha = 1$, and the relative brightnesses to $A = 1$. As in Figure 3.11, the visibility amplitudes show a characteristic minimum around $v = 0.5/d$. The minimum becomes deeper as the relative width of the two components of the image becomes one.

3.2 Conclusions

In this chapter, we quantified the effect of MHD turbulence driven variability on the structure of visibility amplitudes of the upcoming imaging observations of Sgr A* with the EHT. We explored the effect of variability on the structure of the emission region in order to understand the challenges that variability will pose for image reconstruction of EHT observations. We created and analyzed mock images and $u-v$ maps using GRMHD simulations, that were constrained in previous work such that their time averaged broad-band spectrum and 1.3 mm image size match observations of Sgr A*.

We found that the visibility amplitude of the SANE models resembles that of a

highly asymmetric ring. The width of the asymmetric ring is highly variable due to the turbulent accretion flow. The visibility amplitude in the direction parallel to the spin axis of the black hole typically exhibits minima with locations that depend on the width of the asymmetric ring. Since the location of the minima in the direction parallel to the spin axis depends on the width of the emitting region, and is therefore variable, any information that could be inferred by the presence of a minimum is lost by averaging over time.

The SANE models rarely exhibit minima in the direction perpendicular to the spin axis of the black hole. The reason for this is that, due to Doppler beaming, the majority of emission comes from the left of the spin axis (for the spin orientation we use in our figures), with negligible emission coming from the right. This asymmetry does not affect the visibility amplitude in the direction parallel to the spin axis, but affects the depth of minima in the direction perpendicular to the spin axis. For the perpendicular direction, a highly asymmetric ring has a visibility amplitude that decreases monotonically.

In contrast, the images and visibility amplitudes of the MAD models are characterized by two bright spots at the footpoints of the jets, separated by a relatively constant distance equal to the size of the black hole shadow. For the MAD models, the visibility amplitudes in the direction parallel to the spin axis have persistent nulls in constant locations but with variable depths. The locations of the minima in the direction parallel to the spin axis of MAD models depend strongly on the separation between the two image components. Since the distance between the emission peaks in our simulations are

set primarily by the size of the black hole shadow and are approximately constant, the location of the minimum is constant. However, varying the widths, or amplitudes, of the image components affects the depths of the minima. On the other hand, the visibility amplitudes in the direction perpendicular to the spin axis have much less pronounced minima at larger baselines.

Typical EHT exposure times are around 10 minutes and typical imaging runs span a few hours. Our 60-hour simulations are longer than a typical observing run but shorter than the timespan between different observing epochs. Indeed, the EHT is expected to observe Sgr A* for a few nights in each observing cycle, with multiple cycles to occur in successive years. Therefore, the EHT data set as a whole will span multiple years and will sample a broad range of the variability of the source. If the longest timescale of significant source variability is of the order of a few hours to a day, then the range of variability that our models exhibit will be representative of the expected range of variability in the data, when multiple epochs are combined.

A second important issue that we can address with our simulations is the effect of the length of each imaging run on the degree of expected variability. To achieve this, we divided each one of our simulations into overlapping segments of constant length and calculated the fractional rms variability for each segment of the visibility amplitude at three locations in the $u - v$ plane that correspond to the Arizona-California-Hawaii baselines. We then use the measured values of rms variability and calculate their average and standard deviation. In all cases, we calculate the fractional variability by dividing the

standard deviation with the mean visibility amplitude of the entire 60 hour simulation. Finally, we explored the effect on the fractional rms variability of using different exposure (i.e., averaging) times for each measurement of a visibility amplitude.

In Figure 3.13, we show the dependence of these fractional rms variability amplitudes on the length of the segments. For displaying the mean of the rms variability, we use dashed and solid lines to show the effect of changing the exposure time from the 3.5 minute cadence of our simulation outputs to a 10.5 minute time that is representative of early EHT observations. Changing the effective exposure time has a very little impact on the rms variability. On the other hand, as the length of each segment increases, both the number of different overlapping segments decreases and the amount of overlap between successive segments increases, as well. Because of this, the range of fractional rms variability decreases as the length of each segment increases.

In all five models, the fractional rms amplitude increases rapidly with the length of the segment over which the variability is calculated, for lengths shorter than a few hours. Beyond that, increasing the length of the segment does not contribute significantly to the variability. This is expected because, as we discussed in Chan et al. (2015b), the power spectrum of the 1.3 mm variability exhibited by our simulations is that of red noise and turns over at timescales longer than a few hours. This is also consistent with the reported turnover timescale for the observed power spectrum of Sgr A* at 1.3 mm (Dexter et al., 2014). Our results suggest that observing runs that are a few hours long will be affected by the full range of variability that our simulations exhibit.

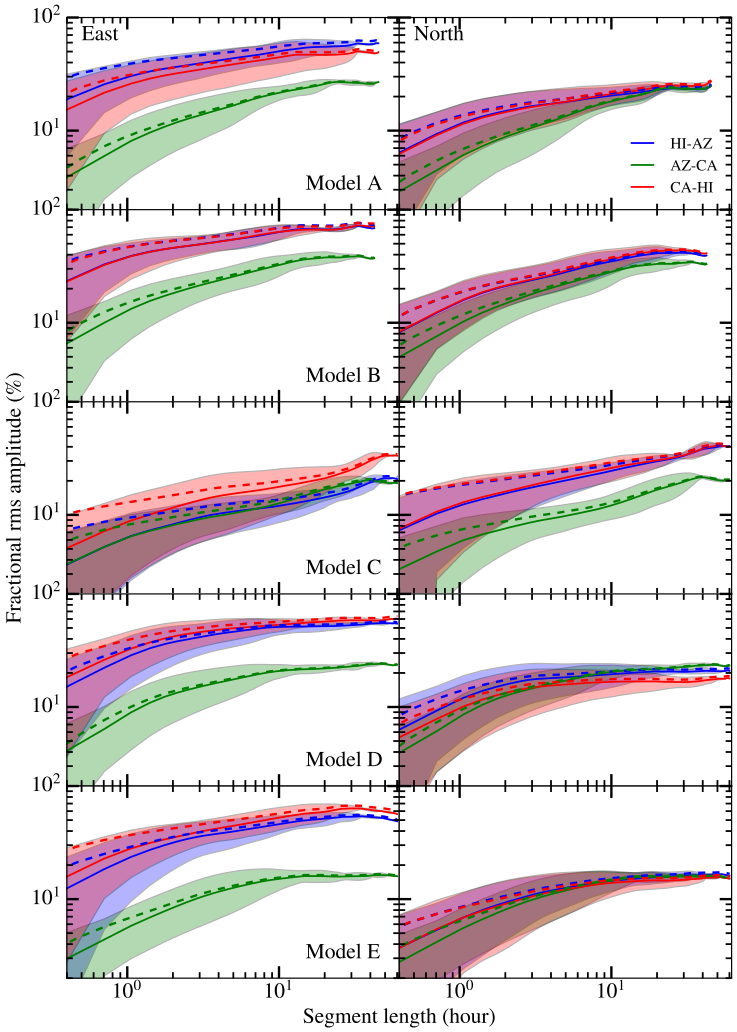

Figure 3.13 Fractional root-mean-squared (rms) variability as a function of the time length of simulation segments. The right (left) column assumes that the black hole spin axis points North (East). The dashed line in each panel is the mean fractional standard deviation of the original simulation with a time resolution of about 3.5 minutes and an effectively instantaneous exposure. The solid line is the mean fractional standard deviation calculated using an effective exposure (averaging) time of 10.5 minutes. The colored regions correspond to the standard deviation in the fractional rms variability for different overlapping segments in the simulation. The three colors in the plot correspond to the three baselines used by Doeleman et al. (2008) and Fish et al. (2011) to take the data shown in Figures 3.2, 3.3, 3.4, 3.8, and 3.9. Red corresponds to the baseline formed by CARMA (California) and the SubMillimeter Telescope (SMT, Arizona), green corresponds to the baseline formed by CARMA (California) and the SubMillimeter array (SMA, Hawaii), and blue corresponds to SMT (Arizona) and SMA (Hawaii). Segments that are at least a few hours long exhibit the full range of variability that our simulations show.

The variability in the interferometric visibilities may, in principle, affect both the parameter estimations based on comparing theoretical models to data and the images that will be reconstructed from the observations. In a companion paper Kim et al. (2016), we develop a Bayesian method to perform parameter estimation using explicitly the time dependence of GRMHD simulations and the expected variability of the upcoming EHT observables. Even without employing such a method, our results nevertheless suggest that fitting early EHT data using simple models of the accretion flow that do not take into account its intrinsic variability will lead to a reasonably accurate determination of the orientation of the black-hole spin on the plane of the sky that will depend only weakly on the flow properties (see, e.g., Broderick et al. 2011b; Psaltis et al. 2015a). This is true because, in both the disk-dominated SANE models and the jet-dominated MAD models, the visibility amplitudes perpendicular to the spin axes are smoother and vary over longer baselines while the visibilities along the spin axes have significantly more structure and drop faster with baseline length.

Using, on the other hand, simple time-independent models to measure more detailed properties of the black hole, such as the size of its shadow and the magnitude of its spin will be likely hampered by the variability in the flow because such models do not generally allow the image structure to change. For example, the spin of the black hole affects primarily the widths of the crescent-like shapes of disk-dominated images and, hence, the locations and depths of minima in the visibility amplitudes. However, turbulence in the accretion flow causes both the locations and depths of these minima to be highly

variable, effectively masking the effect of black-hole spin on the image. In order for the EHT observations to lead to accurate determination of the black-hole shadow size and spin, the image reconstruction and model fitting algorithms will need to take into account the variability of the underlying images explicitly.

Chapter 4

Variability in GRMHD Simulations of Sgr A*: Implications for EHT Closure Phase Observations

The EHT will in principle measure visibility amplitudes and phases, which are the complex components of the Fourier transform of the image. However, mm wavelength VLBI interferometers cannot measure absolute phases at each $u-v$ point covered by the array. This is because there are no point sources that are both close enough to Sgr A* and bright enough at 1.3 mm to be used for calibration and because the timescale for variability of the atmospheric interference at 1.3 mm due to water vapor is only of the order of 10 s (Doeleman et al., 2002). Instead, the EHT will measure closure phases, which are the sum of phases at three points in $u-v$ space, such that the effect of the atmosphere

at each telescope cancels out (Jennison, 1958). The EHT has already obtained closure phase data for Sgr A* for the Hawaii, Arizona, California (HI-AZ-CA) triangle. Fish et al. (2016) reported a median closure phase of $+6.3^\circ$ over 13 observing nights during a four year period. The positive, non-zero average closure phase demonstrates that Sgr A* is not circularly symmetric on event-horizon scales.

A number of groups have considered the effects of closure phase variability in interpreting EHT data. Doeleman et al. (2009b) used a semi-analytic model to explore the variability in closure phases caused by an orbiting hot spot for a few EHT closure triangles. Dexter et al. (2010) performed an early study of the properties of closure phase variability in GRMHD simulations focusing on disk dominated models and triangles which are appropriate for the already existing EHT observations. Broderick et al. (2011a) compared stationary semi-analytic models with variable normalization to early EHT closure phase data. Broderick et al. (2016) studied closure phases for the HI-AZ-CA triangle in a stationary semi-analytic accretion flow model, when small scale Gaussian brightness fluctuations were introduced. Fraga-Encinas et al. (2016) used two GRMHD models, one funnel dominated and one disk dominated, to explore the effect of the Earth's rotation on the variability of closure phases in the HI-AZ-CA triangle but did not include the effect of intrinsic source variability.

In this chapter, we aim to characterize the expected properties of closure phases for Sgr A* in a wide range of EHT triangles of various sizes and orientations, using the suite of simulations discussed in Chapter 2. In §4.1, we investigate the expected magnitudes

and variability of the interferometric visibility phases throughout the $u-v$ plane. Even though the Event Horizon Telescope will not be able to measure directly the visibility phases at individual locations on the $u-v$ plane, exploring their properties allows us to understand in §4.2 the variability of the closure phases that the Event Horizon Telescope will measure. We conclude in §4.3 and compare our results to the existing limited number of closure phase measurements from Sgr A* on a single baseline triangle (Fish et al., 2016).

4.1 Visibility Phases

Since the EHT is an interferometer, it will observe the visibilities, or the complex Fourier components, of the image of Sgr A*. The amplitudes of these Fourier components, or visibility amplitudes, for our five models have been discussed in Chapter 3. Here we focus on the phases of the complex Fourier components, or visibility phases.

Due to the effects of gravitational lensing and Doppler beaming, the emission predicted by these models is not centered on the black hole (the red stars and red dots in Figure 2.3 are in different locations), which results in an overall rapid gradient in phase. We removed this unmeasurable phase gradient by shifting the snapshots such that the center of light of the images (the red stars in Figure 2.3) coincide with the center of the average image (red dots in Figure 2.3) before calculating the transforms. We performed the same shift for all snapshots within each simulation such that they all have the same phase centers.

In Figure 4.1, we present the structure of the complex visibilities for the different

GRMHD models denoting the average visibility phases with contours and the visibility amplitudes in color maps. These averages are obtained by finding the phases and amplitudes of each snapshot and subsequently averaging them. Because angles are directional, periodic quantities, we need to employ a method for calculating means that is appropriate for them. In the Appendix, we describe the directional statistic we use hereafter.

Figure 4.1 highlights the fact that minima in visibility amplitudes coincide with steep gradients in phase. This is particularly prominent in the MAD models (C, D, and E), which have clear minima that are preserved in the average of the visibility amplitudes as we showed in our previous paper Medeiros et al. (2018a). In each panel, the black dashed (solid) triangle corresponds to the HI-AZ-CA closure triangle for a black hole with spin axis pointing North (East). For brevity, we plotted the visibility amplitude and phase averages of the black hole at a constant (North) orientation but moved the triangle so that the relative orientation of the visibilities and the triangles is correct for the quoted black hole spin axis orientation. In reality, the orientation of the triangle is fixed and the orientation of the black hole in the sky is unknown. We will discuss these triangles further below.

We explore the structure of the variability in the visibility phases in Figure 4.2, where the dispersion in visibility phases is shown in color, while the average visibility phases are shown as white contours for comparison. The dispersion was calculated by taking into account the fact that angles are directional quantities, as discussed in the Appendix.

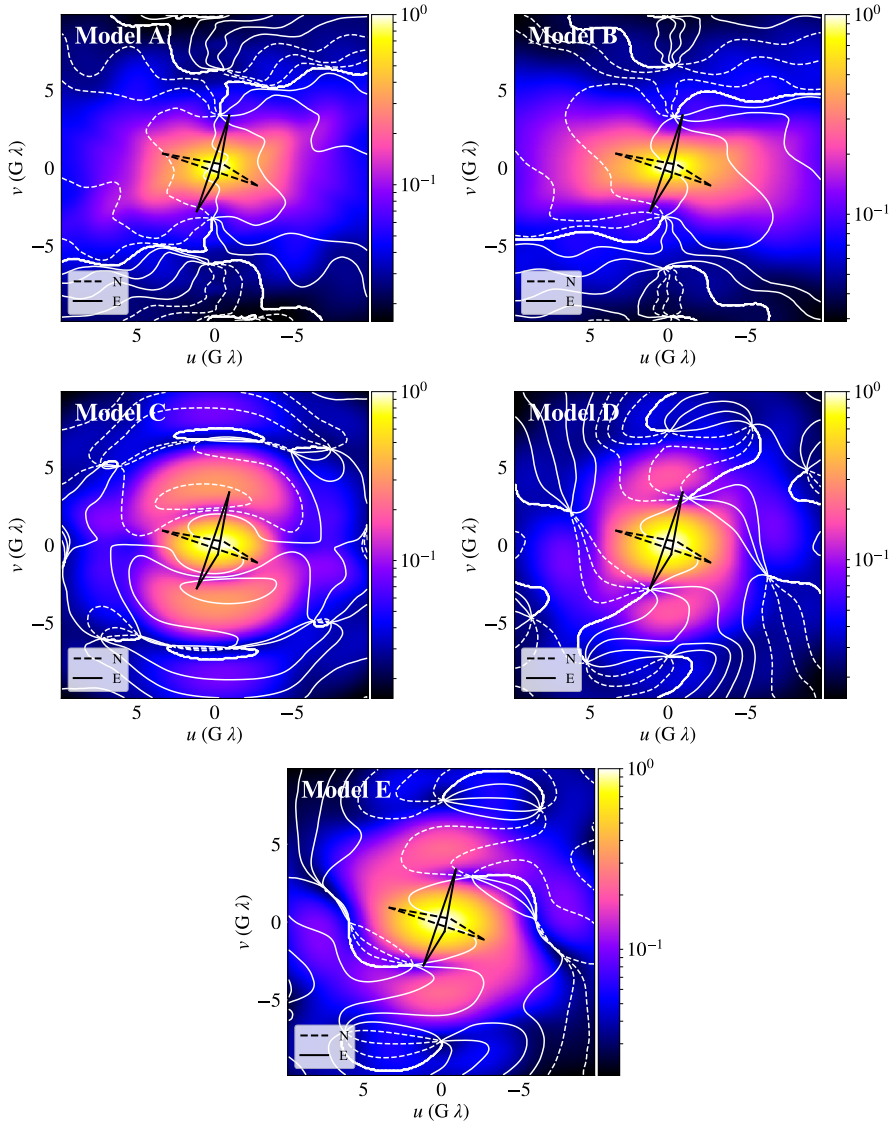

Figure 4.1 The color maps show the average visibility amplitudes and the white contours the average visibility phases for the five models. Minima in the visibility amplitudes correspond to steep gradients in visibility phases. The black dashed triangles correspond to the HI-AZ-CA triangle for a black hole with a spin axis pointing North while the solid black triangles correspond to the same HI-AZ-CA triangle for a black hole with spin axis pointing East. The visibility amplitude maps have been normalized to unity.

The directional dispersion, D (see equation A4), is approximately equal to $\sigma^2/2$ for small σ, where σ is the dispersion of a non-directional Gaussian distribution, and approaches

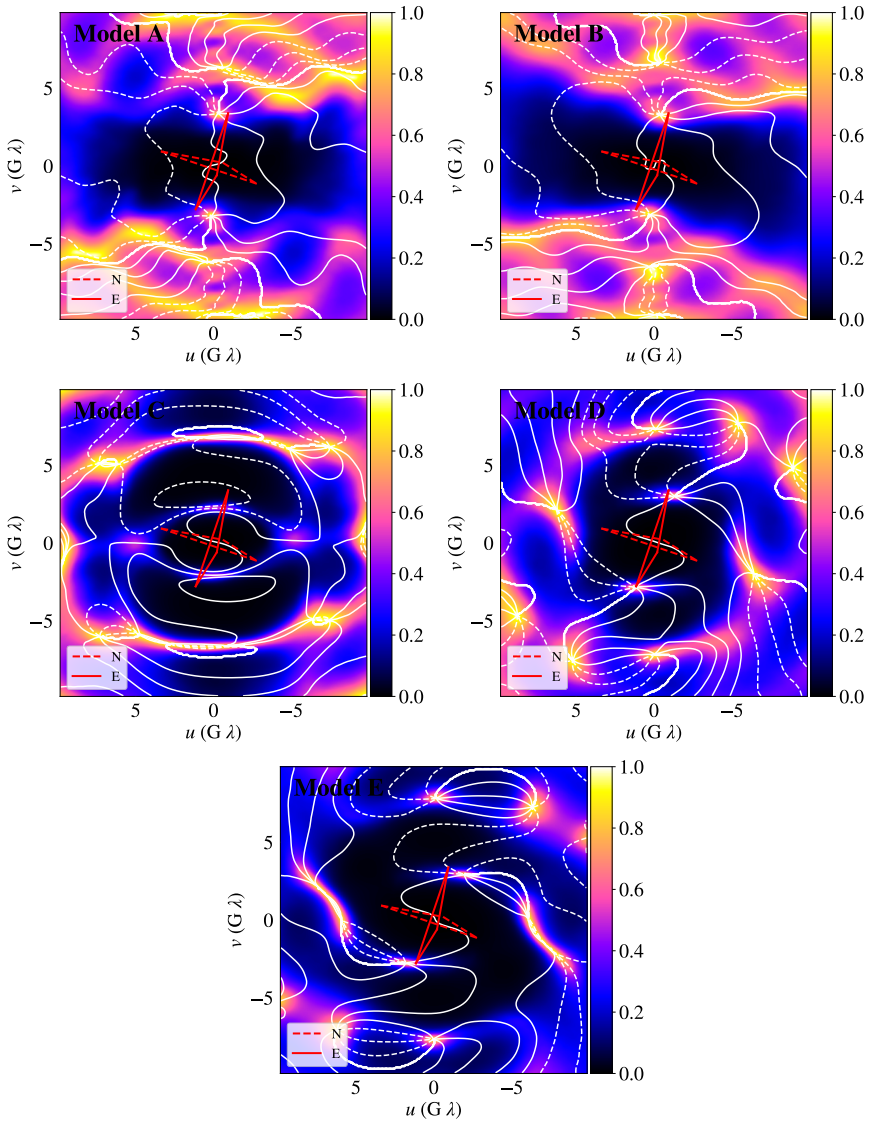

Figure 4.2 The color map shows the dispersion in visibility phase at each point in the $u-v$ space throughout each ~ 60 hour simulation. These dispersions were calculated using the directional statistics described in the Appendix. The white contours correspond to the average phase. Regions of steep phase gradients (and minimum amplitudes; cf. Figure 4.1) correspond to large dispersion in visibility phase. The red dashed (solid) triangle corresponds to the HI-AZ-CA closure triangle for a black hole with spin axis pointing North (East).

unity in the limit of a flat distribution. In the figure, the black and dark blue regions have small dispersions, while the yellow or white regions have very broad, and possibly

flat distributions. For reference, $D = 0.5$ shown in pink corresponds to a Gaussian with a standard deviation of about 1 rad or 57°.

Figure 4.2 shows two general characteristics of variability in the visibility phase throughout the $u - v$ plane. First, for each model, there are a number of localized regions on the $u - v$ plane that exhibit very large dispersions in phase. These regions coincide with the locations of the minima in the visibility amplitudes. Phase variability is related to visibility amplitude since, for similar perturbations in its real and imaginary components, a vector with larger magnitude will experience a smaller change in phase. This means that, if all complex Fourier components of the image experience perturbations to their real and imaginary components of similar size, the complex vectors with smaller amplitude will experience a larger change in phase than those with a larger amplitude. Therefore the regions that have low visibility amplitude also have very high phase variability as a direct consequence of the low amplitude (see also the discussion in Dexter et al. 2010.)

Second, outside the confined locations of the amplitude minima, the variability in the visibility phases at small baseline lengths (less than a few Gλ) is in general very small, even though the accretion flow is highly turbulent. This happens because the small baselines primarily probe the overall structure of the image, which is determined by special and general relativistic effects rather than gas dynamics, and shows little variability. However, at larger baseline lengths, for most baseline orientations, the SANE models A and B show significant phase variability, while the MAD models C-E remain

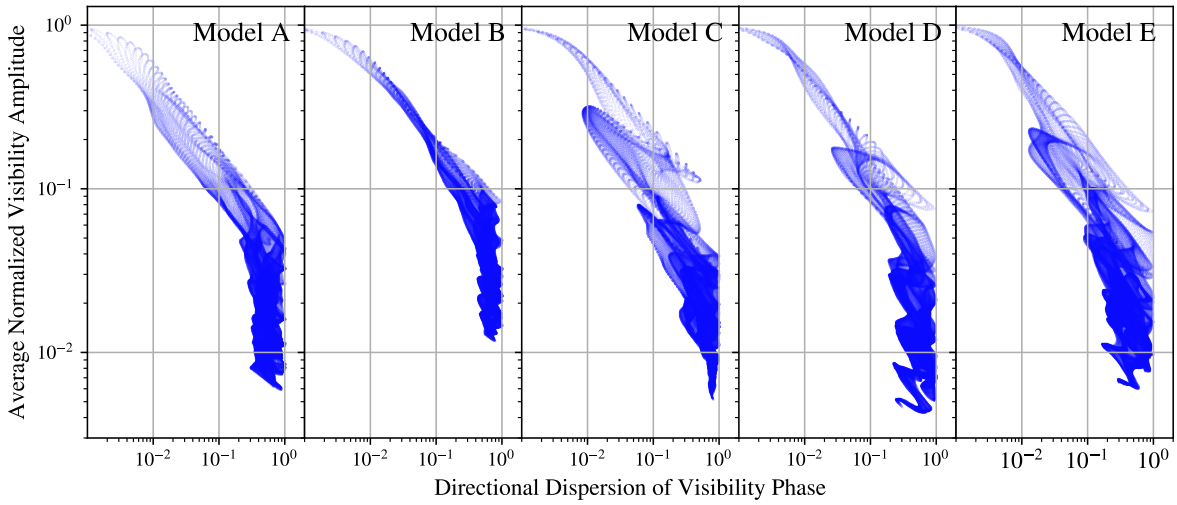

Figure 4.3 Normalized visibility amplitude versus directional dispersion (D) of visibility phase. The different columns correspond to the different models and each dot is a point in $u-v$ space. In all models, the regions of largest dispersion in visibility phase correspond to the lowest visibility amplitudes.

relatively quiet. The large baselines probe the small scale structures, which, in the case of the SANE models, are dominated by, e.g., small hot magnetic flux tubes that are highly variable. In the case of the MAD models, even the small scale structure is dominated by the emission at the funnel footpoints and, for the models we consider here, the closure phases along large baseline triangles are not significantly variable.

In order to demonstrate one of the above points in a different way, we show in Figure 4.3 the overall anticorrelation between the average visibility amplitude throughout the $u-v$ plane and the corresponding dispersion in the visibility phase. Indeed, the largest phase dispersions occur when the visibility amplitude is very low, i.e., at least an order of magnitude smaller than its maximum. As this figure demonstrates, this anticorrelation is independent of the particular cause of variability or the specifics of the models explored.

4.2 Closure Phases

As we discussed in the previous sections, mm VLBI experiments cannot measure absolute phase since the atmosphere introduces an arbitrary phase that is variable on a ≈ 10 s timescale. Instead, the EHT measures closure phases, defined as the sum of the phases at the corners of a triangle in $u-v$ space that corresponds to three telescopes on Earth. Measuring closure phases removes the effects of the atmosphere and instrumental noise from the phase measurements, but cannot recover all absolute phase information, because there are never enough closure triangles to solve for all absolute phases.

Our aim is to explore what the closure phases that the EHT measures will reveal about horizon-scale structures and how they will probe small-scale variability. During the span of an observation, closure triangles move through the $u-v$ space. Therefore, the observed variability in closure phases will reflect the combined effect of the intrinsic variability of the source, the variability caused by the fact that the closure triangles are probing different parts of $u-v$ space as the Earth rotates (see, e.g., Doeleman et al. 2009b; Broderick et al. 2011a, 2016; Fraga-Encinas et al. 2016), and the variability caused by diffractive scattering effects (see Johnson & Gwinn 2015). In the current section, we are primarily interested in exploring the intrinsic variability caused by the accretion flow itself. Because of this, we keep the triangles constant in time for the majority of our analysis (fixed at GMST 01:54:03.4706); we will explore the effect of the Earth's rotation at the end of this section and the effects of scattering in a forthcoming paper.

We choose 4 representative triangles of varying shapes and sizes, shown in Figure 4.4.

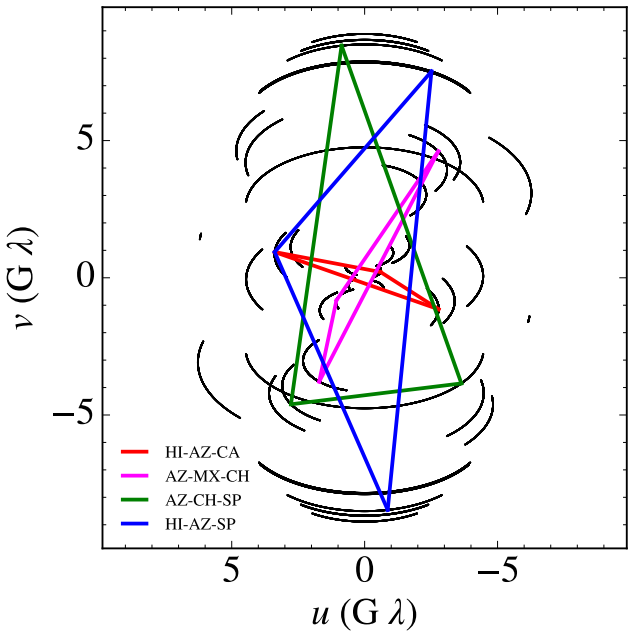

Figure 4.4 The four triangles we used to calculate closure phases (shown here at GMST 01:54:03.4706). In order of increasing size, they are Hawaii (SMA)-Arizona (SMT)-California (CARMA), shown in red, Arizona (SMT)-Mexico (LMT)-Chile (ALMA), shown in magenta, Arizona (SMT)-Chile (ALMA)-South Pole (SPT), shown in green, and Hawaii (SMA)-Arizona (SMT)-South Pole (SPT), shown in blue. The black curves correspond to the EHT baselines for reference. These triangles move through $u-v$ space following the baseline tracks as the Earth rotates.

The smallest triangle, shown in red, is the Hawaii (Submillimeter Array-SMA)-Arizona (Submillimeter Telescope-SMT)-California (Combined Array for Research in Millimeter-wave Astronomy-CARMA) triangle. This is the only triangle on which the EHT has observed closure phases to date. The next smallest triangle, shown in magenta, is the Arizona (SMT)-Mexico (Large Millimeter Telescope-LMT)-Chile (Atacama Large Millimeter/submillimeter Array-ALMA) triangle. The bigger triangles are Arizona (SMT)-Chile (ALMA)-South Pole (South Pole Telescope-SPT), shown in green, and Hawaii (SMA)-Arizona (SMT)-South Pole (SPT), shown in blue.

We calculate closure phases for the four triangles for each snapshot of our five models, for black holes with spin axes pointing North and East. Due to the symmetry of Fourier transforms, the closure phases for black holes with spin axes pointing South (West) are the negative of the closure phase for black holes pointing North (East). We use the same sign convention as described in Fish et al. (2016). Figures 4.5 and 4.6 show closure phases as a function of time for both spin orientations, for the four triangles (ordered from the smaller triangle on the top row to the largest on the bottom row), and for the five models. To explore the distribution of closure phases more quantitatively, we also plot them as histograms in Figure 4.7.

As the top panels for each model in Figures 4.5 and 4.6 and the leftmost panels in Figure 4.7 show, all of our GRMHD models produce little phase variability on small triangles, with the exception of situations where at least one vertex of the triangle crosses an amplitude minimum (see, e.g., the East orientation for models D and E). On larger triangles, the closure phases generally show larger dispersion. For these triangles, however, there is an important difference between the SANE and the MAD models. The MAD models still show peaked distributions of closure phases with well defined means and dispersions, whereas the histograms of the SANE models become nearly flat. Both of these results are expected given our discussion of visibility phase variability in Section 4.1.

The results shown in Figures 4.5, 4.6 and 4.7 are not specific to the particular black-hole spin orientations chosen for these examples but are generically encountered in all

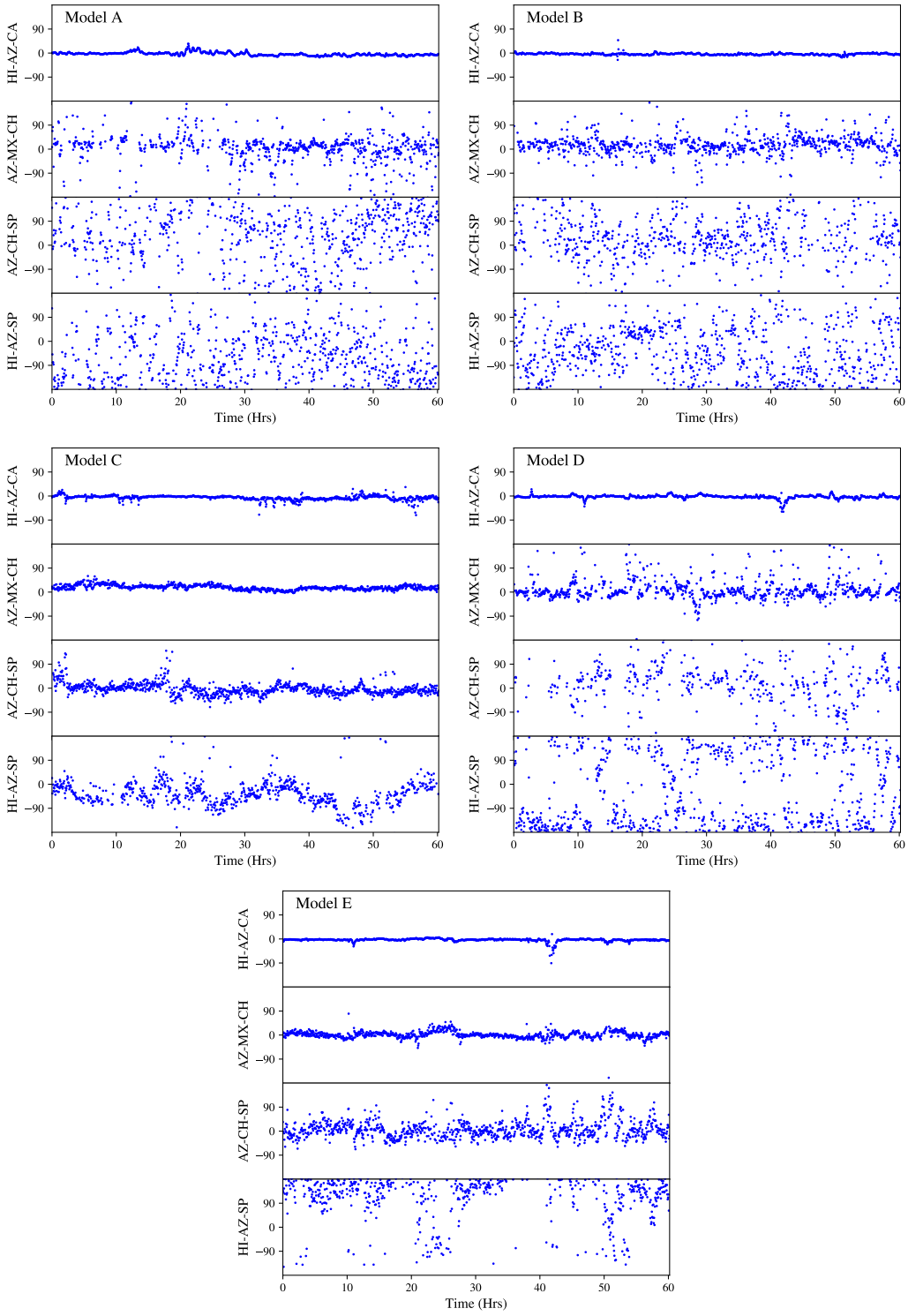

Figure 4.5 Closure phases as a function of time for the five simulations and the four closure triangles we consider for a black hole with a spin axis pointing North. Different rows correspond to different triangles in order of increasing size from top to bottom.

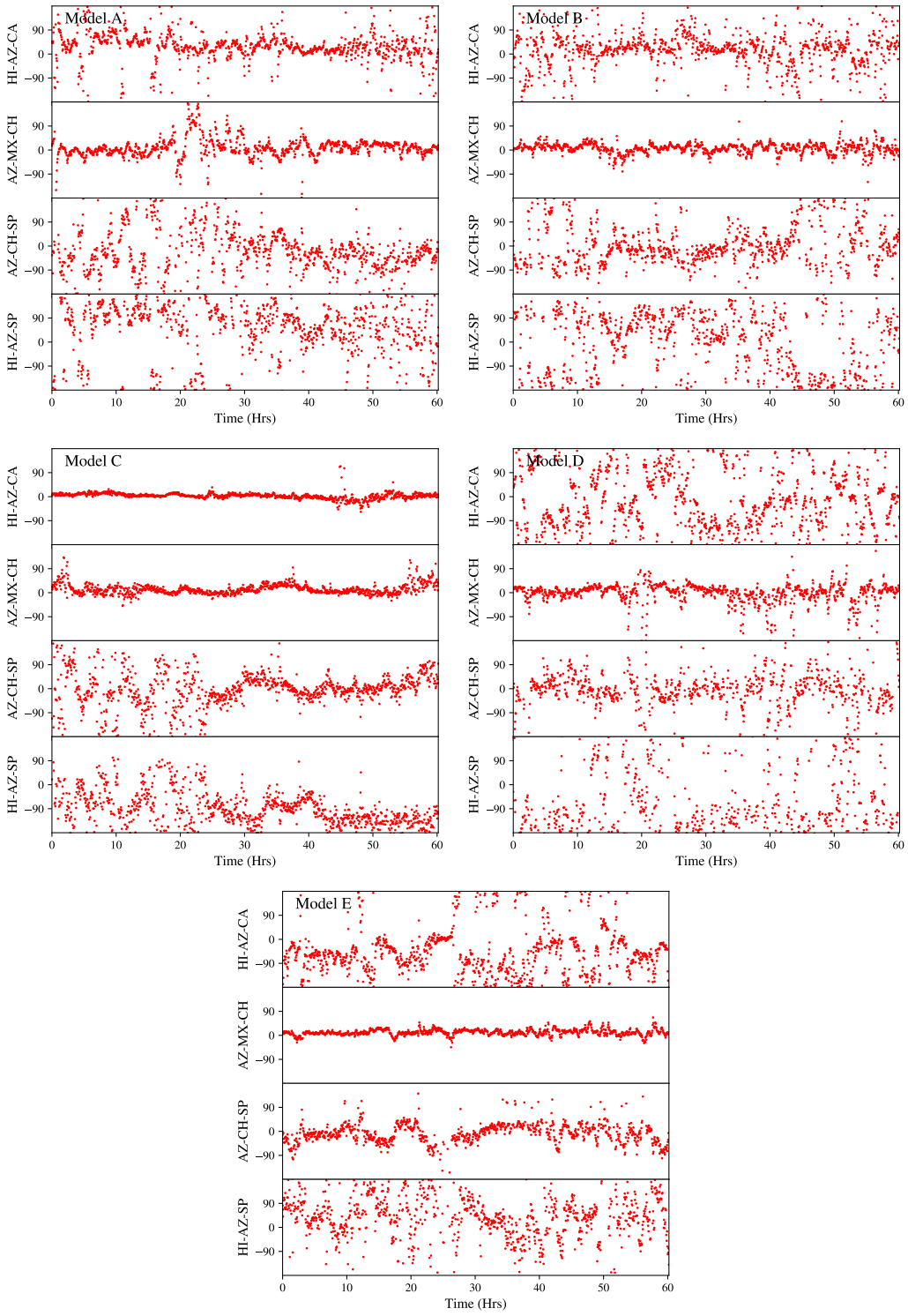

Figure 4.6 Same as Figure 4.5 but for a black hole with spin axis pointing East.

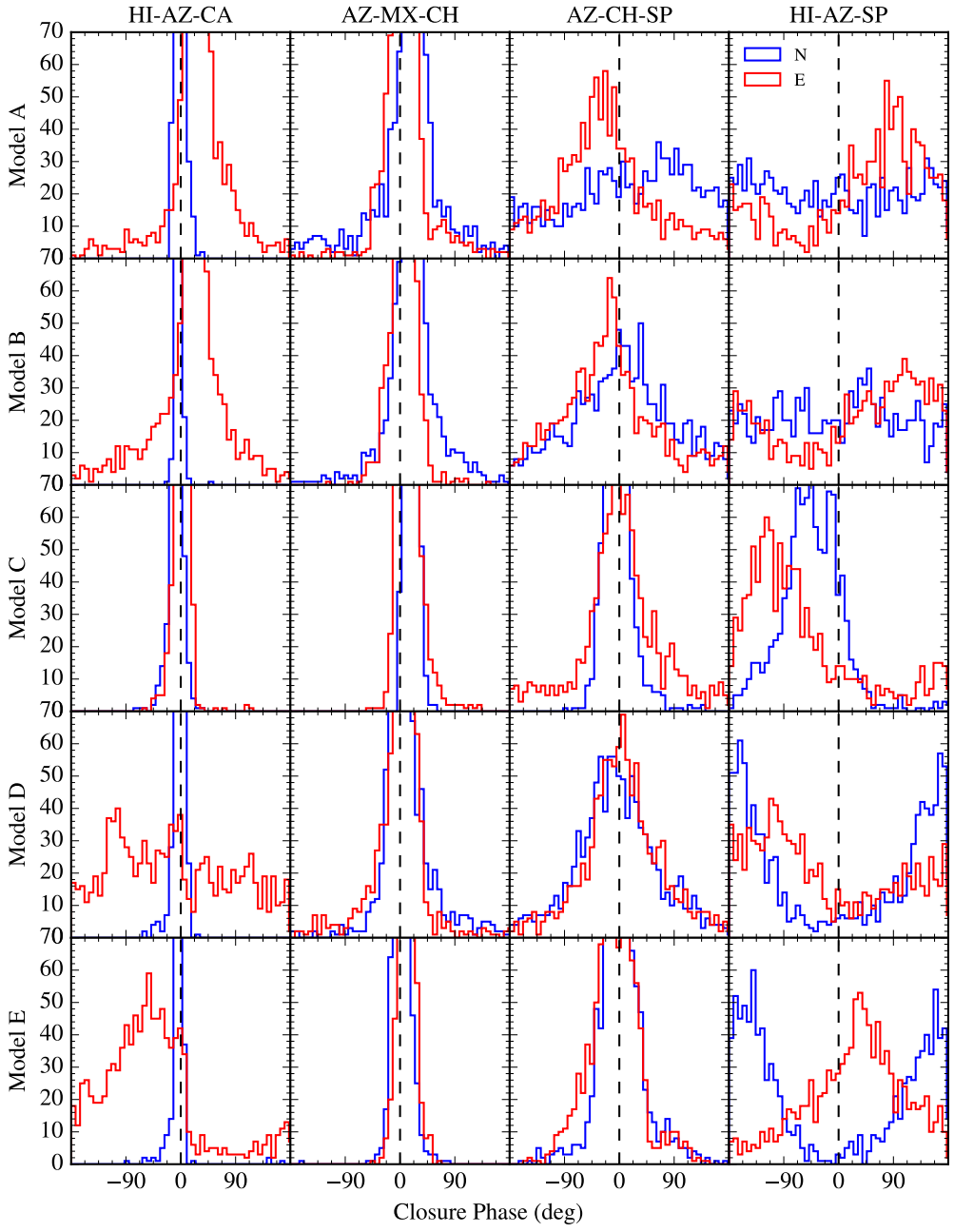

Figure 4.7 Histograms of closure phases calculated for the four triangles we consider. Rows correspond to the different models and columns to different closure triangles, in order of increasing size. In all panels, the blue histograms correspond to a black hole with spin axis that points North, while the red histograms correspond to a spin axis that points East. The orientation of the black hole has a very large effect on the mean and width of the distribution of the closure phases. Some of the peaks of the histograms are not shown in this figure since we are not concerned primarily with the value of the peak but rather with the width of the distribution.

orientations. We demonstrate this in Figure 4.8, which shows the dependence of the closure phase dispersions on black-hole orientation, for the four triangles and for the five models we consider here. In the smallest of the triangles, a small phase dispersion (at the level recently reported by Fish et al. 2016) occurs for about half of the spin-orientation parameter space for all five models. However, for the largest triangles, the large dispersion in the SANE models persists for all spin orientations.

The statistical properties of closure-phase variability that we discussed so far correspond to fixed orientations of the baseline triangles on the $u - v$ plane. In practice, we can observationally infer these properties if we combine data from different epochs and stack them based on the location of each triangle on the $u - v$ plane. However, in the course of a single observation epoch, the orientation of each baseline triangle changes in time and the measured closure phases will sample different locations of the $u - v$ plane, while the underlying image is varying at the same time. A consequence of this may be that a given triangle will rotate from a region of small variability to one of large variability (e.g., near a visibility minimum) or vice versa in the course of a night. In this case, the characteristics of phase variability will change dramatically in the course of the observation.

We show an example of this situation in Figure 4.9 for the small HI-AZ-CA triangle (top panels) and the SANE model A as well as for the larger AZ-MX-CH triangle (bottom panels) and for MAD model E, for two different orientations of the black-hole spin. In two of the configurations shown (Model A, HI-AZ-CA South orientation and Model E AZ-MX-

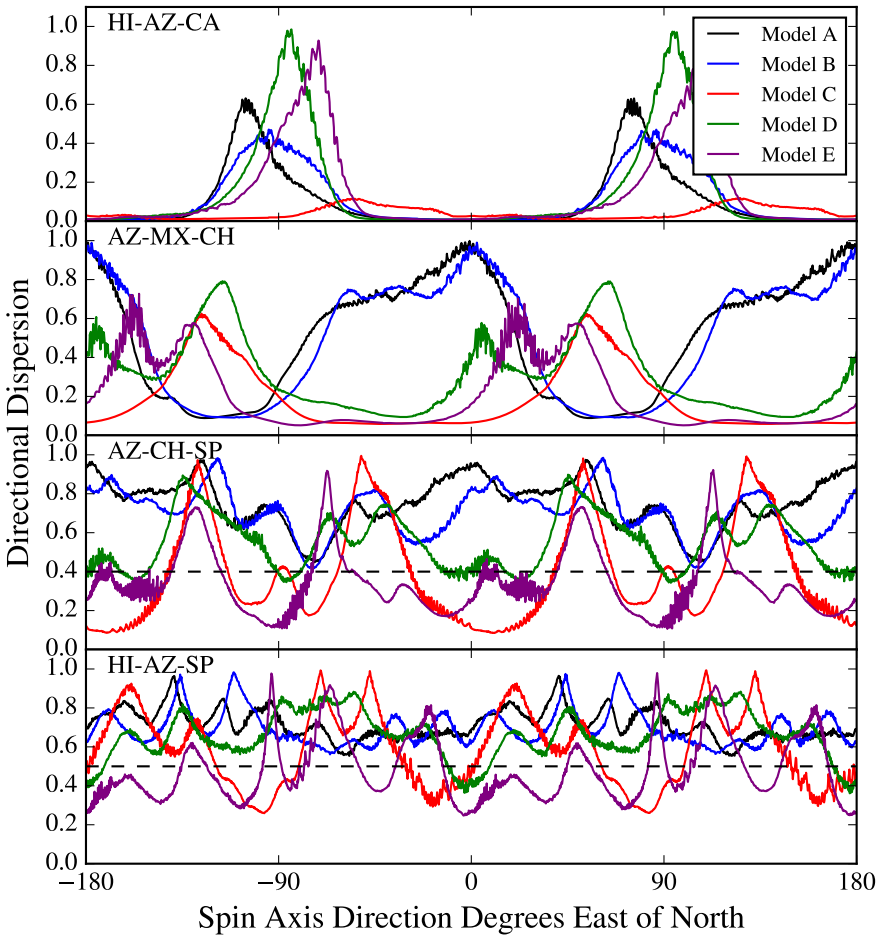

Figure 4.8 Directional dispersion of closure phase for the four closure phase triangles we consider as a function of the orientation of the black hole spin axis. The black dashed line in the third panel corresponds to a directional dispersion of 0.4 which corresponds to a gaussian with a dispersion of about 51°. The black dashed line in the fourth panel corresponds to a directional dispersion of 0.5 which corresponds to a gaussian with a dispersion of about 57°.

CH East orientation), the closure phase remains very stable throughout the observation, because the triangles remain away from the locations of the amplitude minima. In a third configuration (Model A, East orientation), the HI-AZ-CA triangle can follow Sgr A* for $\simeq$ 4 hr. Because the size of this baseline track is comparable to the extent of the high-variability region, the closure phase is variable throughout the observation. In the last

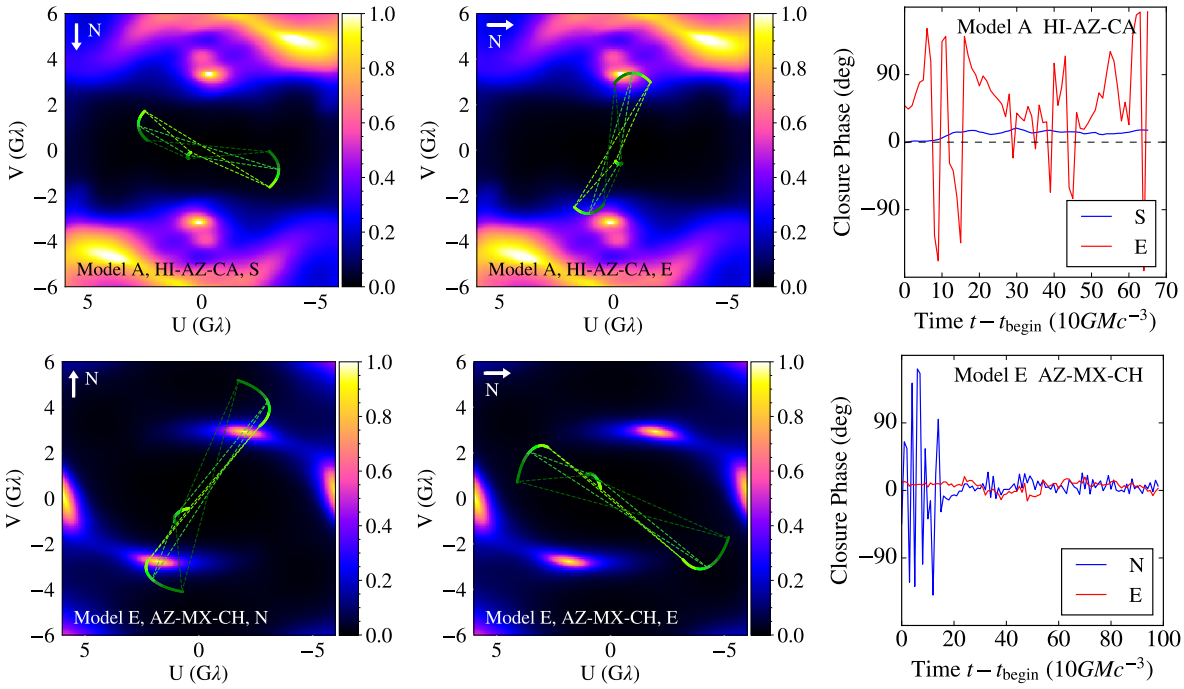

Figure 4.9 The effect of Earth rotation on the variability of closure phases. The top two color maps show the directional dispersion of Model A, the green tracks and dashed triangles correspond to the HI-AZ-CA closure triangle for a black hole pointing South (left panel) and East (middle panel). The bottom two color maps show the directional dispersion of Model E, the green tracks and dashed triangles correspond to the AZ-MX-CH closure triangle for a black hole pointing North (left panel) and East (middle panel). During the course of an observation both closure triangles move from light green to dark green. The rightmost column shows how closure phase varies as a function of time due to the combined effect of intrinsic variability from the simulation and the motion of the closure triangles shown in the color maps. Depending on the orientation of the black hole, the rotation of the Earth may move the triangles to regions of high variability of closure phases during an observation.

configuration (model E, North orientation), only a part of the longer ($\simeq$ 6 hr) baseline track cuts through the region of high variability, causing a very sudden decline in the closure phase variability in the midst of the observation.

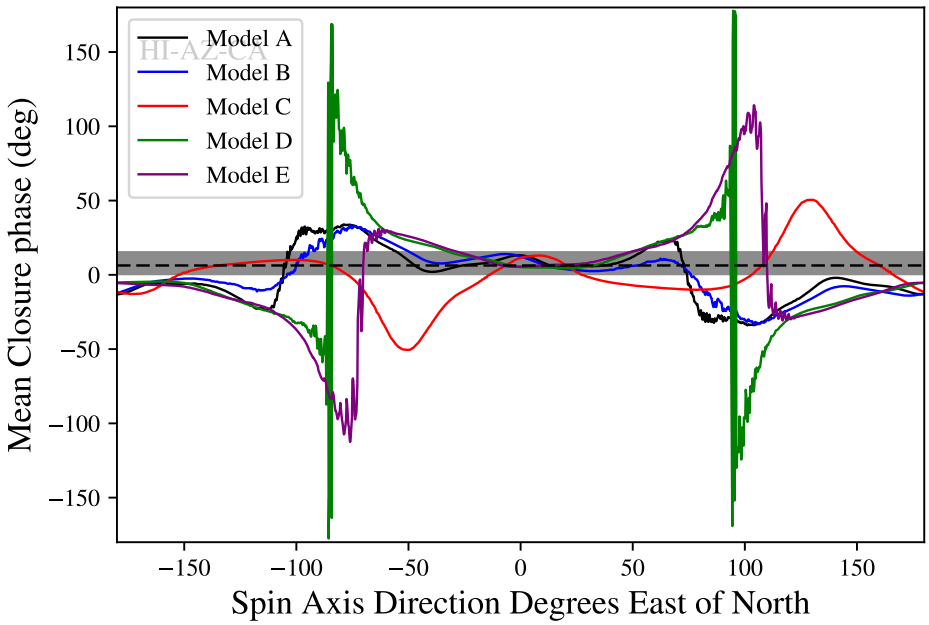

Figure 4.10 Directional mean closure phase for the HI-AZ-CA triangle (in degrees) as a function of the orientation of the black hole spin axis. The dashed black line corresponds to the median closure phase measured by the EHT for this triangle (Fish et al., 2016). The grey band corresponds to the range of median values in the various subsets of the data in Table 3 of Fish et al. (2016).

4.3 Discussion and Conclusions

We used five GRMHD+radiative transfer simulations of accretion onto Sgr A* to explore the predicted magnitudes of closure phases and their variability for the upcoming interferometric observations with the Event Horizon Telescope. We now compare these predictions to existing data to asses the prospects of distinguishing between different models and black hole spin orientations. Currently, there exist only limited measurements of the closure phases, spanning different epochs, along the HI-AZ-CA triangle. These yield a median value of $6.3^{+0.7}_{-2.0}$ degrees (Fish et al., 2016).

Statistically comparing the predicted distribution of closure phases to the observed

ones requires separately treating the formal and systematic uncertainties in the measurements. Because the variability in Sgr A*, as inferred both observationally (Meyer et al. 2008, Dexter et al. 2014) and from theoretical models (e.g. Dolence et al. 2012 and Chan et al. 2015a), points to a red noise process, comparing theoretical models to observations also requires incorporating the effects of finite observing time. We will perform a detailed comparison taking into account these considerations in a future study.

For a more preliminary comparison, we plot in Figure 4.10 not only the median measured closure phase but also a grey band that corresponds to the range of median values in the various subsets of the data in Fish et al. (2016). Even though both the disk-dominated SANE models and the funnel-dominated MAD models we analyzed here have significant asymmetric structures, Figure 4.10 shows that they produce closure phases and dispersions (Figure 4.8) in the HI-AZ-CA triangle that are consistent with the measurements for a wide range of black-hole spin orientations on the sky.

In the near future, closure phases will be detected with the full EHT array over a wide range of baseline triangles, covering long tracks in the $u - v$ plane. Our models show that, for triangles with size similar to that of the existing measurements, the closure phases will show little variability, unless one of the baseline vertices crosses a region of low visibility amplitude. However, the turbulent nature of the flow introduces significant variability on the small scales and, hence, significant closure phase variability might be present at large baseline triangles.

Despite this overall trend, the funnel-dominated MAD models that we studied pro-

duce less closure phase variability on the large triangles than the disk-dominated SANE models. This is because the images of the former are dominated by emission at the footpoints of the funnels and, even though these footpoints flicker, their image structure is not greatly influenced by the variability in the turbulent accretion flow. Therefore, future data will help distinguish between these possibilities. Furthermore, for both SANE and MAD models, we find that there is no trend between flaring events (see, e.g., Figure 1 in Medeiros et al. 2018a) and higher closure phase variability.

Because the highest dispersion in phase occurs at low visibility amplitude, the question of detectability arises when discussing the potential of observing such large dispersions. The EHT has already detected fringes at levels below 10% of the flux at zero baseline (Johnson et al., 2015). Additionally, the incorporation of ALMA into the EHT array (April 2017) is expected to increase the sensitivity of the latter by at least a factor of a few. In most models, the directional dispersion (D) is of order unity in places in $u - v$ space where the visibility amplitude is 5% of the zero baseline flux (see Figure 4.3), indicating that regions with dispersion of order unity will be detectable if present. Even with improved sensitivity, we also expect regions and periods of low visibility amplitudes that fall below the signal-to-noise threshold. In such cases, following a non-detection, we expect that when the source is detected again, the phase will be uncorrelated with the prior phase due to the highly variable nature of phases near regions of minima in visibility amplitude.

Our results have important implications for the image reconstruction techniques that

will rely on the closure phase data. Because of the possibility of substantial dispersion, even at small triangles, large amounts of high-quality data will need to be used to characterize the variability properties of the closure phases. Image reconstruction techniques will then need to take explicitly into account the observed variability. Alternatively, if image reconstruction techniques are used that rely on the assumption of a stationary image, the regions of high closure phase variability will need to be excised.

Chapter 5

Principal Component Analysis as a Tool for Characterizing Black Hole Images and Variability

The task of imaging and modeling the millimeter emission close to the horizon of an accreting black hole with the Event Horizon Telescope (EHT) encompasses a number of challenges. Interferometric imaging requires accurate synthesis of an image based on a sparse and incomplete set of Fourier visibilities (see, e.g., Honma et al. 2014; Bouman et al. 2016; Chael et al. 2016; Akiyama et al. 2017). Understanding the morphological diversity of the structure of the emission and its dependence on the physical parameters of the black hole rests on the comparison of such observations to high-fidelity simulations of the accretion flow (see, e.g., Mościbrodzka et al. 2009b, 2017; Dexter et al. 2009; Chan

et al. 2015b; Kim et al. 2016; Gold et al. 2017). As discussed in the introduction, the accretion flow itself is dynamic, potentially causing strong variations in the emission morphology over the very time scales required to synthesize an image with a large baseline interferometer (see, e.g., Lu et al. 2016; Medeiros et al. 2017, 2018a). In considering all of these issues, a common thread that emerges is a need to efficiently capture and characterize a complex series of images in diverse contexts. In this chapter, we apply Principal Component Analysis (PCA) to General Relativistic magnetohydrodynamic (GRMHD) simulations as an approach to addressing these challenges.

PCA is a mathematical approach to quantifying variability of an ensemble. In our case, the ensemble is a collection of images obtained from time-dependent simulation outputs of black hole accretion flows. PCA is non-parametric and does not incorporate any physical knowledge of the black hole or its accretion physics. Instead, PCA decomposes each image into a sum of orthogonal-basis eigenvectors (i.e., eigenimages) with eigenvalues that correspond to the brightness variance that each eigenimage captures. The eigenimages are then ranked by their eigenvalues, which allows minor variations to be discarded if desired. In other words, PCA allows for a compact and effective representation of the images in the ensemble. In practice, the implicit compression can be substantial, using perhaps only a dozen eigenvectors to represent over 1000 source images (Boroson & Lauer, 2010).

In this initial exploration, we show that PCA is particularly useful to help recognize and characterize the large-scale temporal variability in the morphology of the millimeter

emission close to the horizon of black holes such as Sgr A*and M87. We show that PCA can generate a compact orthogonal set of basis eigenimages that can accurately represent the ensemble of images generated by the suite of high-fidelity GRMHD simulations discussed in Chapter 2 and facilitate the efficient comparison of models to observations. This basis may also be used to provide a compact rendition of the ensemble in Fourier space and, in turn, a path to efficient representation of the sparse visibility observations. Furthermore, we show that PCA allows us to recognize "outliers" in the typical source morphology and identify, both in simulations and in observations, instances of episodic physical phenomena, such as magnetic reconnection and flaring events.

In parallel to the efforts to characterize and understand its origins, the EHT has a nearly orthogonal interest in the question of black hole variability, i.e., identifying emission signatures that are, in fact, not variable. In particular, the black hole shadow is expected to be invariant in time. It is, therefore, valuable to separate time-variable aspects of black hole images, such as turbulence and periodic variabilities in the accretion flow, from the constant signals arising from the black hole spacetime.

The structure of this chapter is as follows. We provide a brief development of the PCA formalism in §5.1 and demonstrate that a PCA basis that is derived in the image domain also provides a basis in the Fourier (i.e., visibility) domain. We apply our formalism to a simple ensemble of images in §5.2. In §5.3, we demonstrate the ability of PCA to represent a temporal sequence of high-fidelity simulated images of an accreting black hole. We demonstrate the use of PCA to compactify the space of images using dimensionality

reduction and to identify times of rare or unusual activity in the simulated time series in §5.4. In §5.5, we compare the spectrum of PCA eigenvalues to that of Gaussian and red-noise processes and show how the PCA eigenvalues are related to the underlying power spectrum of structures in the images. We conclude and discuss future applications of our work in §5.6.

5.1 Principal Component Analysis

Our goal is to use PCA to determine the dominant components in a set of images of black holes. In this section, we give a brief introduction to PCA and show that it may be applied directly to interferometric observables. The majority of this derivation follows Turk & Pentland (1991) with some differences that we will explicitly outline below.

5.1.1 Introduction to Principal Component Analysis

The principle of PCA is to calculate a set of orthogonal eigenimages (or eigenvectors) from an ensemble of images. We can then utilize this basis to compactly represent all of the images in the original ensemble as a linear combination of those eigenimages.

We denote an ensemble of m images by $I_n(x, y)$, where $n = 1, ..., m$ and the pair of coordinates (x, y) are used to represent the location of each of the $N \times N$ pixels on the image. For simplicity, each image can also be represented as a column vector $\mathbf{I}_n$ of length N^2. For our purposes, the ensemble of images will be comprised of a series of snapshots of a black hole accretion flow that are obtained from simulations or observations, although

the derivations we provide below are much more general.

As the basis of our decomposition, we choose to use the m orthogonal eigenimages $\mathbf{u}_k$ of the covariance matrix

$$\begin{aligned} C &= \frac{1}{m}\sum_{n=1}^{m} \mathbf{I}_n \, \mathbf{I}_n^T \\ &\equiv AA^T \, . \end{aligned} \tag{5.1}$$

In this equation, we defined the $N^2 \times m$ matrix A, such that its columns are the m images of the ensemble, i.e.,

$$A \equiv [\mathbf{I}_1 \; \mathbf{I}_2 \; \cdots \; \mathbf{I}_m]. \tag{5.2}$$

Strictly speaking and contrary to the notation of Turk & Pentland (1991), C is not a covariance matrix because we have not subtracted the mean from each image. However, we will refer to C as the covariance matrix throughout the paper to avoid introducing unnecessary terminology.

The covariance matrix C is an $N^2 \times N^2$ matrix that measures how the variation in the brightness of each pixel across the ensemble of images is correlated to the variation in brightness of every other pixel. We can write explicitly each element of the matrix C as

$$C_{ij} = \frac{1}{m}\sum_{n=1}^{m} A_{in} A_{jn}, \tag{5.3}$$

where the indices i and j correspond to the N^2 pixels ($i, j = 1, 2, ..., N^2$) and the index $n = 1, 2, ..., m$ corresponds to the different images in the ensemble.

In principle, we can then find the eigenimages $\mathbf{u}_k$ of the covariance matrix C by

diagonalizing it such that

$$\begin{aligned} C\mathbf{u}_k &= \mu_k \mathbf{u}_k \\ AA^T\mathbf{u}_k &= \mu_k \mathbf{u}_k \ . \end{aligned} \tag{5.4}$$

However, diagonalizing an $N^2 \times N^2$ matrix is computationally expensive and, in fact, not necessary. Because there are (at most) only m independent images in the ensemble, there are only m non-trivial eigenvalues and eigenvectors for this covariance matrix, which we can compute in an efficient way.[1]

We start by computing the eigenvectors and eigenvalues of the $m \times m$ matrix $L = A^T A$ such that

$$\begin{aligned} L\mathbf{v}_\gamma &= \lambda_\gamma \mathbf{v}_\gamma \\ A^T A\mathbf{v}_\gamma &= \lambda_\gamma \mathbf{v}_\gamma \ , \end{aligned} \tag{5.5}$$

where $\mathbf{v}_\gamma$ are the m eigenvectors of L, each of dimension m. It is then easy to show by multiplying both sides of equation (5.5) by A that the matrix L and the covariance matrix C share the same eigenvalues, i.e.,

$$\begin{aligned} AA^T A\mathbf{v}_\gamma &= \lambda_\gamma A\mathbf{v}_\gamma \\ CA\mathbf{v}_\gamma &= \lambda_\gamma A\mathbf{v}_\gamma. \end{aligned} \tag{5.6}$$

This equation also demonstrates that the vectors

$$\mathbf{u}_\gamma = A\mathbf{v}_\gamma, \tag{5.7}$$

of size N^2, are the eigenimages of the covariance matrix C with corresponding eigenvalues λ_γ.

[1] See, e.g., Appendix A of Strang (1988) for a discussion of this property.

The normalization of the eigenimages is, in principle, arbitrary. Following standard PCA convention, we normalize each eigenimage such that

$$\mathbf{u}_k^2 = \lambda_k \tag{5.8}$$

and

$$\sum_{k=1}^{m} \lambda_k = 1 \ . \tag{5.9}$$

Because the eigenvectors are orthogonal, it also follows that $\mathbf{u}_k \mathbf{u}_{k'} = \lambda_k \delta_{kk\prime}$, where $\delta_{kk\prime}$ is the Kronecker delta. Hereafter, we will use the notation $\mathbf{u}_k^2 = \mathbf{u}_k \mathbf{u}_k^T$ to denote the square of the magnitude of an eigenimage. The overall sign of each eigenimage is arbitrary and, in principle, the mean pixel value of an eigenimage may be negative and this caries no physical meaning. Here, for simplicity, we enforce the mean of each eigenimage to be positive.

Having obtained the eigenimages of our ensemble, we can then express any of its images as the linear combination

$$\mathbf{I}_n = \sum_{k=1}^{m} a_{nk} \mathbf{u}_k, \tag{5.10}$$

where

$$a_{nk} \equiv \frac{\mathbf{u}_k^T \mathbf{I}_n}{(\mathbf{u}_k^2)} \tag{5.11}$$

are the amplitudes of the projections of the images on the eigenimage basis. The column vectors $\mathbf{a}_k$ can be written as

$$\mathbf{a}_k = \frac{A^T \mathbf{u}_k}{(\mathbf{u}_k^2)}, \tag{5.12}$$

and are equivalent to $\mathbf{v}_k$, because

$$\mathbf{a}_k = \frac{A^T A \mathbf{v}_k}{(\mathbf{u}_k^2)} = \frac{L\mathbf{v}_k}{(\lambda_k)} = \mathbf{v}_k. \tag{5.13}$$

Equation (12), therefore, provides a simpler way of calculating the column vectors $\mathbf{a}_k$ compared to equation (11). The square of the magnitude of each image is equal to

$$\begin{aligned} \mathbf{I}_n^2 &= \mathbf{I}_n^T \mathbf{I}_n \\ &= \left(\sum_{k=1}^{m} a_{nk} \mathbf{u}_k^T \right) \left(\sum_{k'=1}^{m} a_{nk'} \mathbf{u}_{k'} \right) \\ &= \sum_{k=1}^{m} a_{nk}^2 \lambda_k \ . \end{aligned} \tag{5.14}$$

In our discussion of outlier detection below, we will also use the notion of the fractional contribution of eigenimage k to each snapshot n (cf. eq. (5.11)), which we define as

$$\begin{aligned} a'_{nk} &\equiv \frac{\mathbf{u}_k^T \mathbf{I}_n}{\sqrt{\mathbf{I}_n^2 \mathbf{u}_k^2}} \\ &= \frac{a_{nk}\sqrt{\lambda_k}}{\sqrt{\sum_{k=1}^{m} a_{nk}^2 \lambda_k}} \ . \end{aligned} \tag{5.15}$$

In principle, when we use the above basis set to reconstruct each original image in the ensemble, we need all m eigenimages. However, depending on the level of fidelity required and on the uniformity of the images in the set, the PCA decomposition makes it possible for us to reduce the dimensionality of the problem by only using the first few eigenimages to reconstruct an approximation of each of the original images. This approach becomes especially useful when only a few eigenimages are significant and the

rest are small. Naturally, the number of eigenimages used to construct the model depends on the particular application and does require judgment. For example, in observational data with real noise, the eigenimage expansion can be terminated when the model begins to overfit the noise. Boroson & Lauer (2010) presented a detailed analysis of the optimal way to terminate a PCA expansion given knowledge of the typical S/N ratio of the ensemble images. In characterizing images from simulations that do not include observational noise, the judgment of when to terminate the expansion is one of how much fidelity is required to capture the critical morphology of the image.

Lastly, we emphasize an obvious but important application of PCA. Given a set of eigenimages, the basis can also be used to represent and analyze images that are similar to those in the set used to define the eigenimages but that are not actually in the set itself. In the present context, this means that a basis constructed from a set of simulated images of an accreting black hole should be able to represent observations of the black hole, if the simulations are sufficiently realistic.

5.1.2 Principal Component Analysis in the Fourier Domain

Even though we presented the PCA formalism using a set of images, the data that we ultimately aim to work with are the complex Fourier components of the image, i.e., visibility amplitudes and phases. This is because the EHT is an interferometric array and directly measures the latter quantities. Ideally, we would like to devise a method for characterizing image variability that can be used in both image space and Fourier space

and that allows us to move freely between the two.

From a purely mathematical point of view, the image and Fourier domains are highly symmetric, and it is straight-forward to represent an operation in one domain with a complementary operation in the other domain. In practice, however, the two domains present strongly asymmetric viewpoints. The spatial distribution of radio emission close to the horizon of an accreting black hole is readily formulated and visualized with high-fidelity simulations in the image domain. The observations are obtained in the visibility domain, however, with relatively sparse coverage. Confronting the simulations with the observations requires a sophisticated synthesis of the visibility data into an interpretable form. One path is to use general purpose image reconstruction techniques, but these may suffer from less than optimal use of the expected morphology of the observations. Our approach, instead, will be to develop a basis directly in the visibility domain that encodes the expected behavior of the source as informed by simulations. We thus need to understand how the PCA basis of the simulations will relate to their visibilities. In this section, we show that the visibilities of the principal components of the simulation images are in fact the same as the principal components of the visibilities of these images.

We define the 2D discrete Fourier transform of an image as

$$\tilde{I}_\alpha = \sum_{i=1}^{N^2} F_{\alpha i} I_i \ , \qquad \alpha = 1, ..., N^2 \ . \tag{5.16}$$

Here, in order to account for the folding of the images into one-dimensional vectors, we have written the discrete Fourier operator in the compact form

$$F_{\alpha i} = e^{\frac{-2\pi \mathrm{i}}{N}[j\beta + k\delta]} \ , \tag{5.17}$$

where the indices j, k, β, and δ in the right hand side of this relation can be evaluated from the indices α and i via the relations

$$k = [(i-1) \mod N] + 1 , \tag{5.18}$$

$$j = \frac{i-k}{N} + 1 \tag{5.19}$$

and

$$\delta = [(\alpha - 1) \mod N] + 1 , \tag{5.20}$$

$$\beta = \frac{\alpha - \delta}{N} + 1 . \tag{5.21}$$

Note that in equation (5.17) we used the symbol i for the imaginary number to distinguish it from index i.

The Fourier transform of matrix A is simply

$$\tilde{A}_{\alpha n} = \sum_{i=1}^{N^2} F_{\alpha i} A_{in} \tag{5.22}$$

and we define the $m \times m$ matrix $L' \equiv \tilde{A}^T \tilde{A}$ as

$$L' \equiv \tilde{A}^T \tilde{A} = \begin{bmatrix} \tilde{I}_1 \tilde{I}_1 & \tilde{I}_1 \tilde{I}_2 & \cdots & \tilde{I}_1 \tilde{I}_m \\ \tilde{I}_2 \tilde{I}_1 & \tilde{I}_2 \tilde{I}_2 & \cdots & \tilde{I}_2 \tilde{I}_m \\ \vdots & \vdots & \ddots & \vdots \\ \tilde{I}_m \tilde{I}_1 & \tilde{I}_m \tilde{I}_2 & \cdots & \tilde{I}_m \tilde{I}_m \end{bmatrix} . \tag{5.23}$$

Our goal here is to show that this matrix is the same as L, i.e., that $L' = L$.

We write the vector product that appears in each element of matrix L' as

$$\begin{aligned} \tilde{\mathbf{I}}_f \tilde{\mathbf{I}}_g &= \sum_{\alpha=1}^{N^2} \tilde{I}_{\alpha f} \tilde{I}^*_{\alpha g} \\ &= \sum_{\alpha=1}^{N^2} \left(\sum_{i=1}^{N^2} F_{\alpha i} I_{if} \right) \left(\sum_{i'=1}^{N^2} F^*_{\alpha i'} I_{i' g} \right) . \end{aligned} \tag{5.24}$$

Because I_{if} and $I_{i'g}$ do not depend on α, we can rearrange the above equation as follows

$$\tilde{\mathbf{I}}_f \tilde{\mathbf{I}}_g = \sum_{i=1}^{N^2} I_{if} \sum_{i'=1}^{N^2} I_{i'g} \left(\sum_{\alpha=1}^{N^2} F_{\alpha i} F^*_{\alpha i'} \right). \tag{5.25}$$

The term in parenthesis above is the 2D Fourier transform of a constant and is equal to $\delta_{ii'}$ such that

$$\begin{aligned} \tilde{\mathbf{I}}_f \tilde{\mathbf{I}}_g &= \sum_{i=1}^{N^2} I_{if} \sum_{i'=1}^{N^2} I_{i'g} \delta_{ii'} \\ &= \sum_{i=1}^{N^2} I_{if} I_{ig} = \mathbf{I}_f \mathbf{I}_g \ . \end{aligned} \tag{5.26}$$

Therefore, each element of L is equal to that of L' so their eigenvectors and eigenvalues must also be equal ($L'\mathbf{v}_\gamma = \lambda_\gamma \mathbf{v}_\gamma$).

We now define the covariance matrix for the visibilities in analogy to that of the images as

$$C' = \tilde{A}\tilde{A}^{*T}. \tag{5.27}$$

As before, we can find the eigenvectors of C' by diagonalizing L' (see equation (5.6)), which demonstrates equivalently that $\tilde{A}\mathbf{v}_\gamma$ are eigenvectors of C' with eigenvalues λ_γ. In order to complete our proof, we must show that the eigenvectors $\tilde{A}\mathbf{v}_\gamma$ are equal to the Fourier transform of the eigenvectors $A\mathbf{v}_\gamma$. In other words, we must show that the principal components of the set of visibility maps is equal to the visibilities of the principal components of the set of images. This can be seen by evaluating each component of the

eigenvector $\tilde{A}\mathbf{v}_\gamma$ as

$$\begin{aligned}(\tilde{A}\mathbf{v}_\gamma)_\alpha &= \sum_{l=1}^{m} \tilde{A}_{\alpha l}(\mathbf{v}_\gamma)_l = \sum_{l=1}^{m} \left(\sum_{i=1}^{N^2} F_{\alpha i} A_{il} \right) (\mathbf{v}_\gamma)_l \\ &= \sum_{i=1}^{N^2} F_{\alpha i} \left(\sum_{l=1}^{m} A_{il}(\mathbf{v}_\gamma)_l \right) = (\tilde{A\mathbf{v}}_\gamma)_\alpha \ .\end{aligned} \tag{5.28}$$

Therefore, the visibilities of the principal components are indeed equal to the principal components of the visibilities. We have thus shown that the PCA basis can be developed in one domain, such as image space, but is readily applied in the complementary Fourier (or visibility) domain. This will allow us to use PCA to compare and possibly fit EHT data to simulations directly in the visibility domain. The maximally compact basis provided by the PCA approach may be well-suited to address the sparse coverage of the visibilities.

5.2 An Example of Principal Component Analysis

To elucidate how PCA works in practice, we present, in this section, a simple example that is easy to calculate and understand. We consider a Gaussian spot moving along a circular path and simulate 1080 snapshot images, as the spot completes an integer number (3) of orbits. Figure 5.1 shows a few example snapshots from this model. We calculate the principal components of this image set using the PCA formalism and show in Figure 5.2 the first few principal components. We also show in Figure 5.3 the spectrum of eigenvalues we obtain for this model.

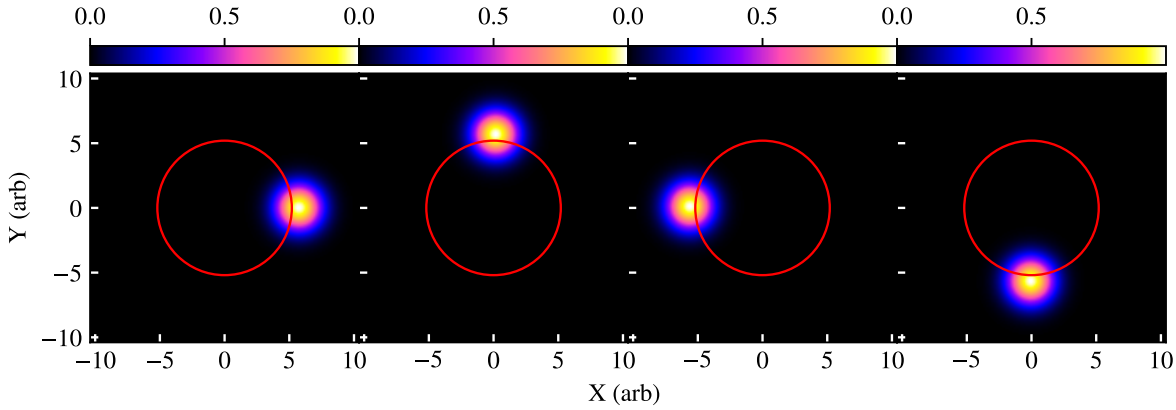

Figure 5.1 Example snapshots from a simple model of a Gaussian spot moving on a circular path. Here the red circle indicates the approximate trajectory of the center of the Gaussian spot. The linear scale of the image is arbitrary. We present PCA analysis of realistic GRMHD simulations later in the paper, but this simple example is useful for understanding how PCA decomposition of the simulations work.

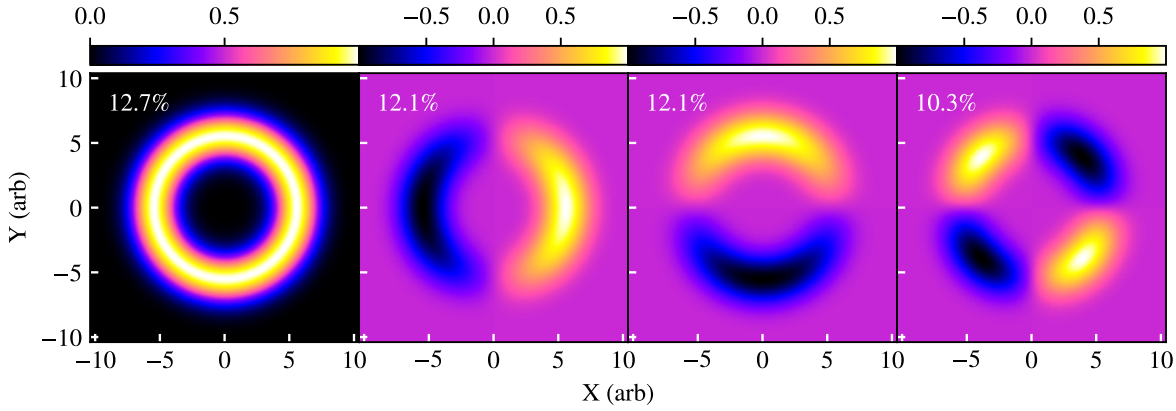

Figure 5.2 The first 4 components of the PCA decomposition of the Gaussian spot moving on the circular path shown in Figure 5.1. The eigenvalues which correspond to these four components are shown in the top left of each panel, respectively. Note that in this figure, and in all figures of principal components in the rest of the paper, each component has been normalized independently so fluxes cannot be compared between different components.

The first principal component, which has the largest flux variance ($\sim 12.7\%$), amounts to the average image of the various snapshots (modulo a normalization constant), i.e., it represents a ring surrounding the circular path with a width comparable to the width

of the Gaussian spot. This is not a general property of a PCA decomposition but is exact in the particular example discussed here and approximately correct in the PCA decomposition of the black hole images we will discuss in the next section. In the example of the orbiting Gaussian spot, all terms in each row of the $m \times m$ matrix L (which is also a covariance matrix) appear in each other row of the same matrix as well, but displaced at different columns. This is true because the product of any two images in the ensemble depends only on the relative positions of the Gaussian spots in the two images. In other words, the sum of the elements of each row of matrix L, i.e., $\sum_{n=1}^{m} L_{in}$ is constant. One of the eigenvectors of a matrix with elements that obey this property is a vector that has all elements equal to one (or actually any constant, depending on how the eigenvector is normalized), i.e., $\mathbf{v}_1 = [1\ 1\ 1\ 1\ ...\ 1]$. The eigenvector of the covariance matrix C that corresponds to this eigenvector of the matrix L is then (see eq.(5.7))

$$\mathbf{u}_1 = A\mathbf{v}_1 = \sum_{n=1}^{m} \mathbf{I}_m \ , \tag{5.29}$$

which (modulo a normalization constant) is nothing but the average image of the ensemble.

Most eigenimages, other than the lowest-order one, have pixels with significantly positive and negative brightness, as one would expect from an eigenvector decomposition. However, because all images are positive definite and the lowest-order eigenimage is the average of the ensemble of images, it follows that the lowest-order eigenimage is also positive definite. Moreover, because of the symmetry of the ensemble of images, components 2 and 3 of the spectrum of eigenimages (in Figure 5.2) differ only by a

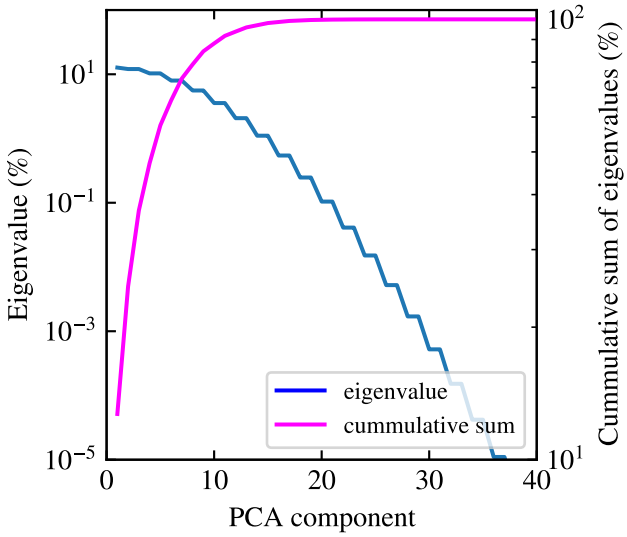

Figure 5.3 *(Blue curve)* The spectrum of eigenvalues for the PCA decomposition of the Gaussian spot shown in Figure 5.1; the eigenvalues have been normalized such that they sum up to 100%. The step-like features in this spectrum are present because the high degree of symmetry in this model causes the principal components to come in pairs with very similar eigenvalues (see the second and third panels of Fig. 5.2). *(Magenta curve)* The cumulative sum of the eigenvalues. Note that only the first ~ 40 of the 1080 components are shown and that the first 10 components contain 88% of the structural information.

rotation. The eigenvalue connected to each eigenimage is related to its variance (see equation (5.8)) and, hence, these two components correspond to the same eigenvalue. This behavior persists with higher components such that components come in pairs with similar eigenvalues. This creates the step pattern present in Figure 5.3.

Here and in all simulations of black hole images discussed in the sections below, the typical values of the amplitudes a_{nk} are very similar between different eigenimages, i.e., the typical values and distribution of the amplitudes a_{nk} depend weakly on k. Because of this and the fact that the eigenimages are normalized according to their eigenvalues (see eq. (5.8)), the spectrum of eigenvalues, such as the one shown in Figure 5.3, matches

very closely the spectrum of the relative contributions of each eigenimage to the reconstruction of any of the m images in the ensemble. As a result, we can use the spectrum of eigenvalues as a proxy for investigating the relative contribution of each eigenimage to the reconstruction of a typical image in the ensemble (see below for outlier detection). This is the reason why we normalize all eigenvalues so that they sum to unity (see eq.(5.9)) and we often quote them as percentages.

In the example of the circulating Gaussian spot that we discuss in this section, the eigenvalues drop dramatically after the first few, indicating that only a few components would be sufficient to reconstruct the original images. Specifically, under the assumption that the parameters a_{nk} are independent of k, we conclude that the first 10 (out of 1080) components account for $\approx 88\%$ of the structures present in the ensemble of images, while ~ 25 components account for nearly all of it. For this particular example, it is straightforward to understand why it takes only a small fraction of the eigenimages in order to reconstruct most of the structures seen in each of the images in the ensemble by estimating the number of substantially different images that are present in the ensemble. For the parameters used in this model, the FWHM of the Gaussian spot subtends $\sim 13^{\circ}$ as viewed from the center of the circular path. Therefore, the full circular trajectory can be decomposed into 28 distinct Gaussian spots that are (mostly) not overlapping. In other words, there are only 28 "resolution" elements in the circular trajectory and, therefore, the contribution of all but the first ~ 28 eigenimages can only be negligible.

5.3 Principal Components Analysis of Simulated Black Hole Images

We now apply PCA to the set of simulations discussed in Chapter 2. We focus on three of the five best-fit models that span the range of image morphologies and structural variability that we encountered in all our simulations. Specifically, Model B has a 1.3 mm image that is dominated by the accretion disk region and resembles a crescent shape, Model C has a 1.3 mm image that is dominated by the base of the jet funnel, while Model D has a 1.3 mm image that is a combination of both the base of the funnel and the disk.

We show in Figure 5.4 four example snapshots from Model B highlighting the structural variation in the emission region that is prominent in this model. Hereafter, when displaying images of black holes, we will measure all lengths in units of the gravitational radius GM/c^2, where M is the mass of the black hole and G and c are the gravitational constant and speed of light, respectively. The radius of the black hole shadow is approximately equal to 5 gravitational radii while the center of the shadow is displaced with respect to the center of gravity, depending on the spin of the black hole (see, e.g., Chan et al. 2013).

We perform PCA on the three simulations described above following the procedure outlined in §5.1. Each image set consists of 1024 images corresponding to the number of snapshots obtained from the accretion flow simulations that span $\approx$ 60 hours. In

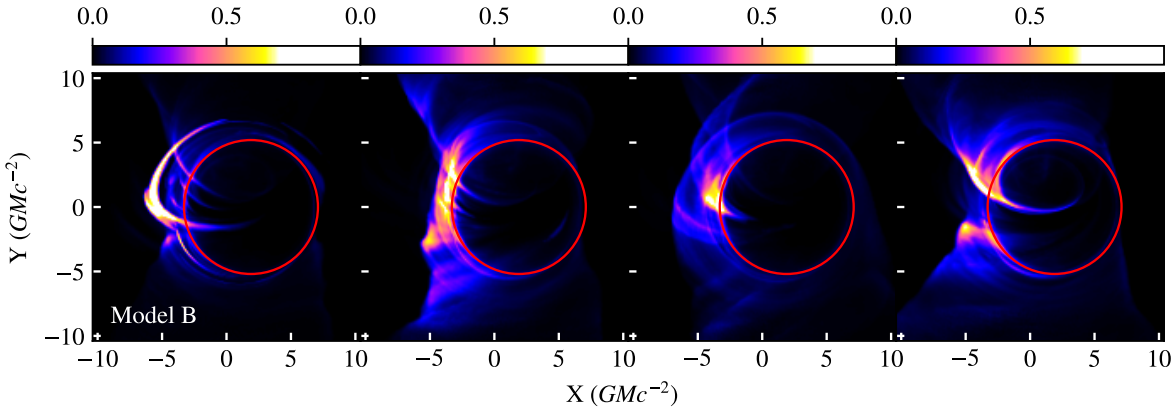

Figure 5.4 Four example snapshots of the ensemble of black hole images computed using Model B at a wavelength of 1.3 mm (see Chapter 2 for a description of the model and of the simulations). None of these snapshots correspond to an instant with a significant flare in the flux of the black hole. For this and the following figures, the peak flux in each panel has been normalized to unity so changes in overall flux have not been preserved. The original images span 32 GM/c^2 on each side and the full size images are used in all calculations; however, we choose to show only the innermost $\sim 20GM/c^2$ in the figures throughout the paper so that the black hole shadows are easy to distinguish. The red circles in the figures correspond to the expected size and location of the black hole shadow for each particular model. The location of the circle relative to the center of the image depends on the black hole spin and is not necessarily centered on the location of the black hole itself.

Figure 5.5, we show the first 4 eigenimages and their respective eigenvalues for the PCA decomposition of the three models. For all models, the first eigenimage (left) is similar to the time average of the ensemble of images (see Figure 2.3). This is true because all images have a dominant structure (i.e., a crescent or the footpoints of the funnel), on top of which the variability of the accretion flow introduces sub-dominant perturbations. As a result, the correlations between the various snapshots are very similar to each other and the arguments given in §5.2 for the dominant eigenimage apply here as well, but only approximately.

Although PCA is a purely mathematical tool and is agnostic about the physics of the

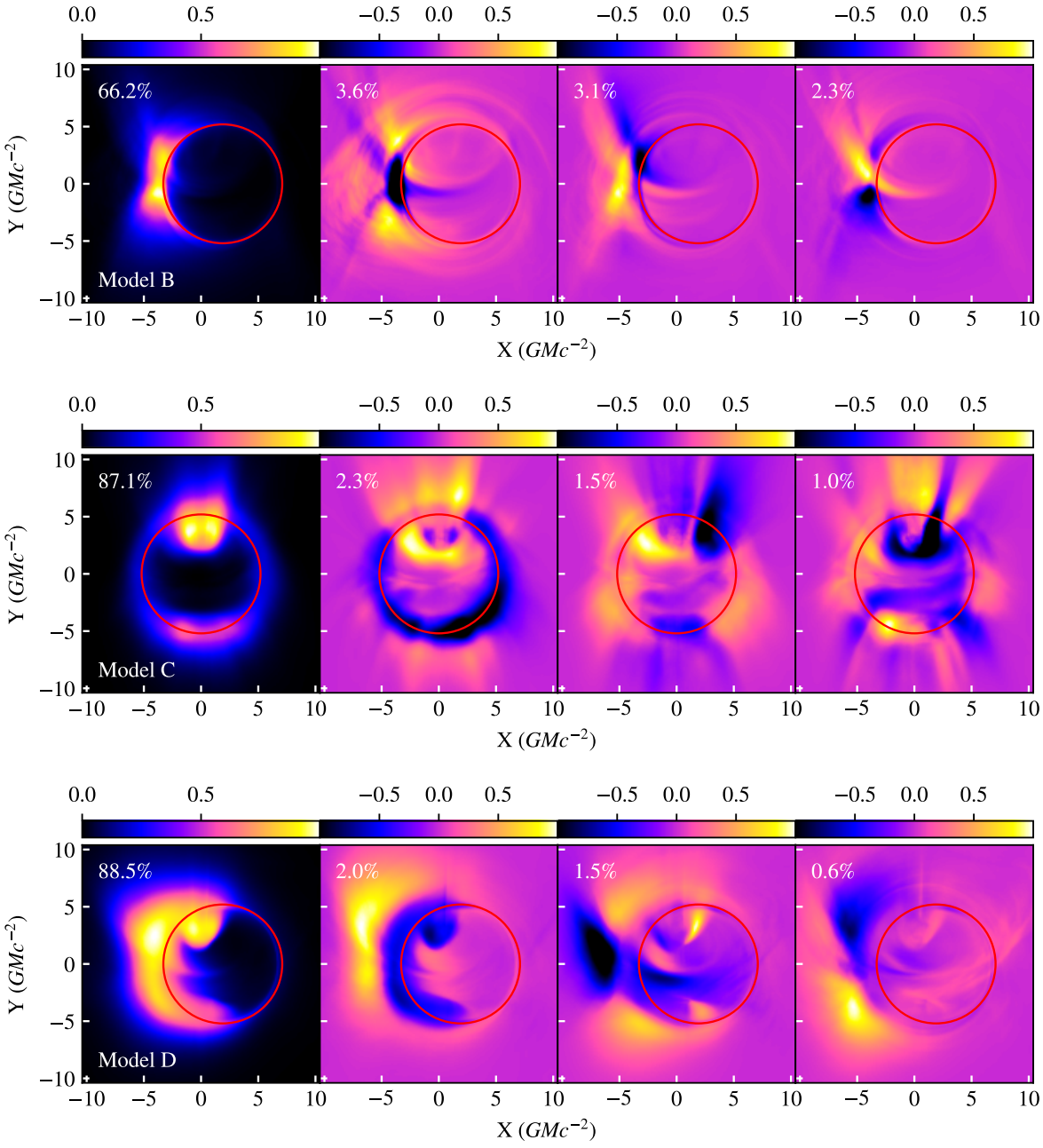

Figure 5.5 The first four principal components and their corresponding eigenvalues for the three GRMHD simulations (models B, C, and D) described in Chapter 2. The principal component for each simulation (leftmost panel) is approximately equal to the average image from the simulation (see Figure 2.3).

system, some of the components do appear to have identified important physical features. For example, the second component in Model B shown in the top row of Figure 5.5 appears to have identified a region of the Doppler boosted accretion disk (center of the crescent shape) that is very close to the black hole shadow and is highly variable in the simulations (see e.g., the second and third panels of Figure 5.4). The third and fourth components of Model B appear to be tracing the Doppler boosted walls of the funnel region. This also matches the behavior that can be seen directly in the simulation, where the relative brightness of the wall of the funnel region is highly variable (see, e.g., the fourth panel of Figure 5.4). Note that, due to the 60 degree inclination of the observer relative to the spin axis of the black hole in these simulations, the base of the funnel appears to come from within the black hole shadow but is actually positioned between the observer and the black hole.

In Model C (middle row), the second component highlights the edge of the black hole shadow while the other two components show various ways in which the structure of the emission at the base of the funnel varies. The PCA decomposition for Model D (bottom row) shows some features of Model B, i.e., that a crescent shape is present, and also some features of Model C, i.e., that the base of the funnel is an important variable feature in the image.

In Figure 5.6, we plot the spectra of eigenvalues of the PCA decomposition of the images from the three models. Unlike the example of the Gaussian spot discussed in §5.2, the eigenvalue of the first principal component in all three models overwhelms that

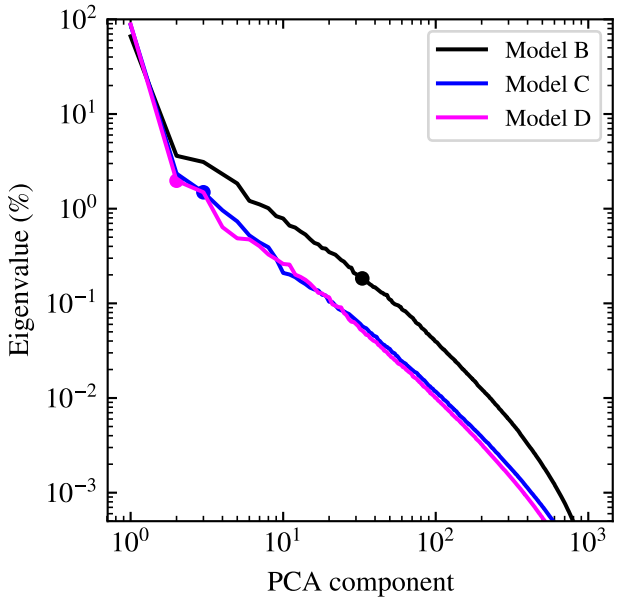

Figure 5.6 The eigenvalue spectra of the PCA decomposition of the images from the three GRMHD simulations we consider. The filled circles along each spectrum indicate the number of PCA components that are required to account for 90% of the image structures. The rapid decay of the eigenvalue spectrum indicates that PCA can be used to reduce significantly the dimensionality of the ensemble of images that arise in these simulations.

of the remaining components. For example, the eigenvalue of the first component of Model D corresponds to $\sim 89\%$, whereas the eigenvalue of the second component drops to only $\sim 2\%$. In other words, under the assumptions discussed in §5.2, only the first two components (out of 1024) are required to account for 90% of the structures in the images from Model D and only the first three components are required to reach the same level for Model C. This result indicates that PCA can be extremely useful in reducing the dimensionality of the images that arise in these GRMHD simulations and that only the first few components are needed to preserve the majority of the image structure.

Model B differs somewhat from the other two models in this regard. The eigenvalue

that corresponds to the first component is equal to $\sim 66\%$, i.e., it is $\sim 20\%$ less than in the other two models. Correspondingly, as many as 33 components are required to account for 90% of the structure seen in the images for model B, showing that this model contains significantly more structural variability than the other models. This is in agreement with the findings reported in Chan et al. (2015a) and Chapters 3 and 4, where the higher level of flux variability and flaring behavior was attributed to structural changes rather than to simple brightness fluctuations. Nevertheless, even for such a simulation that shows more significant structural variability, the required number of components (33) is significantly smaller than the total number of images, making PCA useful for dimensionality reduction. We explore this result further in the following section.

It is intriguing that despite the differences in the relative importance of the first ~ 10 eigenvalues, the eigenvalue spectrum declines with the same slope for the higher components in all models. This suggests a common origin for the slope of the eigenvalue spectrum, which we will explore in detail in §5.5.

Finally, we also apply the PCA analysis directly on the complex visibilities of our image set, which are the components of the 2D Fourier transform of each image. As we showed in §2.2, we can either calculate the complex visibility maps for each image in our ensemble and then perform PCA or calculate directly the complex visibility maps for each PCA component of the ensemble of images; the results will be identical. Given that the images correspond to vectors with real elements whereas the visibilities correspond to vectors with complex elements, we follow the second procedure, which is easier to

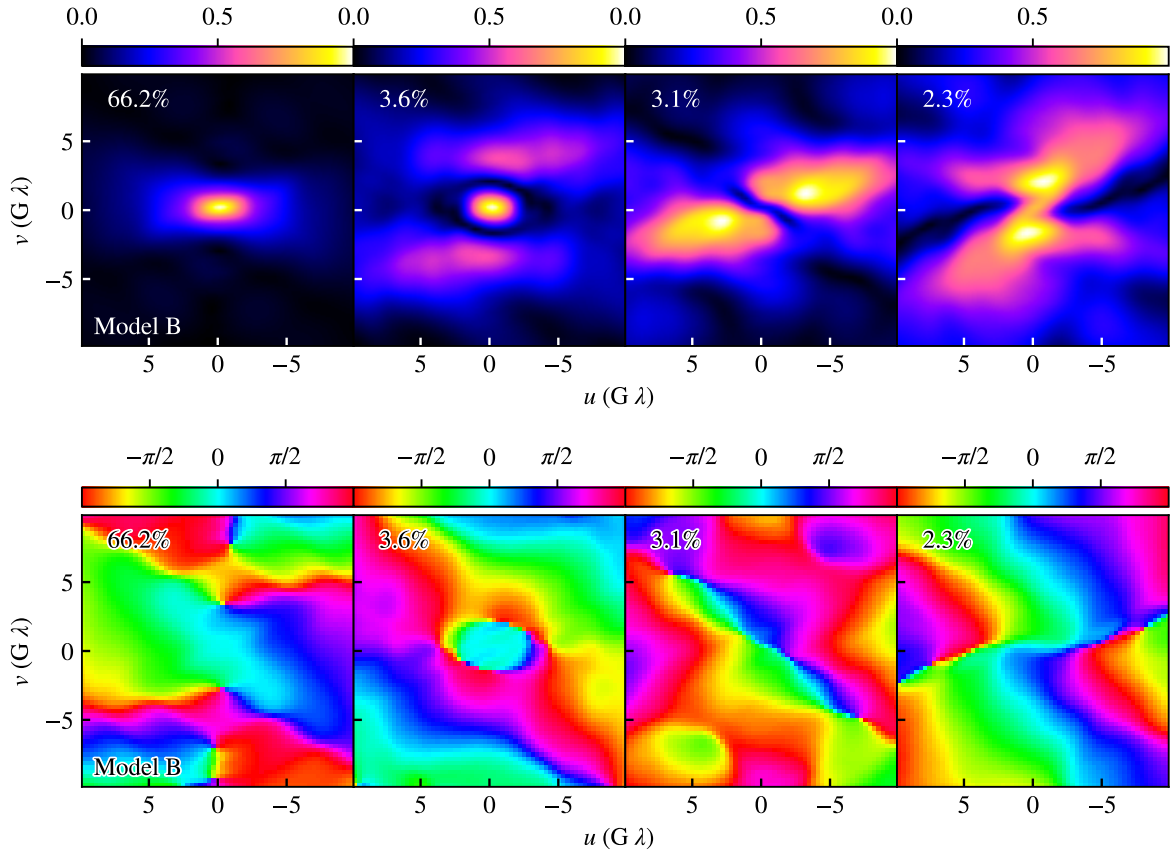

Figure 5.7 Visibility amplitudes (top row) and visibility phases (bottom row) of the first four components of the PCA decomposition of Model B (cf. the top row of Figure 5.5). Higher components contribute significantly at increasingly longer baselines.

implement. In Figure 5.7, we show the first four PCA components of the visibility amplitudes and visibility phases of Model B. As expected, the structures of the visibility amplitudes and phases changes significantly between these four components. In fact, the visibility amplitudes of higher components have more power at longer baselines, which is a direct consequence of the fact that they contain smaller scale structures.

5.4 Dimensionality Reduction and Outlier Identification

As we discussed in the previous section, only the first few PCA components are required to account for the majority of the structure seen in the images from each GRMHD simulation. Components with smaller eigenvalues both contribute less to the brightness of each pixel in the image (see discussion at the end of §5.2) and account primarily for small-scale structures (see Figure 5.7). As alluded to in the introduction, this conclusion (often referred to as dimensionality reduction) also offers the possibility of using a small number of measurements, such as those possible with the sparse coverage of the EHT array, to reconstruct the persistent image of a black hole and, therefore, extract the information that is most relevant for detecting its shadow. To explore the idea of using the first few components to describe the persistent structure from the variable flow, we calculate and compare reconstructions of images from the simulations using the first few components of the PCA decomposition to the original images.

Figure 5.8 shows an example snapshot from Model B compared to its reconstruction using the first 10, 40, and 100 out of the 1024 PCA components. Although the reconstructions with only a small number of components do not reproduce the finer details of the images, they do capture their overall structure. The fidelity of reconstruction naturally increases as more components are added. The number of components we may choose to keep in a particular reconstruction and, hence, the degree of dimensionality

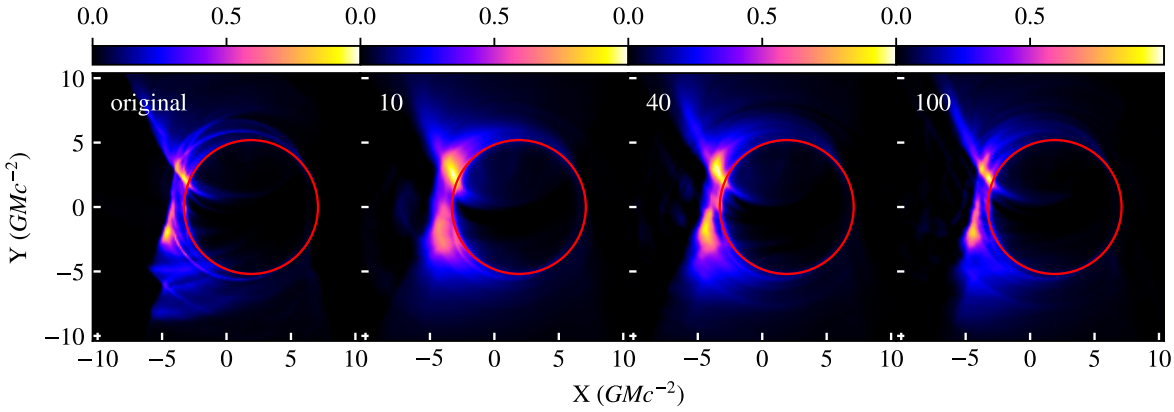

Figure 5.8 The left panel shows a typical snapshot from Model B. The three right panels show the same snapshot from Model B but reconstructed using only the first 10, 40, and 100 components from the PCA decomposition. The reconstruction using only the first 10 components smooths over the fine scale structure but faithfully reproduces the overall brightness distribution of the full image.

reduction will naturally depend on the goal of the reconstruction. Nevertheless, even at a qualitative level, this figure suggests that dimensionality reduction by factors of 10 to 100 may be achievable in characterizing black hole images with PCA.

The snapshot in Figure 5.8 is typical and, therefore, can easily be reconstructed using only the first few PCA components. However, there may be snapshots within a given simulation that are much harder to reconstruct because the structure of the image is unusual compared to the rest of the ensemble. For the purposes of this work, we will define an outlier as an image that cannot be easily reconstructed by the first few (or a "typical" number of) eigenimages. As we will show below, PCA allows us to devise an algorithmic approach for outlier detection. When we apply PCA to numerical simulations, this outlier detection will enable us to efficiently identify instances where rare and episodic events occurred in the simulation, e.g., a flare in the emission properties of

the accretion flow. When we apply PCA to observational data, detecting outliers will allow us to identify similar episodic events that may be caused by physical phenomena or data corruption.

There are many ways of using PCA to identify outliers in a set of images. A common method measures the Euclidean distance of each image in the hyperspace spanned by the set of eigenimages (often related to the Mahalanobis distance, Mahalanobis 1936). In implementations of outlier detection based on the Mahalanobis distance, the ensemble of images (or other data) is often standardized such that the distribution of pixel brightness within each image has been mean centered and scaled by its standard deviation. Because we have chosen not to standardize our data set, applying the Euclidean distance method directly to our PCA implementation would identify as outliers images that are simply brighter than the average image but without necessarily any substantial structural difference. In the context of using PCA to describe simulations of accreting black holes, we can easily identify such bright events by simply looking at large excursions of the total flux from the mean value. Our goal, instead, is to identify as outliers those snapshots with structures in the images that are substantially different from those of the typical snapshots. For this reason, we define a Euclidean distance using the fractional contribution of each eigenimage to the reconstruction of an image in the ensemble (see eq. (5.15)).

We will consider a given snapshot ($\mathbf{I}_n$) as typical, if it can be adequately reconstructed by the first l eigenimages (l can be chosen based on the particular distribution and

application). To quantify the degree to which a snapshot is atypical, we define the quantity

$$R_{nl} \equiv \frac{1}{\sum_{k=l+1}^{m} w_k} \sum_{k=l+1}^{m} \left(\frac{a'_{nk} - \langle a'_k \rangle}{\sigma^2_{a_k}} \right)^2 w_k \tag{5.30}$$

that measures the weighted squared Euclidean distance from the mean of the distribution of a'_{nk}, scaled by the standard deviation of the distribution, and projected onto the subspace of eigenimages that is not being used in the reconstruction. Here, the mean of the distribution

$$\langle a'_k \rangle = \frac{1}{m} \sum_{n=1}^{m} a'_{nk}, \tag{5.31}$$

provides a measure of the average coefficient of an eigenimage needed to reconstruct the snapshots in a given set of images,

$$\sigma^2_{a'_k} = \frac{1}{m} \sum_{n=1}^{m} (a'_{nk} - \langle a'_{nk} \rangle)^2, \tag{5.32}$$

shows the spread in that distribution, and w_k is an appropriate weight function. We set the weight function to $w_k = \lambda_k$ because, in our implementation, the typical contribution of each eigenimage to any reconstruction is proportional to $\sqrt{\lambda_k}$ and we want to give more weight to the most dominant eigenimages when identifying outliers.

In Figure 5.9 we show R_{nl} for $l = 5$, 10, and 20 for all snapshots in Model B as well as the normalized lightcurve. A number of time instances can be easily identified as atypical, i.e., with $R_{nl} \gg 1$, but these instances do not necessarily correlate with large brightness excursions. To examine this further, we show in Figure 5.10 three original snapshots as well as the reconstructions using the first 5, 10, and 20 principal components. The top

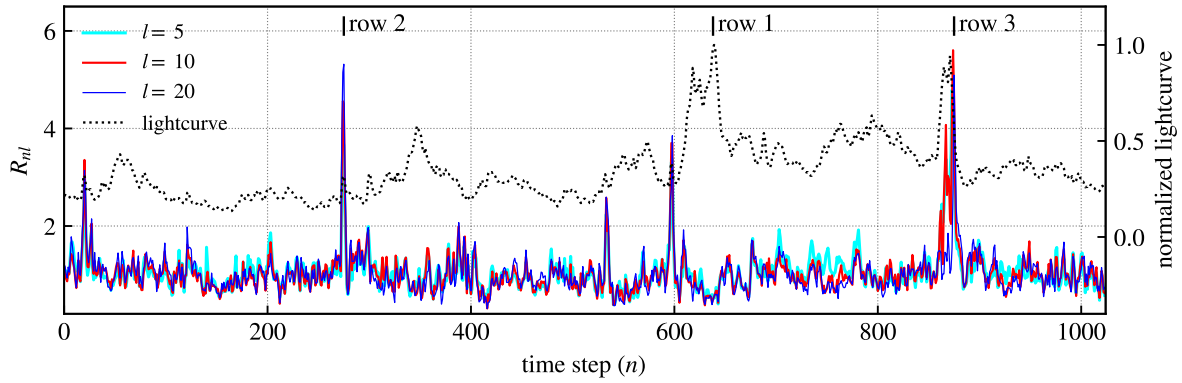

Figure 5.9 The dotted black line shows the normalized light curve for Model B. The cyan, red, and blue curves correspond to the quantity R_{nl} for $l = 5$, 10, and 20, respectively. The peaks in the cyan, red, and blue curves indicate time instances that cannot be adequately reconstructed by only the first few components and are, hence, identified as outliers. The three time instances identified as 'row 1','row 2', and 'row 3' correspond to the images that are shown in Figure 5.10.

row (denoted as "row 1" in Figure 5.9) shows an example of a time instance that is not identified as an outlier but corresponds to the largest flux excursion in this simulation. Clearly, this snapshot can be easily reconstructed by the first 10 eigenimages and has a low R_{nl} value for all three values of l. This snapshot, despite being substantially brighter than the others, does not correspond to a significant structural change in the image. The second row ("row 2") shows a time instance that is identified as an outlier but does not correspond to a significant flux excursion. The morphology of the image is quite unusual compared to the rest of the simulation and a reconstruction with 20 eigenimages fails to capture the general structure of the image. The third row ("row 3") shows a time instance that is both identified as an outlier and shows a significant flux excursion. The reconstruction of this snapshot with 20 eigenimages is also inadequate.

These results demonstrate that, in our simulations, flux excursions and unusual image

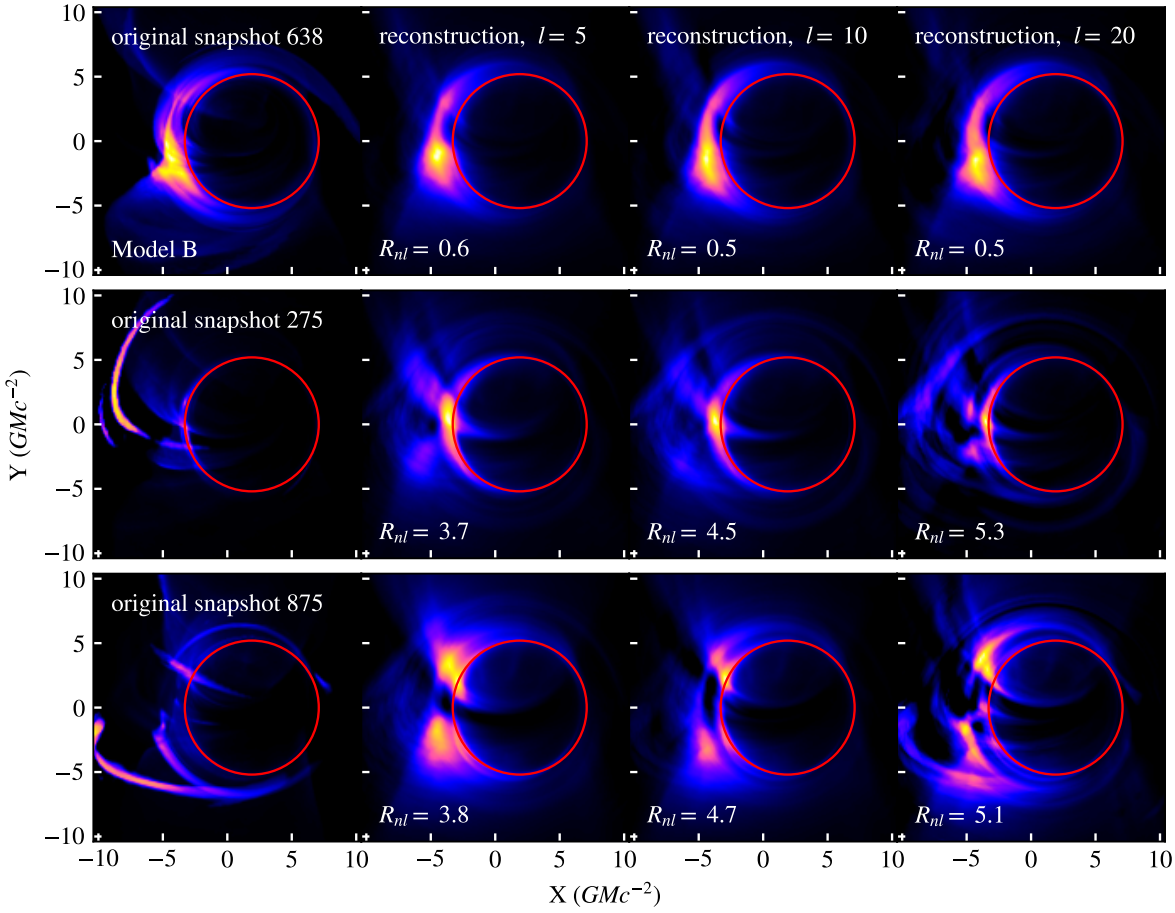

Figure 5.10 The leftmost panels show three snapshots from the ensemble of images calculated for Model B. In each row, the three consecutive panels show reconstructions using the first 5, 10, and 20 principal components. The top row corresponds to a time instance that is not identified as an outlier, but corresponds to a large flux excursion from the accretion flow (this time step is denoted by "row 1" in Figure 5.9). Note that this image is well-fitted with the first 20 eigenimages, and thus has a small R_{nl} value. The second row corresponds to a time step which is identified as an outlier with no significant flux excursion. The third row corresponds to a time instance that is both identified as an outlier and shows a large flux excursion. Both of these latter images are poorly fitted by even 20 eigenimages and have been identified as outliers by their R_{nl} values.

morphologies are not necessarily coincident but the two can be disentangled with the use of the quantity R_{nl} that we have introduced here.

5.5 Understanding the Eigenvalue Spectrum of PCA

In this section we turn our attention to understanding the behavior of the spectrum of eigenvalues of the PCA decomposition of the GRMHD simulations. Specifically, we focus on the higher-order components, which have small eigenvalues and contribute primarily to the small-scale, variable structures seen in the images. We aim to understand the origin of their eigenvalue spectra, which have the intriguing property of being power laws with very similar slopes in all simulations. This allows us to explore whether the spectra of eigenvalues are related to the underlying properties of GRMHD turbulence and, hence, whether measuring them in observations can help us better understand turbulence in accretion flows.

The power-law shapes of the eigenvalue spectra are reminiscent of noise processes. For this reason, we begin by exploring the PCA eigenvalue spectrum of Gaussian noise in an image and then continue with a red-noise process.

5.5.1 Gaussian Noise

We consider a Gaussian noise model where the brightness of each pixel is a random number taken from a Gaussian distribution centered at zero. We perform PCA on 1024 images with independent realizations of Gaussian noise with a standard deviation of $\sigma = 0.5$ over 512×512 pixels. Figure 5.11 shows the first few principal components and their respective eigenvalues. Any two images in the ensemble are statistically uncorrelated. However, the elements of matrix L are not zero because small, non-zero residual

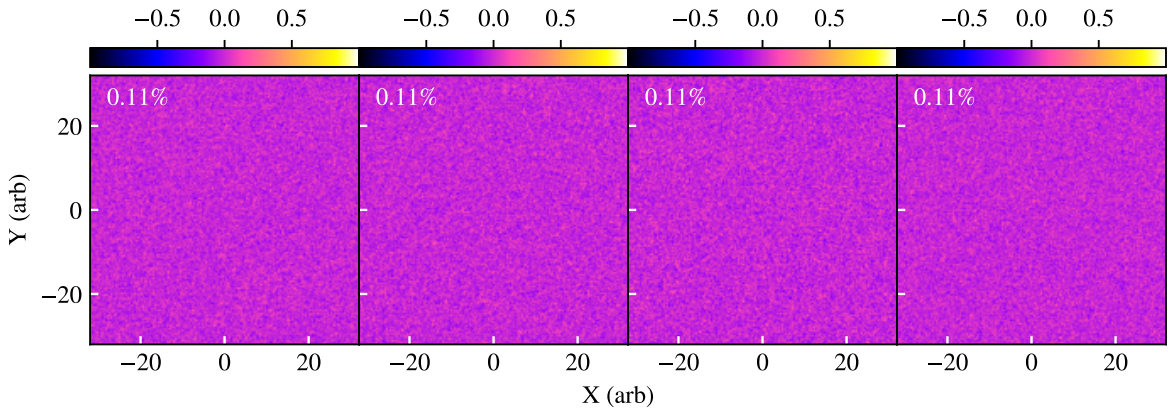

Figure 5.11 The first 4 components of the PCA decomposition of 1024 images with purely Gaussian noise and their respective eigenvalues. The brightness of each pixel in these images is a random number taken from a Gaussian distribution centered at zero with a width of $\sigma = 0.5$. Because each image is uncorrelated from the rest, all principal components have very similar eigenvalues and dimensionality reduction using PCA is not possible for this system.

correlations between any two images remain because of the finite number of pixels in each image and the statistical nature of noise. The eigenvalues of all components are similar, indicating that all of the principal components are of similar importance and dimensionality reduction is not possible for this configuration.

The presence of minor correlations between pairs of images leads to a distribution of eigenvalues of finite width. Because, in PCA, we count the eigenvectors in decreasing order of their eigenvalues, this distribution leads to a spectrum of eigenvalues with a non-zero slope. Figure 5.12 shows the spectrum of the eigenvalues of our realization of the Gaussian noise model. The eigenvalues are normalized such that they sum to unity (see eq. (5.9)). Given that our simulation of Gaussian noise involves $m = 1024$ images, there are 1024 non-trivial eigenvalues of similar magnitude with a mean of $1/1024 \simeq 0.098\%$. To estimate the standard deviation of the distribution of eigenvalues, we consider the

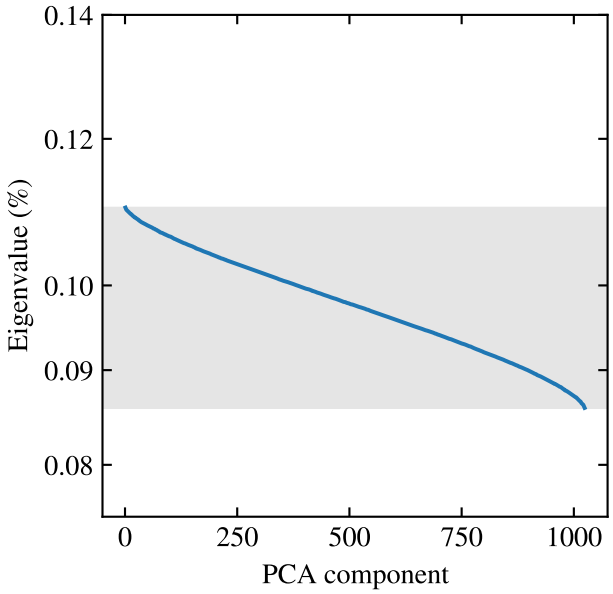

Figure 5.12 The eigenvalue spectrum for the PCA decomposition of an ensemble of images with Gaussian noise. The gray rectangle represents the expected range of eigenvalues, given the statistical nature of Gaussian noise (see text). Note the very small range of the y-axis.

fact that there are mN^2 individual realizations of the Gaussian noise in the ensemble of $m = 1024$ images with $N^2 = 512^2$ pixels each. We, therefore, expect the standard deviation of eigenvalues to be comparable to

$$\sigma = \frac{1}{\sqrt{mN^2}} \simeq 0.006 \left(\frac{m}{1024}\right)^{-1/2} \left(\frac{N}{512}\right)^{-1} \%. \tag{5.33}$$

The full range of eigenvalues in our particular realization of images is from 0.0859% to 0.1101%, which corresponds to a width of $\approx 4\sigma$. In Figure 5.12, we show the range of 4σ around the expected mean magnitude of the eigenvalues to visualize this result.

In contrast to Gaussian noise, the spectra of PCA eigenvalues for our GRMHD simulations, including the power-law tails at large eigenvector numbers, do not depend on either the number of images or the number of pixels. We tested this by decreasing our

spatial and temporal resolution by factors of 2 and 4 but preserving the total time span and image size. This behavior indicates that the structures present in our simulations are much larger than the pixel size; as a result, changing the number of pixels does not alter the PCA decomposition. A similar argument is valid for the lack of dependence on the number of images. For this reason, we now turn our attention to noise spectra with maximum power at scales that are larger than the pixel sizes.

5.5.2 Red Noise

The spatial and time variability of images of accretion flows, such as those from Sgr A*, are expected to be approximated by red-noise power spectra. This is based both on the observationally measured flux variability of Sgr A*(Meyer et al. 2008, Dexter et al. 2014) as well as on theoretical models (e.g., Dolence et al. 2012 and Chan et al. 2015a). Other physical phenomena that affect black hole images, such as refractive scattering in the intervening medium, are also expected to introduce noise at different characteristic scales (e.g., Johnson & Narayan 2016). Because of such considerations, we consider here an ensemble of images with structure described by an isotropic, red-noise 2D Fourier spectrum given by

$$P(q) = 2^{\alpha}\pi\alpha e^{-(q/q_{\rm max})^2}(q^2 + q_{\rm min}^2)^{-(1+\alpha/2)} \tag{5.34}$$

such that the image brightness at a location given by the transverse vector $\vec{r}$ on the image plane is

$$I(\vec{r}) = I_0 \int d^2q P(q) \exp\left[-i\vec{q}\cdot\vec{r}\right] \ . \tag{5.35}$$

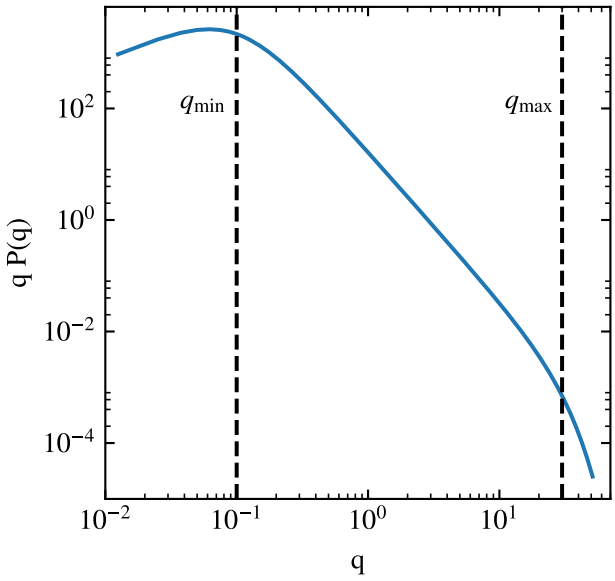

Figure 5.13 The red-noise spectrum given in equation (5.34) with $q_{\max} = 30$, $q_{\min} = 0.5$, and $\alpha = 5/3$. The parameters $q_{\min}$ and $q_{\max}$ determine the locations of the first and second break in the spectrum, respectively, and α specifies the slope of the region between $q_{\min}$ and $q_{\max}$.

Here, $q_{\min}$ and $q_{\max}$ determine the location of the first and second breaks in the spectrum and consequently the sizes of the largest and smallest structures in the images, respectively. The parameter α determines the slope of the power spectrum in the region between $q_{\min}$ and $q_{\max}$.

Figure 5.13 shows a plot of this spectrum with $q_{\max} = 30$, $q_{\min} = 0.5$, and $\alpha = 5/3$. As expected, for $\alpha = 5/3$, there is very little power at the small scales where $q_{\max}$ is relevant; the majority of the power is at the larger scales related to $q_{\min}$. Figure 5.14 shows some examples of images with different red-noise realizations. By construction, the structures in these images are almost entirely resolved in an $N \times N$ image, as long as the size of each pixel is much smaller than $1/q_{\max}$.

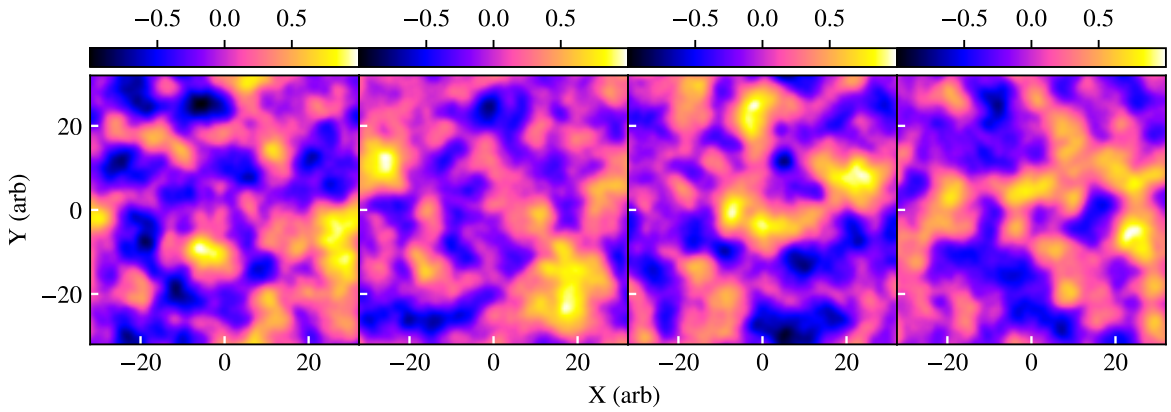

Figure 5.14 Examples of images with different realizations of red-noise with the isotropic power spectrum shown in Figure 5.13 and random phase fluctuations. As expected for $\alpha = 5/3$, most of the power is at scales $\simeq 1/q_{\rm min}$.

In order to investigate the effect of red noise on the PCA of images, we construct numerous sets of 1024 images for different values of the red noise parameters, such as those in Figure 5.14, and perform PCA on the set. We now explore the dependence of the PCA decomposition of these images on the parameters of the red-noise spectrum.

The spectrum of PCA eigenvalues of red noise does not depend on the number of pixels N per image, as long as the size of the dominant scale of the noise is fully resolved, i.e., as long as $L/N << 1/q_{\rm min}$, where L is the linear size of the image. This is similar to the PCA results for the images of the GRMHD simulations and unlike those of the Gaussian noise simulations discussed earlier. The eigenvalue spectrum is also independent of $q_{\rm max}$ as long as $q_{\rm max} >> q_{\rm min}$ and $\alpha > -1$ because, if these conditions are met, there is negligible power at scales $\sim 1/q_{\rm max}$ to affect the PCA decomposition significantly.

Figure 5.15 shows the spectrum of PCA eigenvalues and its dependence on $q_{\rm min}$. For $\alpha > -1$, $1/q_{\rm min}$ determines the size of the dominant scale of the noise structures. The

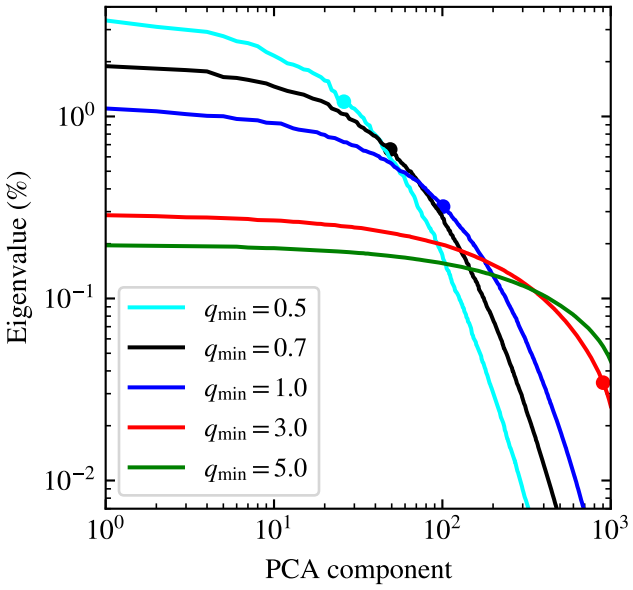

Figure 5.15 The spectra of PCA eigenvalues for ensembles of images with isotropic red noise and for different values of the parameter $q_{\rm min}$; the remaining parameters are the same as in Figure 5.13. For lower values of $q_{\rm min}$ the dominant scale of the structures in the images is larger and fewer PCA components are required to reproduce the majority of structure in the images. The filled circles on each curve indicate the number of PCA components that is equal to the approximate number of different noise structures that can fit in the image, i.e., where the number of components is equal to $L^2 q_{\rm min}^2$, where L is the size of the image.

number of dominant noise structures that can fit in an image of size L is

$$n = \left(\frac{L}{1/q_{\rm min}} \right)^2 = L^2 q_{\rm min}^2 \ . \tag{5.36}$$

We, therefore, expect, following the discussion in §5.2, that this number corresponds to the number of dominant PCA components. This is shown in Figure 5.15, where the filled circle on each spectrum corresponds to the eigenvalue of the $n-$th PCA component given by the above relation. Clearly, as $q_{\rm min}$ increases, the structures on the images become smaller and more PCA components are necessary to reconstruct with fidelity the original ensemble of images.

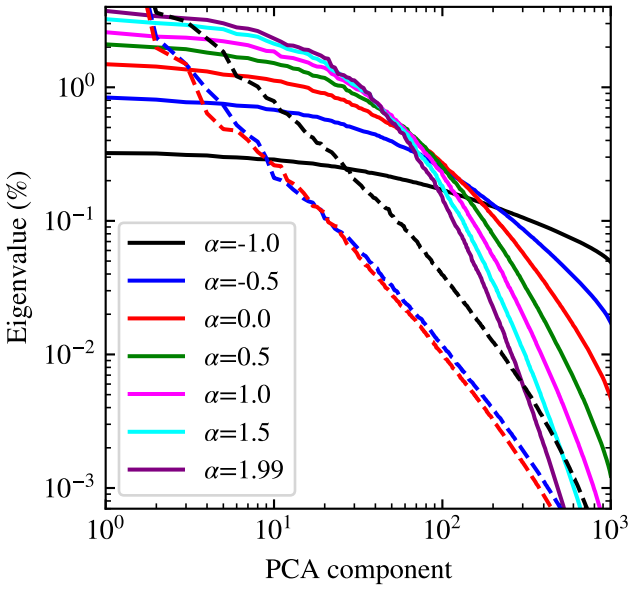

Figure 5.16 The spectra of PCA eigenvalues for ensembles of images with isotropic red noise and for different values of the power-law index α; the remaining parameters are the same as in Figure 5.13. For comparison, the eigenvalue spectra of the GRMHD models B, C, and D are also included in the black, blue, and red dashed lines respectively. The power law slope of the eigenvalue spectrum after the break depends strongly on α.

For a given value of the parameter $q_{\rm min}$, the number of images m in the ensemble determines whether the spectrum of eigenvalues has converged or not. Indeed, as we discussed above, for small values of $q_{\rm min}$, which correspond to large dominant noise structures, a small number of eigenimages is required to reconstruct with fidelity the full ensemble of images. In this case, i.e., as long as $m \gg n = L^2 q_{\rm min}^2$, the eigenvalue spectrum has converged and its shape depends only very weakly on the number m of images in the ensemble.

Figure 5.16 shows the spectrum of PCA eigenvalues for images with Fourier spectra characterized by different power-law indices $\alpha > -1$. As in Figure 5.15, the spectra are relatively flat until the $n-$th PCA component but then turn into power laws with indices

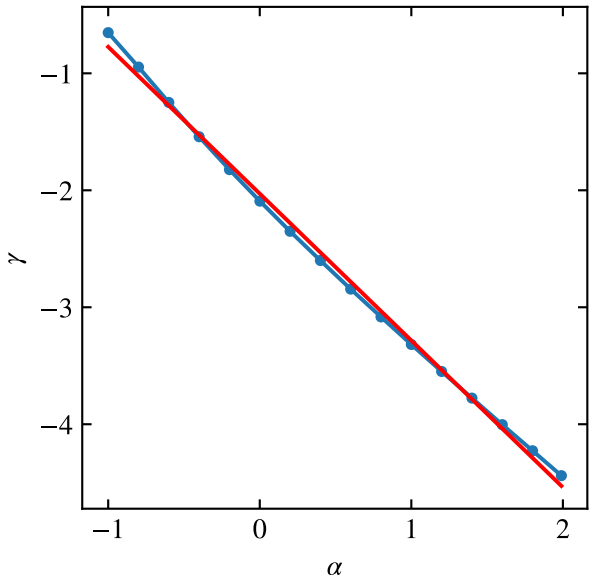

Figure 5.17 The power-law index γ of the spectra of PCA eigenvalues as a function of the power-law index α of the red-noise Fourier spectra that was used to generate the images. The blue circles are the values obtained numerically from fitting the eigenvalue spectra with power-law functions; the red line is a linear fit to the blue circles.

that appear to be correlated with α. For $\alpha \lesssim -1$, which we do not show, the dominant noise structures occur at the small scales $\simeq 1/q_{\max}$ and the resulting eigenvalue spectra are flat with very weak dependence on α.

We further explore the dependence of the eigenvalue spectra on $\alpha > -1$ by fitting the higher components of each eigenvalue spectrum with a power-law function of the form $\lambda_k \sim k^{-\gamma}$ and show in Figure 5.17 the dependence of the fitted power-law index γ on α. We find this dependence to be

$$\gamma \simeq \frac{5}{4}\alpha + 2 \, . \tag{5.37}$$

Note that, for the simulations used in generating Figure 5.17, we set $q_{\min} = 0.1$ to force the breaks of the eigenvalue spectra to occur at low PCA components and, thus,

to allow for a more accurate determination of the power-law index of the spectra. This result demonstrates that the 2D Fourier spectrum of the structures in the image plane determine in a predictable way the high-end spectrum of PCA eigenvalues and, therefore, the latter can be used to infer the former.

5.5.3 The Small-Scale Structures of black hole Images from GRMHD Simulations

We compare in Figure 5.16 the spectra of PCA eigenvalues from the black hole images of GRMHD simulations to those of the images with red-noise Fourier spectra. The large range of eigenvalues in the GRMHD simulations is clearly inconsistent with the small expected range of eigenvalues for purely Gaussian noise (see also Fig. 5.12). This suggests a more complex origin of image structure and variability than what has been assumed in the past (cf. Broderick et al. 2016).

The spectra of PCA eigenvalues for the images of GRMHD simulations become power laws after only the first handful of PCA components. This suggests that $Lq_{\rm min}$ for these simulations is a small number (see eq. (5.36) and Figure 5.15) and, therefore, that the typical scale of variable structure in the images is comparable to the size of the images themselves. In other words, it is comparable to the size of the black hole shadow. This is consistent with the discussion in Chapters 3 and **??**, where we attributed the variability of the simulated interferometric amplitudes and closure phases to overall changes in the widths of the crescent-like images as well as to the appearance and disappearance from

the images of large, hot, and, therefore, bright magnetic flux tubes that orbit the black hole.

The power-law indices in the eigenvalue spectra of the images from GRMHD simulations are nearly independent of the underlying model and equal to $\gamma \simeq 1.3$. Using equation (5.37), we find that this implies a power-law index for the 2D Fourier spectrum of the variable structures of $\alpha \simeq -0.5$. It is important to emphasize here that this power-law index characterizes the 2D Fourier spectrum of the variable structures, which are determined in a complex, non-linear way by the anisotropies in the density, temperature, emissivity, magnetic field, and lensing in the vicinity of the black hole. It is, therefore, not surprising that the inferred value of α does not reflect the underlying power-spectrum of the MHD turbulence in the accretion flow.

5.6 Conclusion

Understanding the horizon-scale millimeter emission around an accreting black hole requires a two-pronged approach. One component is to utilize our best understanding of the physics to generate high-fidelity GRMHD simulations of the morphology of the emission. The second is to use an interferometer, such as the EHT, to test the understanding of the physics with real observations. In both components, there is a common theme: the question of how we characterize and extract the salient information in an ensemble of images. In this paper, we have demonstrated that PCA offers an effective tool for this task over a wealth of different problems.

Focusing purely on the simulations, we showed that PCA offers an extremely compact representation of the theoretical millimeter images. Each simulation comprises over 1000 distinct images, yet we find that we can represent *most* of the images with only a few to a few dozen eigenimages, depending on the desired fidelity. Moreover, recognizing images poorly represented by the leading eigenimages is critical and represents another useful application of PCA. As detailed in the Introduction, temporal variability of the strength and morphology of the millimeter emission close to the horizon is a phenomenon that can limit or compromise the construction of interferometric images. Knowledge of the amplitudes of the eigenimages needed to represent any given image can be used to define a simple scalar metric that flags outliers in either the simulations or observations. This approach has already provided the realization that outliers may be more subtle than had been presumed. It had been supposed that flares in flux would correspond to events in which the emission morphology would show strong departures from the average form. Yet the outlier metric R_{nl} (see Eq. 5.30) allowed us to identify both images that had unusual morphology with no significant excursion in flux, as well as flare events that had perfectly ordinary morphology. As useful as this particular metric is in this work, however, we emphasize that other metrics and classifiers can be constructed from the locations of the simulated images in their eigenspace. Our goal here is not to strongly advocate any particular metric but to provide a useful example of what is possible within the PCA representation.

Apart from the identification of outliers, we also demonstrated the use of the eigen-

value spectrum to characterize the properties of the noise and turbulent structure in the simulations. This approach shows a path for allowing the rapid quantitative evaluation of GRMHD simulations over a significant timespan of accretion. As with the outlier metric R_{nl}, other diagnostic metrics can be built around the locations or trajectories of the simulated images as a function of time in their eigenspace.

Lastly, we showed that PCA may be applied directly to the analysis of interferometric data because the Fourier transform of the principal components of a set of images is equivalent to the principal components of the set of Fourier transformed images. Coupled with the dimensionality reduction that we discussed above, this property opens the possibility of using PCA for efficient image reconstruction from sparse interferometric data. In parallel, the PCA approach can be incorporated into the Bayesian inference method discussed in Kim et al. (2016), in order to generate efficient comparisons of EHT data to large suites of GRMHD simulations. Additionally, analysis of the temporal variability of the amplitude of each eigenimage may be fruitful for further understanding variability in both the simulations and the data. We will explore these avenues in future work.

Chapter 6

Conclusions

In this dissertation, we have explored in depth the effect of intrinsic source variability on interferometric visibilities. We have specifically focused on Sgr A*, motivated by recent EHT observations, and used a set of high-fidelity GRMHD + ray tracing simulations. We began by exploring how the variability seen in these GRMHD simulations affects the structure of visibility amplitudes in Chapter 3. We found that, in all simulations, the visibility amplitudes for baselines oriented parallel and perpendicular to the spin axis of the black hole follow general trends that do not depend strongly on accretion-flow properties. This suggests that fitting Event Horizon Telescope observations with simple geometric models may lead to a reasonably accurate determination of the orientation of the black hole on the plane of the sky. We showed that, especially for SANE models, intrinsic source variability causes the main features in the visibility amplitude maps, the minima or"nulls", to move as a function of time. Consequently, if visibility amplitude is

averaged over time, the information about the existence and location of these minima will be washed out, which can significantly affect the EHT's ability to accurately reconstruct an image from interferometric visibilities. We also developed simple analytic models to understand how changes in image morphology are manifest in $u-v$ space for both MAD and SANE models.

After demonstrating that intrinsic source variability will significantly affect the visibility amplitudes the EHT will measure, we turned our attention to visibility phase. We explored the distribution of variability in phase in $u-v$ space and showed that regions of low visibility amplitude correspond to significant peaks in phase variability. If a corner of a closure triangle crosses one of these small regions of high phase variability, the closure phase for that triangle will be highly variable. Because the density of these high phase variability regions tends to increase with baseline length, variability in closure phases will increase with triangle size. We further showed that our simulations are consistent with currently published closure phases measured by the EHT, indicating that the low variability in the small closure triangle that has been measured does not imply that the larger triangles will have low variability. It is therefore crucial that the EHT model fitting and image reconstruction algorithms prepare for variable closure phases.

The results presented in Chapters 3 and 4 motivated us to explore novel ways of comparing simulations to future EHT data and of reconstructing images from EHT data. In Chapter 5, we explored the utility of PCA to both characterize and understand the variability present in the simulations and also as a means to mitigate many of the concerns

identified in Chapters 3 and 4. We found that PCA can be used to compactly represent the space of images that result from GRMHD simulations. Specifically, we showed that only a dozen PCA components are needed to reconstruct almost all images, even from the most variable simulation we considered. We also showed that the PCA components of the visibilities of a set of images are identical to the visibilities of the PCA components of the same set of images. This property will allow us to fit PCA components to interferometric visibilities in Fourier space directly.

Additionally, we derived a PCA-based metric that can be used to identify images with unusual image morphology within a set of images. Surprisingly, we found that images identified as structural outliers are not necessarily associated with a flux excursion, and that flux excursions do not require a structural outlier. Finally, we identified a relationship between the PCA eigenvalue spectrum of a set of images and the power spectrum of the structures contained in these images.

In future work, we will use a PCA eigenbasis to compare GRMHD simulations to EHT data. Current model-fitting algorithms either compare EHT data to the mean image of a GRMHD simulation or compare EHT data to each snapshot in a GRMHD simulation. The approach we propose improves upon this because the entire space of images created by either one or several GRMHD simulations can be fit to EHT data in one step. Furthermore, because a PCA eigenbasis can be used to reconstruct images that are not contained within the original data set (as long as the image is similar to the images in the set), the emission structure of the source does not need to match any particular

snapshot in the simulation for us to reconstruct an image using a PCA basis. By fitting a PCA eigenbasis derived from physically motivated simulations to EHT data, we aim to both perform model fitting to find a best fit model and to reconstruct a time-variable image that relies on assumptions that are completely independent from the assumptions used in traditional image reconstruction algorithms.

The work presented in this dissertation has also motivated a parallel line of research where we aim to use PCA to compare black hole shadows created by non-Kerr metrics to EHT data. We have simulated a large number of non-Kerr shadows using a set of metrics that are parametric extensions to Kerr. We performed PCA on this data set and found that only a small number of PCA components is necessary to reconstruct the entire data set and that the results of fitting these components to EHT data can be used to place constraints on deviations away from the Kerr metric. The results of this work could not be included in this dissertation per the constraints outlined in the collaboration agreement, but will be published separately.

Bibliography

Abramowicz, M. A., Chen, X., Kato, S., Lasota, J.-P., & Regev, O. 1995, ApJ, 438, L37

Abramowicz, M. A., Czerny, B., Lasota, J. P., & Szuszkiewicz, E. 1988, ApJ, 332, 646

Abramowicz, M. A., & Fragile, P. C. 2013, Living Reviews in Relativity, 16, 1

Akiyama, K., et al. 2017, AJ, 153, 159

Anninos, P., Fragile, P. C., & Salmonson, J. D. 2005, ApJ, 635, 723

Baganoff, F. K., et al. 2001, Nature, 413, 45

Balbus, S. A., & Hawley, J. F. 1991, ApJ, 376, 214

—. 1998, Reviews of Modern Physics, 70, 1

Ball, D., Özel, F., Psaltis, D., & Chan, C.-k. 2016, ApJ, 826, 77

Begelman, M. C. 1979, MNRAS, 187, 237

Begelman, M. C., & Meier, D. L. 1982, ApJ, 253, 873

Blaes, O. 2014, Space Sci. Rev., 183, 21

Boroson, T. A., & Lauer, T. R. 2010, AJ, 140, 390

Bouman, K. L., Johnson, M. D., Dalca, A. V., Chael, A. A., Roelofs, F., Doeleman, S. S., & Freeman, W. T. 2017, arXiv e-prints

Bouman, K. L., Johnson, M. D., Zoran, D., Fish, V. L., Doeleman, S. S., & Freeman, W. T. 2016, in The IEEE Conference on Computer Vision and Pattern Recognition (CVPR)

Broderick, A. E., Fish, V. L., Doeleman, S. S., & Loeb, A. 2011a, ApJ, 738, 38

—. 2011b, ApJ, 735, 110

Broderick, A. E., & Loeb, A. 2006, ApJ, 636, L109

Broderick, A. E., et al. 2016, ApJ, 820, 137

Chael, A., Rowan, M., Narayan, R., Johnson, M., & Sironi, L. 2018, MNRAS, 478, 5209

Chael, A. A., Johnson, M. D., Narayan, R., Doeleman, S. S., Wardle, J. F. C., & Bouman, K. L. 2016, ApJ, 829, 11

Chan, C.-k., Liu, S., Fryer, C. L., Psaltis, D., Özel, F., Rockefeller, G., & Melia, F. 2009, ApJ, 701, 521

Chan, C.-k., Medeiros, L., Özel, F., & Psaltis, D. 2018, ApJ, 867, 59

Chan, C.-k., Psaltis, D., & Özel, F. 2005, ApJ, 628, 353

—. 2013, ApJ, 777, 13

Chan, C.-k., Psaltis, D., Özel, F., Medeiros, L., Marrone, D., Sądowski, A., & Narayan, R. 2015a, ApJ, 812, 103

Chan, C.-K., Psaltis, D., Özel, F., Narayan, R., & Saḍowski, A. 2015b, ApJ, 799, 1

Chen, X., Abramowicz, M. A., Lasota, J.-P., Narayan, R., & Yi, I. 1995, ApJ, 443, L61

Chen, X., & Taam, R. E. 1993, ApJ, 412, 254

Curd, B., & Narayan, R. 2019, MNRAS, 483, 565

Davis, S. W., Stone, J. M., & Jiang, Y.-F. 2012, ApJS, 199, 9

De Villiers, J.-P., & Hawley, J. F. 2002, ApJ, 577, 866

—. 2003, ApJ, 589, 458

Dexter, J., Agol, E., & Fragile, P. C. 2009, ApJ, 703, L142

Dexter, J., Agol, E., Fragile, P. C., & McKinney, J. C. 2010, ApJ, 717, 1092

Dexter, J., Agol, E., Fragile, P. C., & McKinney, J. C. 2012, in Journal of Physics Conference Series, Vol. 372, Journal of Physics Conference Series, 012023

Dexter, J., Kelly, B., Bower, G. C., Marrone, D. P., Stone, J., & Plambeck, R. 2014, MNRAS, 442, 2797

Di Matteo, T., Allen, S. W., Fabian, A. C., Wilson, A. S., & Young, A. J. 2003, ApJ, 582, 133

Do, T., Ghez, A. M., Morris, M. R., Yelda, S., Meyer, L., Lu, J. R., Hornstein, S. D., & Matthews, K. 2009, ApJ, 691, 1021

Dodds-Eden, K., Sharma, P., Quataert, E., Genzel, R., Gillessen, S., Eisenhauer, F., & Porquet, D. 2010, ApJ, 725, 450

Doeleman, S., et al. 2009a, in arXiv Astrophysics e-prints, Vol. 2010, astro2010: The Astronomy and Astrophysics Decadal Survey

Doeleman, S. S., Fish, V. L., Broderick, A. E., Loeb, A., & Rogers, A. E. E. 2009b, ApJ, 695, 59

Doeleman, S. S., et al. 2002, in Proceedings of the 6th EVN Symposium, ed. E. Ros, R. W. Porcas, A. P. Lobanov, & J. A. Zensus, 223

Doeleman, S. S., et al. 2008, Nature, 455, 78

Dolence, J. C., Gammie, C. F., Mościbrodzka, M., & Leung, P. K. 2009, ApJS, 184, 387

Dolence, J. C., Gammie, C. F., Shiokawa, H., & Noble, S. C. 2012, ApJ, 746, L10

Fish, V. L., et al. 2011, ApJ, 727, L36

—. 2016, ApJ, 820, 90

Fraga-Encinas, R., Mościbrodzka, M., Brinkerink, C., & Falcke, H. 2016, A&A, 588, A57

Fragile, P. C., & Anninos, P. 2005, ApJ, 623, 347

Frank, J., King, A., & Raine, D. J. 2002, Accretion Power in Astrophysics: Third Edition, 398

Gammie, C. F., McKinney, J. C., & Tóth, G. 2003, ApJ, 589, 444

Genzel, R., Schödel, R., Ott, T., Eckart, A., Alexander, T., Lacombe, F., Rouan, D., & Aschenbach, B. 2003, Nature, 425, 934

Ghez, A. M., et al. 2008, ApJ, 689, 1044

Gillessen, S., Eisenhauer, F., Trippe, S., Alexander, T., Genzel, R., Martins, F., & Ott, T. 2009, ApJ, 692, 1075

Gold, R., McKinney, J. C., Johnson, M. D., & Doeleman, S. S. 2017, ApJ, 837, 180

Hawley, J. F., & Krolik, J. H. 2006, ApJ, 641, 103

Honma, M., Akiyama, K., Uemura, M., & Ikeda, S. 2014, PASJ, 66, 95

Howes, G. 2011, ApJ, 738, 40

Howes, G. G. 2010, MNRAS, 409, L104

Ichimaru, S. 1977, ApJ, 214, 840

Igumenshchev, I. V., & Abramowicz, M. A. 1999, MNRAS, 303, 309

—. 2000, ApJS, 130, 463

Igumenshchev, I. V., Abramowicz, M. A., & Narayan, R. 2000, ApJ, 537, L27

Igumenshchev, I. V., Chen, X., & Abramowicz, M. A. 1996, MNRAS, 278, 236

Jennison, R. C. 1958, MNRAS, 118, 276

Jiang, Y.-F., Stone, J. M., & Davis, S. W. 2014, ApJS, 213, 7

Johannsen, T., & Psaltis, D. 2011, Advances in Space Research, 47, 528

Johannsen, T., Psaltis, D., Gillessen, S., Marrone, D. P., Özel, F., Doeleman, S. S., & Fish, V. L. 2012, ApJ, 758, 30

Johnson, M. D., & Gwinn, C. R. 2015, ApJ, 805, 180

Johnson, M. D., & Narayan, R. 2016, ApJ, 826, 170

Johnson, M. D., et al. 2015, Science, 350, 1242

—. 2017, ApJ, 850, 172

Kamruddin, A. B., & Dexter, J. 2013, MNRAS, 434, 765

Kato, S., Fukue, J., & Mineshige, S. 2008, Black-Hole Accretion Disks — Towards a New Paradigm —

Katz, J. I. 1977, ApJ, 215, 265

Kim, J., Marrone, D. P., Chan, C.-K., Medeiros, L., Özel, F., & Psaltis, D. 2016, ApJ, 832, 156

Lu, R.-S., et al. 2016, ApJ, 817, 173

Lynden-Bell, D., & Pringle, J. E. 1974, MNRAS, 168, 603

Mahalanobis, P. C. 1936, Proceedings of the National Institute of Sciences (Calcutta), 2, 49

Mardia, K., & Jupp, P. 1999, Directional Statistics, 1st edn. (Baffins Lane, Chichester, West Sussex, PO19 IUD England: Wiley)

Marrone, D. P., Moran, J. M., Zhao, J.-H., & Rao, R. 2007, ApJ, 654, L57

Marrone, D. P., et al. 2008, ApJ, 682, 373

McKinney, J. C., & Gammie, C. F. 2004, ApJ, 611, 977

McKinney, J. C., Tchekhovskoy, A., & Blandford, R. D. 2012, MNRAS, 423, 3083

Medeiros, L., Chan, C.-k., Özel, F., Psaltis, D., Kim, J., Marrone, D. P., & Saḑowski, A. 2017, ApJ, 844, 35

Medeiros, L., Chan, C.-k., Özel, F., Psaltis, D., Kim, J., Marrone, D. P., & Sądowski, A. 2018a, ApJ, 856, 163

Medeiros, L., Lauer, T. R., Psaltis, D., & Özel, F. 2018b, ApJ, 864, 7

Meyer, L., Do, T., Ghez, A., Morris, M. R., Witzel, G., Eckart, A., Bélanger, G., & Schödel, R. 2008, ApJ, 688, L17

Morales Teixeira, D., Avara, M. J., & McKinney, J. C. 2018, MNRAS, 480, 3547

Mościbrodzka, M., Dexter, J., Davelaar, J., & Falcke, H. 2017, MNRAS, 468, 2214

Mościbrodzka, M., & Falcke, H. 2013, A&A, 559, L3

Mościbrodzka, M., Falcke, H., Shiokawa, H., & Gammie, C. F. 2014, A&A, 570, A7

Mościbrodzka, M., Gammie, C. F., Dolence, J. C., & Shiokawa, H. 2011, ApJ, 735, 9

Mościbrodzka, M., Gammie, C. F., Dolence, J. C., Shiokawa, H., & Leung, P. K. 2009a, ApJ, 706, 497

—. 2009b, ApJ, 706, 497

Narayan, R., Sądowski, A., Penna, R. F., & Kulkarni, A. K. 2012, MNRAS, 426, 3241

Narayan, R., & Yi, I. 1994, ApJ, 428, L13

—. 1995a, ApJ, 444, 231

—. 1995b, ApJ, 452, 710

Neilsen, J., et al. 2013, ApJ, 774, 42

—. 2015, ApJ, 799, 199

Novikov, I. D., & Thorne, K. S. 1973, in Black Holes (Les Astres Occlus), ed. C. Dewitt & B. S. Dewitt, 343–450

Ohsuga, K., Mori, M., Nakamoto, T., & Mineshige, S. 2005, ApJ, 628, 368

Porquet, D., et al. 2008, A&A, 488, 549

Pringle, J. E. 1981, ARA&A, 19, 137

Psaltis, D., Narayan, R., Fish, V. L., Broderick, A. E., Loeb, A., & Doeleman, S. S. 2015a, ApJ, 798, 15

Psaltis, D., Özel, F., Chan, C.-K., & Marrone, D. P. 2015b, ApJ, 814, 115

Rauch, K. P., & Blandford, R. D. 1994, ApJ, 421, 46

Rees, M. J., Begelman, M. C., Blandford, R. D., & Phinney, E. S. 1982, Nature, 295, 17

Remillard, R. A., & McClintock, J. E. 2006, ARA&A, 44, 49

Ressler, S. M., Tchekhovskoy, A., Quataert, E., & Gammie, C. F. 2017, MNRAS, 467, 3604

Ryan, B. R., Ressler, S. M., Dolence, J. C., Gammie, C., & Quataert, E. 2018, ApJ, 864, 126

Sądowski, A., Narayan, R., Penna, R., & Zhu, Y. 2013, MNRAS, 436, 3856

Sądowski, A., Wielgus, M., Narayan, R., Abarca, D., McKinney, J. C., & Chael, A. 2017, MNRAS, 466, 705

Shakura, N. I., & Sunyaev, R. A. 1973, A&A, 24, 337

Shapiro, S. L., Lightman, A. P., & Eardley, D. M. 1976, ApJ, 204, 187

Shcherbakov, R. V., & Baganoff, F. K. 2010, ApJ, 716, 504

Shcherbakov, R. V., Penna, R. F., & McKinney, J. C. 2012, ApJ, 755, 133

Shiokawa, H., Dolence, J. C., Gammie, C. F., & Noble, S. C. 2012, ApJ, 744, 187

Stone, J. M., Gardiner, T. A., Teuben, P., Hawley, J. F., & Simon, J. B. 2008, ApJS, 178, 137

Stone, J. M., & Norman, M. L. 1992a, ApJS, 80, 753

—. 1992b, ApJS, 80, 791

Stone, J. M., Pringle, J. E., & Begelman, M. C. 1999, MNRAS, 310, 1002

Strang, G. 1988, Linear algebra and its applications, 3rd edn. (Orlando, Florida 32887: Harcourt Brace Jovanovich)

Tchekhovskoy, A., McKinney, J. C., & Narayan, R. 2012, in Journal of Physics Conference Series, Vol. 372, Journal of Physics Conference Series, 012040

Turk, M., & Pentland, A. 1991, Journal of cognitive neuroscience, 3, 71

van der Klis, M. 2000, ARA&A, 38, 717

Yuan, F., & Narayan, R. 2014, ARA&A, 52, 529

Appendix A

Directional Statistics

Calculating statistical moments of distributions of quantities that are periodic in nature, such as closure phases, requires special care. Mardia & Jupp (1999) explore meaningful ways of determining the mean and dispersion of distributions of angles. Specifically, they suggest that the mean of a distribution of n angles θ_j may be obtained using

$$\bar{\theta} = \begin{cases} \tan^{-1}\left(\bar{S}/\bar{C}\right), & \text{if } \bar{C} \geq 0 \\ \tan^{-1}\left(\bar{S}/\bar{C}\right) + \pi, & \text{if } \bar{C} < 0, \end{cases} \tag{A.1}$$

where

$$\bar{S} = \quad \frac{1}{n}\sum_{j=1}^{n} \sin(\theta_j) \tag{A.2}$$

$$\bar{C} = \quad \frac{1}{n}\sum_{j=1}^{n} \cos(\theta_j). \tag{A.3}$$

In words, to calculate the mean of a distribution of angles, we calculate the mean of the unit vectors that correspond to the distribution of angles. The dispersion of a distribution

of angles then is defined as

$$D = \frac{1}{n}\sum_{j=1}^{n}\{1 - \cos(\theta_j - \bar{\theta})\}. \tag{A.4}$$

Hereafter, we will refer to this dispersion relation as the directional dispersion when comparing it to the dispersion relation commonly used for non-directional data.

To understand the behavior of the directional dispersion, we consider here two limiting cases. For small deviation from the mean $(\theta_j - \bar{\theta})$, the directional dispersion can be approximated as

$$\begin{aligned} D &\simeq \frac{1}{n}\sum_{j=1}^{n}\left[1 - \left(1 - \frac{(\theta_j - \bar{\theta})^2}{2}\right)\right] \\ &= \frac{1}{2n}\sum_{j=1}^{n}\left[(\theta_j - \bar{\theta})^2\right] \\ &= \frac{\sigma^2}{2}, \end{aligned} \tag{A.5}$$

where we have denoted the normal definition of dispersion by σ.

In the limit of a continuous flat distribution of deviations from the mean, on the other hand, we find

$$\begin{aligned} D &\simeq \frac{1}{2\pi}\int_{-\pi}^{\pi}[1 - \cos(\theta_j - \bar{\theta})]d\theta \\ &= 1 - \frac{1}{2\pi}\int_{-\pi}^{\pi}\cos(\theta_j - \bar{\theta})d\theta \\ &= 1. \end{aligned} \tag{A.6}$$

In Figure A.1, we explore the behavior of the directional dispersion further by com-

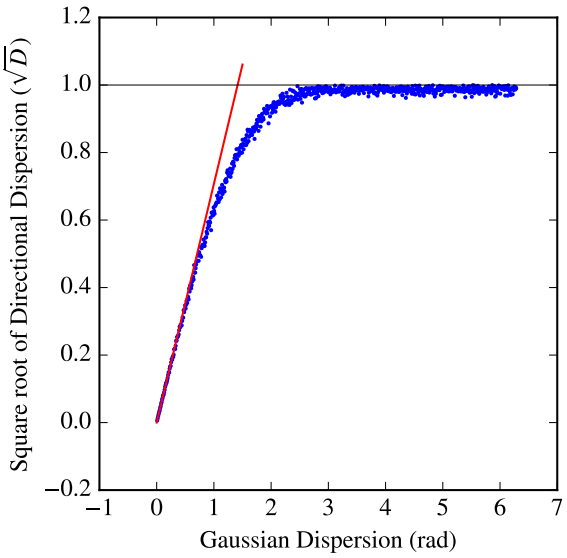

Figure A.1 Directional dispersion, D, of a Monte Carlo distribution of data calculated using directional statistics as a function of the standard deviation of a Gaussian distribution that was used to create the Monte Carlo data. The red line corresponds to $D = \sigma^2/2$. The horizontal black line is at $D = 1$. As the standard deviation in the Monte Carlo simulation reaches $\approx \pi$, the directional dispersion approaches unity and remains constant as the standard deviation in the Monte Carlo increases further.

paring this quantity to the dispersion σ of an ensemble of Monte Carlo points drawn from a Gaussian distribution. The blue points are the square root of the directional dispersion of simulated data created using Gaussian distributions with different dispersions. As expected, the directional dispersion scales with the dispersion of the Gaussian distribution when the latter is small. However, as $\sigma \gtrsim \pi$, the periodic nature of the angular data causes the directional dispersion to asymptote to unity.